Optical Momentum Transfer to Macroscopic Media

by

Brandon Alden Kemp

B.S.Engr., Electrical Engineering
Arkansas State University, May 1997
M.S., Electrical Engineering and Computer Science
University of Missouri-Rolla, December 1998

Submitted to the Department of Electrical Engineering and Computer Science
in partial fulfillment of the requirements for the degree of

Doctor of Philosophy

at the

MASSACHUSETTS INSTITUTE OF TECHNOLOGY

June 2007

BARKER

MASSACHUSETTS INSTITUTE OF TECHNOLOGY
AUG 16 2007
LIBRARIES

© Massachusetts Institute of Technology 2007. All rights reserved.

Author ....
Department of Electrical Engineering and Computer Science
April 26, 2007

Certified by..... .....
Jin Au Kong
Professor of Electrical Engineering
Thesis Supervisor

Certified by..... .....
Tomasz M. Grzegorczyk
Research Scientist
Thesis Supervisor

Accepted by..... .....
Arthur C. Smith
Chairman, Department Committee on Graduate Students

Optical Momentum Transfer to Macroscopic Media

by

Brandon Alden Kemp

Submitted to the Department of Electrical Engineering and Computer Science
on April 26, 2007, in partial fulfillment of the
requirements for the degree of
Doctor of Philosophy

Abstract

Persistent conflicts over the momentum of light in media has led researchers to apply an alternate approach to predicting the electromagnetic force on material. Direct application of the Lorentz force to media allows for the computation of electromagnetic forces while avoiding *a priori* assumptions for the form of optical momentum. In this view, the forces exist everywhere in matter once the field is present. Because of this, the approach can be computationally daunting, particularly when multiple particles are surrounded by a medium with a dielectric or magnetic response to the fields. The theory presented in this thesis represents a self-consistent formulation for efficiently modeling optical momentum transfer to macroscopic media.

The Maxwell stress tensor and the distributed Lorentz force are first applied to calculate forces on lossless media and are shown to be in excellent agreement. It is shown that a normally incident plane wave pushes a slab in the wave propagation direction, while it pulls a half-space toward the incoming wave. The Lorentz force density is applied to the slab in a direct way, while the half-space is dealt with by introducing a finite amount of loss. The losses have to be properly accounted for, otherwise differing results are obtained. The momentum transfer to lossy dielectric and magnetic media is derived from the Lorentz force density without prior assumption of the momentum of light in media. A view of momentum conservation is developed which is rooted in the stress tensor formalism and is based on the separation of momentum contributions to bound and free currents and charges consistent with the Lorentz force density. The formulation is shown to be in agreement with known observations of momentum transfer to media.

The electromagnetic wave momentum is derived for a Lorentz medium and applied to study the momentum transfer to stationary, isotropic left-handed material. The model includes material dispersion and losses, which are necessary for a causal medium with negative index of refraction. The results provide a rigorous proof for the force on free currents in a lossy medium . The resulting electromagnetic wave momentum conservation theorem proves that the momentum flux of a monochromatic

wave in an isotropic left-handed material is opposite to the power flow direction. However, the momentum density in a lossy medium with negative index of refraction may be parallel or antiparallel to the power flow. The results are applied to predict the reversal of radiation pressure on free currents in a material with negative index of refraction. Furthermore, conservation of momentum at a material boundary states that the tangential component of the wave momentum is conserved.

The theory is applied to predict new experiments such a decrease in optical momentum transfer to Mie particles due to absorption, which contrasts the common intuition based on the scattering and absorption by Rayleigh particles. Lossless dielectric particles incident by multiple plane waves and a Gaussian beam are also studied using Mie theory to model existing experiments of optical manipulation using lasers. The modeling of single particles is achieved by applying analytical field calculations to infinite cylinders used to represent particles in two dimensions and to spheres used to more closely model three dimensional experiments. The application of electromagnetic wave momentum conservation via the stress tensor formalism allows us to compute the experimentally observed dynamics of particles in solution while reducing the computation by one dimension. For example, the force on a dielectric sphere can be computed by either applying a volume integration of the Lorentz force or by computing the surface integration of the Maxwell stress tensor.

The Mie theory and the FoldyLax multiple-scattering equations are applied to compute the scattered field of an arbitrary number of infinite dielectric cylinders of arbitrary size, subject to in-plane incidences. Binding forces are studied as a function of particle size and separation. The formulation is applied to a system of 20 particles, and extends the capabilities of modeling particle interaction and optical matter beyond the simple cases of the Rayleigh regime and two-particle systems. Based on this approach, a new trapping regime is proposed, which is based on the equilibrium between a scattering force and optical binding forces only. The trap is realized from the interaction between a single plane wave and a series of fixed small particles, and is efficient at trapping multiple free particles. The possibility of serially guiding and sorting nanometer-sized particles without the use of any external control is also demonstrated. The working principle is based on an equilibrium between scattering and binding forces, the latter depending on the properties of the particles. A configuration is proposed that utilizes this property and is shown to efficiently sort small particles as function of their size. In order to understand the complex interactions between dielectric particles, a simplified geometry consisting of identical slabs subjected to normally incident plane waves is also studied.

Thesis Supervisor: Jin Au Kong
Title: Professor of Electrical Engineering

Thesis Supervisor: Tomasz M. Grzegorczyk
Title: Research Scientist

Acknowledgments

I would sincerely like to thank my research advisors Professor Jin Au Kong and Dr. Tomasz M. Grzegorczyk. Although this thesis reports my own investigation of the electromagnetic momentum transfer to media, the modeling of optical manipulation of small particles was developed as a collaborative effort by myself and Dr. Grzegorczyk. It has truly been a pleasure developing this topic from first principles, and I have learned a great deal about the business of doing applied research from Dr. Grzegorczyk. I have also learned a lot about electromagnetic wave theory and problem solving from Professor Kong as both a research assistant and a teaching assistant. I acknowledge Professor Kong's breath of knowledge and unique ability to explain difficult concepts. To Professor Kong and Dr. Grzegorczyk I extend my deepest gratitude.

During the course of my thesis research, I had the pleasure of communicating with a number of people about my work. I had a spirited discussion of electromagnetic force calculations with my Research Qualifying Exam (RQE) Committee consisting of Professor Markus Zahn and Professor David Staelin. I also would like to thank Professor Staelin for serving on my thesis committee. I was fortunate to have enlightening conversation with others researchers in the field of optical manipulation: Professor Jean-Marc Fournier of the Swiss Federal Institute of Technology in Lausanne, Switzerland; Dr. Michael Scalora of U.S. Army Missile Command, Redstone Arsenal in Alabama, USA; and Dr. Timo Nieminen of The University of Queensland, Australia. I would also like to acknowledge my colleagues at CETA for all of the discussions on all aspects of electromagnetic theory and applications. Thank you Zachary Thomas, Bill Herrington, Beijia Zhang, Dr. Hongsheng Chen, Kei Suwa, Zhen Li, Professor Xudong Chen, Song Liang Chua, Micheal Yeung, Bailc Zhang, Dr. Jie Lu, Dr. James Chen, and Dr. Bae-Ian Wu.

This doctoral degree was completed with financial support from various sources. It is a pleasure to acknowledge research assistantships with Dr. Cory Myers at BAE

Systems Information and Electronic Warfare Systems, Dr. Audrey Dumanian and Dr. Mohamed Abouzahra of MIT Lincoln Laboratory Group 34, and Dr. Yoshihisa Hara of Mitsubishi Electric. I was also fortunate to spend three semesters as Professor Kong's teaching assistant within the Department of Electrical and Computer Engineering. Finally, I would like to acknowledge the support of NASA Institute for Advanced Concepts (NIAC) Phase II LTM study and principal investigator Professor Elizabeth McCormack of Bryn Mawr College, Pennsylvania, USA.

I want to extend a special note of gratitude to Professor Robert D. Engelken at Arkansas State University. Professor Engelken served as my undergraduate advisor and research supervisor. He provided me with my first research opportunity as part of a NASA Joint Venture Outreach program in the Summer of 1993. I am truly grateful to him for extending a research assistantship to me the following academic year as a true freshman. I owe a lot of my current successes to the opportunities Professor Engelken afforded me, and the lessons in research learned during my time at Arkansas State University.

Finally, I want to thank my family. My parents, Donnie and Freda, have always instilled in me the importance of education. My brother, Bellamy, has always shown unwavering support in my endeavors and faith is my abilities. Last, but certainly not least, I thank my wife, Shan. She is my soul-mate and best friend, who accompanies me on this journey of life. This doctoral thesis marks the end of what we have come to term "the great MIT adventure." This accomplishment is as much hers as it is mine. Thank you.

For my daughter, Hadley Faith

Contents

List of Figures

List of Tables

Chapter 1

Introduction

In 2005, I began a study of optical momentum transfer to macroscopic media in order to model the manipulation on colloidal particles with lasers. In March of that year, my research supervisor, Dr. Tomasz M. Grzegorczyk, was personal witness to the optical binding experiments of Professor Jean-Marc Fournier at the Swiss Federal Institute of Technology. Upon his return, Dr. Grzegorczyk described to me the fascinating experiments that turned a collection of colloidal particles into an array of optical matter in the presence of a laser field. It was around this time that Dr. Grzegorczyk began developing an analytic multi-body scattering code that would eventually be used to model the optical forces within a collection of particles. One of the original goals of this modeling effort was to aid in the design of a laser trapped mirror (LTM) that would use optical matter as a imaging reflector in space. I began my own investigation of this subject on my own accord in May 2005. It soon evolved from mere curiosity to become my primary research focus while at MIT. By September 2005, we officially began working on the NASA Institute for Advanced Concepts (NIAC) Phase II LTM study along with Professor Fournier, principal investigator Professor Elizabeth McCormack of Bryn Mawr College, and former NASA headquarters member, Dr. Robert Stachnik. It was an immediate goal to under-

stand the complex nature of optical forces on colloidal particles and to theoretically recreate the optical binding experiments. This dissertation reports the results of this theoretical investigation and modeling effort.

1.1 Background

Electromagnetic wave theory was first applied by J. C. Maxwell to predict and calculate radiation pressure of light [8]. This prediction was soon verified by the observation of light pressure on reflectors in vacuum [9, 10]. In 1905, Poynting quantitatively validated the theory with detailed measurements of radiation pressure [11]. Until the invention of the laser, such experiments were relegated to scientific validation of the electromagnetic wave theory.

1.1.1 Optical manipulation of colloidal particles

In 1970, the manipulation of small dielectric particles by laser light was first demonstrated by Arthur Ashkin at Bell Labs when particles suspended in water were drawn into the axis of a laser beam and accelerated in the direction of propagation [12]. The original experiments were designed by applying a rough calculation for the radiation pressure of a $1W$ laser focused upon spheres ranging from approximately $1\lambda_0$ to $5\lambda_0$ in diameter, where λ_0 is the laser wavelength. In addition to radiation pressure, the particles experienced a trapping force that pulled the particles into the laser beam. The trapping force was reversed when the relative index of refraction was inverted. That is, an air bubble with dielectric permittivity less than that of the surrounding water was always seen to be pushed out of the beam, while the radiation pressure remained in the beam propagation direction. The trapping force was explained using ray optics, a technique that is generally reserved to describe scattering from bodies much larger than the wavelength of light. This separation based on radiation pressure and trapping force would continue for the next 30 years.

Many experimental demonstrations followed, including optical levitation [13, 14] and radiation pressure on a liquid surface [15]. The use of lasers was also proposed as an atom trap [16, 17], and eventually realized to trap and cool atoms by Steven Chu of Bell Labs [18–20], who became one of at least two Nobel Laureates owing some acknowledgement to the use of optical trapping. The trapping force and radiation pressure became to be known as the gradient force and the scattering force, respectively, due to the separation based on the Rayleigh approximation for a point scatterer [21]. The former force reduces to the gradient of incident field intensity, and the latter is described simply by the scattering of incident momentum. Mesoscopic dielectric particles were also trapped using a single highly focused laser beam [22]. Such traps, termed optical tweezers, result when a the gradient force is larger than the scattering force as predicted by application of the Rayleigh approximation [23, 24]. Optical manipulation has since found application in physics, biology, chemistry, and medicine [25–27]. In fact, optical tweezers have become a necessary tool for many researchers in microbiology. Besides manipulating living organisms with lasers directly [28], researchers are also applying particles as handles to characterize the mechanics of living cells. In this regard, there is a need to consider metal particles [29, 30] and novel materials that may provide higher trapping efficiencies for optical handles [31].

The description of optical manipulation was further expanded in 1989 when optical binding was first observed [32]. Optical binding refers to the interaction forces between multiple particles and can be used to create a lattice of dielectric particles termed optical matter [33]. Optical binding was originally described by the interaction of dipoles induced by an electromagnetic field incident on polarizable particles [34]. The binding force, scattering force, and gradient force then became the standard description for the optical manipulation of colloidal particles. Thus, while significant experimental advances have been made in optical manipulation, modeling has, until recently, remained in its infancy.

There are two primary issues responsible for this lack of theoretical development. First, a fully developed model requires the solution of Maxwell's equations in the near field region of many particles, which generally requires significant computing resources. Second, once the electromagnetic fields are known, the force must be calculated by either applying the Lorentz force directly or by computing the scattered electromagnetic momentum. The first issue is treated in this thesis by applying analytical field solutions to electromagnetic waves scattered by canonical particles (*e.g.* cylinders and spheres). However, the primary focus of this work is in regard to the second issue, which has historically been a controversial subject. It is necessary to address the issue of electromagnetic momentum in matter since the particles are typically immersed in a dielectric medium (water in most of the experiments).

1.1.2 Momentum controversy

The electromagnetic momentum in media has been debated throughout the previous century with two leading candidates; $\bar{D} \times \bar{B}$ due to Minkowski [35] and $\epsilon_0 \mu_0 \bar{E} \times \bar{H}$ due to Abraham [36, 37]. Although the so-called Abraham-Minkowski controversy originated out of relativistic formulations, the primary issue of the radiation pressure exerted on the interface of a dielectric boundary can be studied independently of material motion [38]. The momentum density vector derived from the macroscopic electromagnetic wave theory [39] for a nonmagnetic medium is $\bar{G} = \bar{D} \times \bar{B} = \epsilon_0 \mu_0 \bar{E} \times \bar{H} + \bar{P} \times \mu_0 \bar{H}$, where the wave momentum density is expressed as the sum of the electromagnetic momentum density $\epsilon_0 \mu_0 \bar{E} \times \bar{H}$ and a momentum density resulting from the dielectric polarization $\bar{P} = \bar{D} - \epsilon_0 \bar{E}$ in the presence of a field [21]. The debate of the radiation pressure of normally incident light from free space onto a dielectric can be demonstrated by momentum conservation at the interface. The difference in the radiation pressure resulting from either the Minkowski momentum $\bar{D} \times \bar{B}$ or the Abraham momentum $\epsilon_0 \mu_0 \bar{E} \times \bar{H}$ transmitted into the dielectric is significant; an outward force results from the former, while an inward force results

from the latter [40].

In contrast to momentum conservation, the force on matter due to an electromagnetic field can be computed directly via the Lorentz force. The Lorentz force has been applied to bound and free currents to compute the radiation pressure on dielectric media due to normal incidence at a planar boundary [41, 42], and the force on bound charges has been included to model forces resulting from oblique incidence [43, 44]. While some researchers have recently applied the force calculations to derive a new form of electromagnetic momentum in matter [43, 45, 46], others warn against the use of momentum conservation theorems all together [41].

1.1.3 Summary of the most relevant experiments related to momentum controversy

Several of experiments have been carried out over the last century in an attempt to measure the momentum of light. In this section, a few of these experiments are described. The experiments listed are limited to those optical or near infrared measurements that are discussed within the body of this thesis. The descriptions present what was measured and why the measurements are significant. For a detailed presentation of how a particular experiment was performed, the reader is referred to the cited references. Reviews of many of these experiments can be found in the literature [40, 47].

Tangential pressure of light In 1905, J. H. Poynting measured the tangential force due to light obliquely incident on absorbing and reflecting surfaces [11]. The tangential stress was carefully measured and reconciled with the electromagnetic wave theory of Maxwell. This experiment demonstrated that the force tangential to the surface of an absorbing material is proportional to the incident intensity and has a maximum at an incident angle of 45°. Zero tangential force was also measured for obliquely incident light upon a good reflector. This experiment represents the

first quantitative comparison of carefully measured radiation pressure effects with the electromagnetic wave theory.

Recoil of light against a source Using an analogy with the recoil of a gun, J. H. Poynting and G. Barlow performed an experiment in 1910 designed to measure the recoil force exerted by light against the source from which it originates [48]. The premise of the experiment was to study the equilibrium forces exerted upon various disks subject to steady illumination. The disks consisted of various permutations of absorbing and reflecting surfaces on their two sides. One particularly interesting result comes from the transient period of initial illumination upon the absorbing side of a disk with a reflecting silver film deposited on the unilluminated side. As the researchers remarked, "a strong suction always set in, and this suction, after reaching a maximum, rapidly subsided, giving place finally to a pressure increasing to the limiting value corresponding to the steady state." The effect was explained by the expulsion of occluded gasses from the silver films. Since in this geometry the silver film was on the unilluminated side of the disk, a back pressure was exerted upon the disk as the gas was expelled from the disk into the surrounding vacuum.

Pressure on submerged mirrors In 1954, Jones and Richards measured the deflection of reflectors as a function of refractive index of the submerging fluids [49]. The pressure exerted upon a submerged mirror in the Jones-Richards experiment was determined to be directly proportional to the index of reflection n of the surrounding medium. However, the experiment was unable to determine whether the observed proportionality n was the conventional phase velocity refractive index or the group velocity refractive index, due respectively to the ratio of phase velocity or group velocity to the speed of light in vacuum. The invention of the laser allowed Jones and Leslie in 1978 to improve upon the precision of the original experiment [50] and to determine unambiguously the dependence of the pressure upon a mirror submerged in a dielectric liquid on the phase velocity index of refraction (*i.e.* the measured

pressure was proportional to $n = c/v_p$ where v_p is the velocity of phase propagation in the surrounding dielectric).

Scattering and gradient force on dielectric particles In 1970, Arthur Ashkin at Bell Labs demonstrated that dielectric particles suspended in water could be drawn into the axis of a laser beam and accelerated in the direction of propagation [12]. In addition to radiation pressure, such particles experience a force transverse to the propagation direction, the direction of which depends upon the dielectric contrast between the particle and the surrounding liquid; dielectric particles that are optically dense compared to the background medium are pulled into the high intensity axis of the beam while less optically dense air bubbles were pushed out of the beam axis.

Photon drag The photon drag effect measured by Gibson *et. al.* is one of the most direct observations of optical momentum in dielectric media [51]. The measured current in a weakly absorbing semiconductor such as Germanium or Silicon is produced by the absorption of an electromagnetic wave in the near infrared. The experiment reveals the Minkowski momentum transferred to free carriers due to absorption of electromagnetic energy. Since the absorbed photon momentum is greater than the incident momentum by a factor of the refractive index n, it is deduced by momentum conservation that an additional force on the bulk material must be directed toward the incident wave.

Recoil momentum in a gas of atoms In 2005, the recoil momentum of single atoms struck by light in an absorptive medium has been made by Gretchen Campbell, Dave Pritchard, Wolfgang Ketterle and colleagues [52]. This experiment serves as the most direct measurement of optical momentum in matter to date. The experiment was performed by observing the change in momentum of single atoms in the lowest momentum state due to the absorption of photons. It was determined that the recoil of the momentum imparted to the atoms was directly proportional to the macroscopic

refractive index of the gas. The experiment demonstrates that a single photon entering a dilute gas is affected by the presence of all surrounding atoms.

Optical trap stiffness In 2005, A. Rohrbach provided the first quantitative agreement between measured and calculated trap stiffness of optically trapped particles. The trap stiffness represents a measurement of the linear restoring force in a particular direction. That is, if we model an optical trap as a potential well, the trap stiffness is simply the proportionality constant relating the force to the displacement distance due to small perturbation from the equilibrium position. The experiment was performed using dielectric particles suspended in water. The theoretical calculations were based on an effective force with respect to the surrounding liquid. In other words, the force was calculated as if the particle were in free space with the free space index of refraction $n = 1$ replaced simply by the index of refraction of water $n \rightarrow 1.33$. This calculated force on the particle is equivalent to calculating the difference in incident and scattered Minkowski momentum.

1.2 Thesis work

The purpose of this thesis is to provide a theoretical framework for the modeling of experiments. While some contributions have been made toward the understanding of wave electrodynamics, the emphasis has been placed on deriving a theoretical framework which may be applied to develop applications. Fundamentally, one could apply the complete description of electrodynamics provided by Penfield and Haus [53]. However, such a description would greatly hinder efforts to model many particle systems since the dynamics of both the particles and the background fluid must be taken into account within the framework of moving media. The results presented here greatly reduce the complexity and computation required to formulate the electrodynamics of multiple particles by deriving and applying the concept of an effective electromagnetic wave momentum.

1.2.1 Scope and assumptions

The basis for the theory and calculations presented herein is the macroscopic electromagnetic wave theory [39]. The Maxwell-Minkowski equations

$$\nabla \times \bar{\mathcal{H}} - \frac{\partial \bar{\mathcal{D}}}{\partial t} = \bar{\mathcal{J}} \tag{1.1a}$$

$$\nabla \times \bar{\mathcal{E}} + \frac{\partial \bar{\mathcal{B}}}{\partial t} = 0 \tag{1.1b}$$

$$\nabla \cdot \bar{\mathcal{B}} = 0 \tag{1.1c}$$

$$\nabla \cdot \bar{\mathcal{D}} = \rho \tag{1.1d}$$

make no distinction between field and matter contributions to the electromagnetic wave theory since the electric field $\bar{\mathcal{E}}$, magnetic field $\bar{\mathcal{H}}$, electric flux $\bar{\mathcal{D}}$, and magnetic flux $\bar{\mathcal{B}}$ contain the response of matter via the constitutive relations. Throughout this thesis, the materials considered are assumed to be isotropic, linear, and stationary. The limitation to stationary media is not a severe restriction since the primary issue of the radiation pressure on a material surface can be studied independently of motion [38]. The constitutive relations in the most general form for the purposes of this thesis are

$$\bar{\mathcal{D}} = \int_{-\infty}^{t} d\tau \epsilon(t-\tau)\bar{\mathcal{E}}(\tau) = \int_{0}^{\infty} d\tau \epsilon(\tau)\bar{\mathcal{E}}(t-\tau) \tag{1.2a}$$

$$\bar{\mathcal{B}} = \int_{-\infty}^{t} d\tau \mu(t-\tau)\bar{\mathcal{H}}(\tau) = \int_{0}^{\infty} d\tau \mu(\tau)\bar{\mathcal{H}}(t-\tau). \tag{1.2b}$$

Furthermore, it is assumed that the media are homogeneous except for discrete spatial discontinuities in the permittivity and permeability used to represent material boundaries.

The Lorentz force density $\rho\bar{\mathcal{E}} + \bar{\mathcal{J}} \times \bar{\mathcal{B}}$ is assumed in Chapter 2 to represent the force on electric charge ρ and electric current $\bar{\mathcal{J}}$ and applied to model the momentum transfer to lossless and lossy media. It should be noted that the form $\bar{\mathcal{J}} \times \bar{B}$ is con-

sistent with the most common form of the force on free currents found in many texts, for example [39, 54, 55], and results from historical measurements of the deflection of moving charged particles in a magnetic medium due to an applied magnetic field (see [56] and references herein). However, various scholars have proposed that the force on electric currents may be written instead as $\bar{\mathcal{J}} \times \mu_0 \bar{\mathcal{H}}$. In Chapter 3, a derivation of the wave momentum in a dispersive Lorentz medium is given and applied to predict the reversal of wave momentum in left handed materials. It is shown that both $\bar{\mathcal{J}} \times \bar{\mathcal{B}}$ and the force $\bar{\mathcal{J}} \times \mu_0 \bar{\mathcal{H}}$ have interpretations of momentum transfer to macroscopic media. That is, the form $\bar{\mathcal{J}} \times \mu_0 \bar{\mathcal{H}}$ represents part of the force density exerted upon a material by the electromagnetic fields, while $\bar{\mathcal{J}} \times \bar{\mathcal{B}}$ gives the force on free electric currents inside a material.

Throughout this thesis, complex notation is used to represent monochromatic waves. The time domain fields, written in script font, are related to the complex fields, written in straight font, by the relation $\bar{\mathcal{E}} = \Re\{\bar{E} e^{-i\omega t}\}$, where ω is the angular frequency of the incident laser field and $\Re$ denotes the real part. Because of (1.2), the constitutive relations for the complex fields are

$$\bar{D} = \epsilon \bar{E} \tag{1.3a}$$

$$\bar{B} = \mu \bar{H}. \tag{1.3b}$$

Time-average quantities are denoted by brackets such as $< \bar{S} >= \frac{1}{2}\Re\{\bar{E} \times \bar{H}^*\}$ and * represents the complex conjugate operator. Vectors are given one bar $\bar{E}$, tensors have two bars $\bar{\bar{T}}$, and scalars like ρ are written without bars.

1.2.2 Theoretical framework

In order to precisely model experimental observations, it is necessary to outline a theoretical framework for the application of energy and momentum conservation theorems. To accomplish this, the subsystem concept is introduced in a manor that is

similar to the analysis of Penfield and Haus [53]. In general, we may write the energy and momentum equations for a subsystem as

$$\phi_j = -\nabla \cdot \bar{S}_j - \frac{\partial}{\partial t} W_j \tag{1.4a}$$

$$\bar{f}_j = -\nabla \cdot \bar{\bar{T}}_j - \frac{\partial}{\partial t} \bar{G}_j, \tag{1.4b}$$

where the subscripts denote the j^{th} subsystem. In (1.4), ϕ_j gives the energy transferred to and from other subsystems, $\bar{S}_j$ is the energy flux, $\bar{W}_j$ is the energy density, $\bar{f}_j$ is a force density representing the momentum transfer to or from other subsystems, $\bar{\bar{T}}_j$ is the momentum flux, and $\bar{G}_j$ is the momentum density. In order for momentum and energy to be conserved, the overall system must be expanded such that the interaction terms are zero. That is, the energy and momentum of the system is conserved if we include enough subsystems such that

$$\sum_j \phi_j = 0 \tag{1.5a}$$

$$\sum_j \bar{f}_j = 0. \tag{1.5b}$$

The meaning of (1.5) is that there is no energy or momentum leaving the expanded system. The definition of a particular subsystem depends upon the equations applied to model the physics. It is certainly possible to combine subsystems into larger subsystems or to rearrange terms from one subsystem to another. Because of this, there are different subsystems which can be defined which include the electromagnetic fields. Depending upon the formulation applied, different expressions for the quantities in (1.4) will be obtained to represent the electromagnetic subsystem. The difference between the energy and momentum equations for these subsystems fundamentally rests in how we separate the primary field from the response field of the matter. In this regard, we may view an electromagnetic force density as being related to particular momentum flux and momentum density. In what follows, the

Maxwell-Minkowski subsystem is studied within a stationary, unbounded medium.

The standard form of the Lorentz force density $\rho\bar{\mathcal{E}} + \bar{\mathcal{J}} \times \bar{\mathcal{B}}$ gives the force on free charge density ρ and free current density $\bar{\mathcal{J}}$ due to the presence of electromagnetic fields. According to the Maxwell-Minkowski equations given in (1.1) the dissipated energy and Lorentz force are given by

$$\begin{aligned} \bar{\mathcal{E}} \cdot \bar{\mathcal{J}} &= -\bar{\mathcal{E}} \cdot \frac{\partial \bar{\mathcal{D}}}{\partial t} - \bar{\mathcal{H}} \cdot \frac{\partial \bar{\mathcal{B}}}{\partial t} + (\nabla \times \bar{\mathcal{H}}) \cdot \bar{\mathcal{E}} - (\nabla \times \bar{\mathcal{E}}) \cdot \bar{\mathcal{H}} && \text{(1.6a)} \\ \rho\bar{\mathcal{E}} + \bar{\mathcal{J}} \times \bar{\mathcal{B}} &= -\frac{\partial \bar{\mathcal{D}}}{\partial t} \times \bar{\mathcal{B}} + \frac{\partial \bar{\mathcal{B}}}{\partial t} \times \bar{\mathcal{D}} + (\nabla \times \bar{\mathcal{H}}) \times \bar{\mathcal{B}} + (\nabla \times \bar{\mathcal{E}}) \times \bar{\mathcal{D}} && \text{(1.6b)} \\ &+ (\nabla \cdot \bar{\mathcal{B}})\bar{\mathcal{H}} + (\nabla \cdot \bar{\mathcal{D}})\bar{\mathcal{E}}. && \text{(1.6c)} \end{aligned}$$

These equations can be written in the form of (1.4) by applying the appropriate vector calculus identities. The resulting Minkowski energy and momentum equations for a linear, isotropic, and non-dispersive medium are

$$\begin{aligned} \bar{\mathcal{E}} \cdot \bar{\mathcal{J}} &= -\nabla \cdot \left[\bar{\mathcal{E}} \times \bar{\mathcal{H}}\right] - \frac{\partial}{\partial t}\left[\frac{1}{2}\left(\bar{\mathcal{D}} \cdot \bar{\mathcal{E}} + \bar{\mathcal{B}} \cdot \bar{\mathcal{H}}\right)\right] && \text{(1.7a)} \\ \rho\bar{\mathcal{E}} + \bar{\mathcal{J}} \times \bar{\mathcal{B}} &= -\nabla \cdot \left[\frac{1}{2}\left(\bar{\mathcal{D}} \cdot \bar{\mathcal{E}} + \bar{\mathcal{B}} \cdot \bar{\mathcal{H}}\right)\bar{\bar{I}} - \bar{\mathcal{D}}\bar{\mathcal{E}} - \bar{\mathcal{B}}\bar{\mathcal{H}}\right] - \frac{\partial}{\partial t}\left[\bar{\mathcal{D}} \times \bar{\mathcal{B}}\right], && \text{(1.7b)} \end{aligned}$$

where $\bar{\bar{I}}$ is the identity dyad. Note that the limitation to non-dispersive media is lifted in Chapter 3. In a lossless and source free region of an unbounded medium the energy and momentum equations in (1.7) represent a closed system since $\bar{\mathcal{J}} \cdot \bar{\mathcal{E}} = 0$ and $\rho\bar{\mathcal{E}} + \bar{\mathcal{J}} \times \bar{\mathcal{B}} = 0$. However, if $\rho \neq 0$ and/or $\bar{\mathcal{J}} \neq 0$, the subsystem given by (1.7) does not represent a closed system. Therefore, at least one other subsystem must be added to close the system. The resulting force acts upon the charge carriers inside the medium. It is useful to consider the experimentally observed force density $\rho(\bar{\mathcal{E}} + \bar{v} \times \bar{\mathcal{E}})$ on a collection of charged particles with charge density ρ, mass density

m, and velocity field $\bar{v}$. Consider the dynamics of all charge carriers

$$-\bar{\mathcal{E}} \cdot \bar{\mathcal{J}} = -\frac{\partial}{\partial t}\left[\frac{1}{2} m\bar{v} \cdot \bar{v}\right] \tag{1.8a}$$

$$-\rho\bar{\mathcal{E}} - \bar{\mathcal{J}} \times \bar{\mathcal{B}} = -\frac{\partial}{\partial t}\left[m\bar{v}\right], \tag{1.8b}$$

which closes the system when added to (1.7). In this closed system, the kinetic energy of the particles $\frac{1}{2}m\bar{v} \cdot \bar{v}$ and momentum of the particles $m\bar{v}$ are altered by the presence of the electromagnetic fields. Therefore, the dynamics of the system of charged particles can be deduced either by evaluating the force density $\rho\bar{\mathcal{E}} + \bar{\mathcal{J}} \times \bar{\mathcal{B}}$ or by applying the Minkowski momentum flux and momentum density in (1.7).

The preceding analysis raises a very important question regarding the remainder of this thesis. It is assumed up front that the materials considered here are stationary. However, imparting momentum to a material body implies that the momentum of the material will change with time according to $\partial(m\bar{v})/\partial t$. For example, consider the classic case of a monochromatic plane wave incident normally upon a perfect electrical conductor (PEC) mirror from free space. The solution of this problem assuming a stationary mirror shows that the energy of the wave is conserved, and the momentum imparted to the mirror is twice the incident wave momentum [39]. To reconcile the fact that the momentum change will accelerate the mirror, thus increasing it's kinetic energy, we must consider the moving boundary. In fact, the reflection of incident electromagnetic momentum will cause the mirror to move away from the incident wave such that the reflected wave is shifted in frequency. The Doppler effect is responsible for the red shift in the reflected wave frequency and the transfer of electromagnetic energy to the mirror [61].

To treat stationary media, the velocity of the material is not simply set to zero. To account for the fact that the solutions seemingly violate conservation of energy, a limiting process is applied. In the limit $\bar{v} \to 0$, the kinetic energy density $\frac{1}{2}m\bar{v} \cdot \bar{v}$ approaches zero faster than does the momentum density $m\bar{v}$. Therefore, the limi-

tation to stationary medium is actually the limit of very small velocity such that smaller material velocity yields a better approximation. Thus, a finite momentum is transferred to the material while the kinetic energy of the material is zero.

1.2.3 Toward reconciliation

In this thesis, I take the position that regardless of which calculation approach is applied, all results must conform to the same predictions of experimentally observable phenomena. In Chapter 2, which begins on page 45, the Lorentz force density and momentum conservation equation are applied to equivalently predict the optical forces on media. While the Lorentz force provides a means to calculate the force density everywhere inside a material once the fields are present, the momentum conservation equation reduces the computation by describing the momentum transfer to lossless media to a surface effect. Also, each method can equivalently distinguish the momentum transfer to free currents due to the attenuation of the wave in a lossy medium. In Chapter 3, which starts on page 79, the momentum of an electromagnetic wave is derived for a lossy, dispersive Lorentz medium. The theory is applied to calculate the reversal of wave momentum in an isotropic medium with negative index of refraction. The optical manipulation of colloidal particles is treated in Chapter 4 starting on page 101. The concept of electromagnetic wave momentum developed in the preceding chapters is applied to predict the behavior of particles suspended in a background medium and subjected to various incident optical fields. Optical binding is studied in Chapter 5 beginning on page 125. The equilibrium positions of multiple cylindrical particles in an optical interference pattern are predicted by applying the multi-scattering code implemented by Dr. Grzegorczyk to calculate the total fields necessary for application of the Maxwell stress tensor. This approach is validated by using a commercial field solver and integrating the Lorentz force over the surface of the cylinders. A more basic description of optical binding is also provided by considering the interaction of multiple slabs incident by a plane electromagnetic wave.

Finally, the conclusions are discussed in Chapter 6 starting on page 149.

1.3 Papers published toward completion of Ph.D.

The results presented in this thesis have been disseminated in refereed journals and at the Progress in Electromagnetics Research Symposium (PIERS). Below, the record of these publications and symposium presentations are listed along with works published as part of the doctoral studies not included within the scope of this thesis.

Journal Papers

B. A. Kemp, J. A. Kong, T. M. Grzegorczyk, "Reversal of wave momentum in isotropic left handed media," *Phys. Rev. A.*, accepted for publication.

B. A. Kemp, T. M. Grzegorczyk, B. I. Wu, and J. A. Kong, "Application of the electrostatic mean value theorem to electrostatic sensor electrodes," *Journal of Electrostatics*, Vol. 65, No. 2, 69-74, 2007.

T. M. Grzegorczyk, B. A. Kemp, and J. A. Kong, "Passive guiding and sorting of small particles with optical binding forces," *Opt. Lett.*, 31, 3378-3380, 2006.

B. A. Kemp, T. M. Grzegorczyk, and J. A. Kong, "Optical momentum transfer to absorbing Mie particles," *Phys. Rev. Lett.*, 97, 133902, 2006.

T. M. Grzegorczyk, B. A. Kemp, and J. A. Kong, "Stable optical trapping based on optical binding forces," *Phys. Rev. Lett.*, 96, 113903, 2006.

T. M. Grzegorczyk, B. A. Kemp, and J. A. Kong, "Trapping and binding of an arbitrary number of cylindrical particles in an in-plane electromagnetic field," *J. Opt. Soc. Am. A*, Vol. 23, No. 9, 2324-2330, 2006.

B. A. Kemp, T. M. Grzegorczyk, and J. A. Kong, "Lorentz force on dielectric and magnetic particles," *J. of Electromagn. Waves and Appl.*, Vol. 20, No. 6, 827-839, 2006.

B. A. Kemp, T. M. Grzegorczyk, and J. A. Kong, "Ab initio study of the radiation pressure on dielectric and magnetic media," *Opt. Express* 13, 9280-9291, 2005.

Conference Papers

A. J. Dumanian, E. C. Burt, and B. A. Kemp, "A Component Model Approach for the RCS Validation of an Electrically Large Open-Ended Cylindrical Cavity," IEEE AP-S International Symposium, Honolulu, HI, 2007.

B. A. Kemp, T. M. Grzegorczyk, and J. A. Kong, "Comparison of methods for the calculation of radiation pressure on dielectric and magnetic particles," Progress in Electromagnetics Research Symposium, PIERS-2006, Cambridge, MA.

B. A. Kemp, T. M. Grzegorczyk, B. I. Wu, and J. A. Kong, "Three satellite geolocation from TDOA and FDOA measurements," Progress in Electromagnetics Research Symposium, PIERS-2006, Cambridge, MA.

B. A. Kemp, T. M. Grzegorczyk, and J. A. Kong, "Optimal sensor placement for the localization of an electrostatic source," Progress in Electromagnetics Research Symposium, PIERS-2006, Cambridge, MA.

T. M. Grzegorczyk, B. A. Kemp, and J. A. Kong, "Theory and modeling of optical forces within a collection of Mie scatterers," Progress in Electromagnetics Research Symposium, PIERS-2006, Cambridge, MA.

Chapter 2

Electromagnetic Theory of Optical Forces

Recently, the radiation pressure exerted by an electromagnetic wave impinging upon a dielectric body was derived by the direct application of the Lorentz law [43]. This method applies the Lorentz force to bound currents distributed throughout the medium and bound charges at the surface of the medium. The approach allows for the computation of force at any point inside a dielectric [43, 45, 46] and has been shown applicable to numerical methods, such as the finite-difference-time-domain (FDTD) [44, 57]. A similar approach was taken to study the radiation pressure on a dielectric surface [41] and a semiconductor exhibiting the photon drag effect [42]. Direct comparison with the stress tensor divergence has not been done previously in the regime of optical momentum transfer. Two important generalizations of the method proposed in [43] are introduced that allow for the calculation of forces on linear, isotropic media. First, the force on bound and free magnetic currents and bound magnetic charges are introduced to the distributed Lorentz force to model magnetic materials. Including magnetization in the model is important because materials have recently been developed with magnetic response into the Terahertz [58] and opti-

cal [59] frequencies which offer hope for future experiments of optical momentum transfer in magnetic media. The second generalization allows for the discrimination of the force on free carriers so that experimental observation of momentum transfer to lossy media can be modeled. This is an important contribution since all media is inherently lossy. An equivalent view of momentum transfer is developed and formalized via the Maxwell stress tensor. The viewpoints and physical predictions of the two approaches are compared and contrasted.

2.1 Lorentz force and momentum conservation

The Maxwell-Chu equations for a time-harmonic field in a source free region

$$\nabla \times \bar{H} + i\omega\epsilon_0 \bar{E} = -i\omega \bar{P} \tag{2.1a}$$

$$\nabla \times \bar{E} - i\omega\mu_0 \bar{H} = i\omega\mu_0 \bar{M} \tag{2.1b}$$

$$\nabla \cdot \mu_0 \bar{H} = -\nabla \cdot \mu_0 \bar{M} \tag{2.1c}$$

$$\nabla \cdot \epsilon_0 \bar{E} = -\nabla \cdot \bar{P} \tag{2.1d}$$

are deduced from the Maxwell-Minkowski equations by defining a polarization $\bar{P} = \bar{D} - \epsilon_0 \bar{E}$ and magnetization $\mu_0 \bar{M} = \bar{B} - \mu_0 \bar{M}$ to model stationary media. A momentum conservation equation is obtained by adding (2.1a) cross multiplied by $\mu_0 \bar{H}^*$, (2.1b) cross multiplied by $\epsilon_0 \bar{E}^*$, (2.1c) multiplied by $\bar{H}^*$, and (2.1d) multiplied $\bar{E}^*$. After taking one-half of the real part, the equation reduces to [53]

$$< \bar{f} >= -\frac{1}{2} \Re \left\{ \nabla \cdot \bar{\bar{T}} \right\}. \tag{2.2}$$

In (2.2), $< \bar{f} >$ is the average Lorentz force on bound and free currents and charges to be discussed shortly and

$$\bar{\bar{T}} = \frac{1}{2}(\epsilon_0 |\bar{E}|^2 + \mu_0 |\bar{H}|^2)\bar{\bar{I}} - \epsilon_0 \bar{E}\bar{E}^* - \mu_0 \bar{H}\bar{H}^* \tag{2.3}$$

takes the form of the free-space Maxwell stress tensor [55], where $\bar{E}\bar{E}$ is a dyadic product and $\bar{\bar{I}}$ is the identity dyad. To calculate the total force $< \bar{F} >$ on a medium, the force density $< \bar{f} >$ is integrated over the entire volume V occupied by the material. Applying the divergence theorem allows the total force on a material medium to be written as a surface integral of the free-space Maxwell stress tensor over an area A enclosing the material body

$$< \bar{F} >= -\frac{1}{2}\Re\left\{ \oint_A dA \left[\hat{n} \cdot \bar{\bar{T}}\right] \right\}, \tag{2.4}$$

where $\hat{n}$ is the outward pointing unit vector on A. The momentum transfer to a material body surrounded by free space can be determined unambiguously since there is no debate regarding the free space electromagnetic momentum.

Application of the Maxwell stress tensor provides the viewpoint that electromagnetic waves posses momentum that may be transferred to material objects via scattering. An alternate viewpoint states that the force exists everywhere in a medium once the fields are present. The force density

$$< \bar{f} >= \frac{1}{2}\Re\{(-\nabla \cdot \bar{P})\bar{E}^* + (-\nabla \cdot \mu_0 \bar{M})\bar{H}^* - i\omega \bar{P} \times \mu_0 \bar{H}^* + i\omega\mu_0 \bar{M} \times \epsilon_0 \bar{E}^*\} \tag{2.5}$$

may be integrated over the entire region occupied by the material. It is interesting to note that (2.5) gives the force on the equivalent electric current density $\bar{J}_e = -i\omega\bar{P}$ as $\bar{J}_e \times \mu_0 \bar{H}^*$, not $\bar{J}_e \times \bar{B}^*$. However, (2.5) may be written, with the replacements $\epsilon_0 \bar{E} = \bar{D} - \bar{P}$ and $\mu_0 \bar{H} = \bar{B} - \mu_0 \bar{M}$, as

$$\begin{aligned} < \bar{f} > &= \frac{1}{2}\Re\{(-\nabla \cdot \bar{P})\bar{E}^* + (-\nabla \cdot \mu_0 \bar{M})\bar{H}^* - i\omega \bar{P} \times \bar{B}^* + i\omega\mu_0 \bar{M} \times \bar{D}^* \\ &+ i\omega \bar{P} \times \mu_0 \bar{M}^* - i\omega\mu_0 \bar{M} \times \bar{P}^*\}. \end{aligned} \tag{2.6}$$

It is obvious that the last two terms cancel due to the $\Re$ operator. Thus, using (2.1c)

and (2.1d), the force density is expressed as

$$< \bar{f} > \;=\; \frac{1}{2}\Re\{\epsilon_0(\nabla\cdot\bar{E})\bar{E}^* + \mu_0(\nabla\cdot\bar{H})\bar{H}^* - i\omega\bar{P}\times\bar{B}^* + i\omega\mu_0\bar{M}\times\bar{D}^*\}. \quad (2.7)$$

The Lorentz force can be applied directly to bound and free currents and charges, which are used to model lossy media with complex permittivity $\epsilon = \epsilon_R + i\epsilon_I$ and permeability $\mu = \mu_R + i\mu_I$ in a free space background (ϵ_0, μ_0). The force on free electric currents is separated based on the imaginary part of the dielectric constant [42]. Thus, the electric current density $-i\omega\bar{P} = -i\omega(\epsilon - \epsilon_0)\bar{E}$ is separated into a bound electric current density $-i\omega(\epsilon_R - \epsilon_0)\bar{E}$ and a free electric current density $\omega\epsilon_I\bar{E}$. A similar separation is made for μ so that the time-average Lorentz force density on bound currents and charges is

$$\begin{aligned} < \bar{f}_b > \;&=\; \frac{1}{2}\Re\Big\{\epsilon_0(\nabla\cdot\bar{E})\bar{E}^* + \mu_0(\nabla\cdot\bar{H})\bar{H}^* \\ &-\; i\omega(\epsilon_R - \epsilon_0)\bar{E}\times\bar{B}^* + i\omega(\mu_R - \mu_0)\bar{H}\times\bar{D}^*\Big\}. \end{aligned} \quad (2.8)$$

The leading two terms in (2.8) contribute via a surface force density on bound electric and magnetic charges, while the final two terms represent the volume force density on bound electric and magnetic currents. The reason for this is that both $\nabla\cdot\bar{E}$ and $\nabla\cdot\bar{H}$ are zero everywhere except at the boundaries where the spatial derivatives are undefined and need to be supplemented with boundary conditions. The force on bound currents and charges is calculated by the integral of $< \bar{f}_{bulk} >$ over the volume of the medium plus the integral of $< \bar{f}_{surf} >$ over the surface of the medium, where

$$< \bar{f}_{bulk} > \;=\; \frac{1}{2}\Re\Big\{ - i\omega(\epsilon_R - \epsilon_0)\bar{E}\times\bar{B}^* + i\omega(\mu_R - \mu_0)\bar{H}\times\bar{D}^*\Big\} \quad (2.9a)$$

$$< \bar{f}_{surf} > \;=\; \frac{1}{2}\Re\Big\{\rho_e\bar{E}^*_{avg} + \rho_h\bar{H}^*_{avg}\Big\}. \quad (2.9b)$$

The bound electric surface charge density is $\rho_e = \hat{n}\cdot(\bar{E}_{out} - \bar{E}_{in})\epsilon_0$ [43], and, similarly,

the bound magnetic surface charge density is $\rho_h = \hat{n} \cdot (\bar{H}_{out} - \bar{H}_{in})\mu_0$. The fields $(\bar{E}_{in}, \bar{H}_{in})$ and $(\bar{E}_{out}, \bar{H}_{out})$ are the total fields just inside the particle and outside the particle, respectively, and the fields in (2.9b) are given by $\bar{E}_{avg} = (\bar{E}_{out} + \bar{E}_{in})/2$ and $\bar{H}_{avg} = (\bar{H}_{out} + \bar{H}_{in})/2$. In addition to (2.8), the force density on free currents

$$< \bar{f}_c >= \frac{1}{2}\Re\left\{\omega\epsilon_I \bar{E} \times \bar{B}^* - \omega\mu_I \bar{H} \times \bar{D}^*\right\}, \tag{2.10}$$

extends the recent analysis of the photon drag effect [42] to include magnetization, oblique incidence, and arbitrary polarization. Note that $< \bar{f}_c >$ does not have a surface force contribution since the trivial case of a perfect electrical conductor (PEC) is not considered. The total time-average force on the material $< \bar{F} >=< \bar{F}_c > + < \bar{F}_b >$ results from integration of the time-average force densities over the entire medium.

The connection of (2.8) and (2.10) to momentum conservation can be shown by considering a normally incident electromagnetic wave with complex wavenumber $k_z = k_{zR} + ik_{zI}$ transmitted into a medium occupying the half-space $z > 0$. Substitution of the transmitted field $\bar{E} = \hat{y}E_0 e^{-k_{zI}z} e^{ik_{zR}z}$ into (2.8) and (2.10) yields

$$< \bar{f}_b > = -\hat{z}\frac{1}{2}k_{zI}\left[(\epsilon_R - \epsilon_0)|\bar{E}|^2 + (\mu_R - \mu_0)|\bar{H}|^2\right] \tag{2.11a}$$

$$< \bar{f}_c > = \hat{z}\frac{1}{2}k_{zR}\left[\epsilon_I|\bar{E}|^2 + \mu_I|\bar{H}|^2\right]. \tag{2.11b}$$

The negative sign leading the left-hand side of (2.11a) indicates that the force on the bound currents is opposite to the incident wave propagation direction when the medium is optically dense. The force density on free currents can be written as

$$< \bar{f}_c >= \hat{z}\frac{1}{2}\frac{n\omega}{c}\left[\epsilon_I|\bar{E}|^2 + \mu_I|\bar{H}|^2\right] = -\hat{z}\frac{1}{2}\Re\left\{\frac{n}{c}\nabla \cdot \bar{S}\right\}, \tag{2.12}$$

where $n = ck_{zR}/\omega$ is the index of refraction, c is the speed of light in vacuum, and $\bar{S} = \bar{E} \times \bar{H}^*$ is the complex Poynting vector resulting from the application of

Poynting's theorem to the second equality. The result of (2.12) is interpreted for two means of momentum transfer. First, the transfer of momentum at the boundary is due entirely to $\bar{F}_b$ since electromagnetic power is conserved in the reflection/transmission (*i.e.* $\Re\{\nabla \cdot \bar{S}\} = 0$). Second, the transfer of momentum to free currents due to the attenuation of the wave in the medium is given by the divergence of the momentum $\bar{p} = n\bar{S}/c$ in (2.12). Recent experiments confirm this result by showing that the observed transfer of momentum to an atom in a dilute gas is directly proportional to the macroscopic refractive index [52]. This dependence on n has also been observed in the photon drag measurements [60] and was recently analyzed in [42, 46]. It is concluded that the direct dependence of absorbed momentum on the refractive index n holds for both dielectric and magnetic media.

The connection of momentum transfer to bound and free currents is formalized by applying the momentum conservation theorem via the Maxwell stress tensor. The previous derivation for the momentum conservation equation in (2.4) may be repeated using the Maxwell-Minkowski equations

$$\nabla \times \bar{H} + i\omega\bar{D} = \bar{J} \tag{2.13a}$$

$$\nabla \times \bar{E} - i\omega\bar{B} = 0 \tag{2.13b}$$

$$\nabla \cdot \bar{B} = 0 \tag{2.13c}$$

$$\nabla \cdot \bar{D} = \rho. \tag{2.13d}$$

The resulting force density gives the force on free currents $\bar{J}$ and free charges ρ in terms of the Maxwell stress tensor in matter [39]

$$\bar{\bar{T}} = \frac{1}{2}(\bar{D} \cdot \bar{E}^* + \bar{B}^* \cdot \bar{H})\bar{\bar{I}} - \bar{D}\bar{E}^* - \bar{B}^*\bar{H}. \tag{2.14}$$

Also, the introduction of free magnetic charges and currents into (2.13c) and (2.13b), respectively, does not change the form of (2.14). The tensor (2.14) can be applied to

distinguish between $< \bar{F}_b >$ and $< \bar{F}_c >$ by noting the relationship in (2.12).

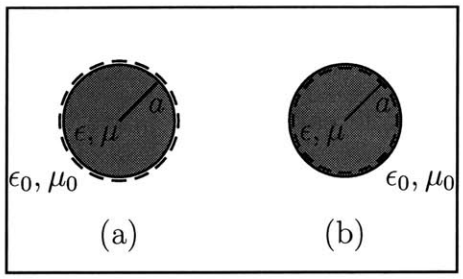

Figure 2-1: Integration path for (2.4) applied to a lossy particle with radius a and (ϵ, μ) in a background of (ϵ_0, μ_0). (a) An integration path that completely encloses the particle gives the total Lorentz force $\bar{F}$. (b) The integration path just inside the boundary gives the force on the free carriers $\bar{F}_c$.

As an example, we consider the force calculation on a particle of radius a. The total Lorentz force $< \bar{F} >$ on bound and free currents is found by integrating a surface in (2.4) that just encloses the entire particle so that $\bar{\bar{T}}$ is evaluated at $r = a^+$ as shown in Fig.2-1(a), and the tensor in (2.14) reduces to the free-space Maxwell stress tensor in (2.3). In fact, it is only necessary that the integration path completely encloses the particle, which is satisfied if $r > a$. The force on free currents $< \bar{F}_c >$ is found by integrating the stress tensor (2.14) along the interior of the particle boundary at $r = a^-$ as shown in Fig.2-1(b) such that all free currents are enclosed. The force on bound currents and charges is $< \bar{F}_b >=< \bar{F} > - < \bar{F}_c >$. The choice of integration paths for $< \bar{F} >$, $< \bar{F}_b >$, and $< \bar{F}_c >$, allow for the description of electromagnetic forces in media consistent with the direct application of the Lorentz force in (2.8) and (2.10).

2.2 Radiation pressure on dielectric and magnetic media

In this section, the momentum transfer due to 1-D material inclusions is calculated by integrating the Lorentz force density over the material and also by applying momen-

tum conservation via the Maxwell stress tensor. The radiation pressure on a lossless slab is calculated first as a simple application of the equations developed in the previous section. Then, the momentum transfer to an absorbing dielectric is found, and the result is applied to reconcile conflicting reports of the radiation pressure on a lossless dielectric half-space by taking the limiting case of zero absorption. The calculations are shown to be in complete accord with relevant measurements, including the deflection of mirrors immersed in a dielectric liquid.

2.2.1 Radiation pressure on a slab

The radiation pressure on a slab due to an incident TE plane wave $\bar{E}_i = \hat{y}E_i e^{ik_{0z}z}e^{ik_x x}$ is calculated using the Lorentz force density and momentum conservation. The slab shown in Fig. 2-2 is characterized by real permeability μ and permittivity ϵ and is surround by free space. The field solution is well known and is given in Appendix A. The problem of a TM polarized wave can be solved by applying the duality principle [39].

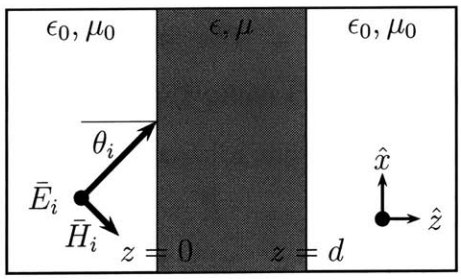

Figure 2-2: TE plane wave incident upon a slab (ϵ, μ) surrounded by free space (ϵ_0, μ_0). The angle of incidence is θ_i and the slab thickness is d.

First, the Lorentz force density on bound currents is applied to calculate the radiation pressure on a dielectric slab due to a plane wave at normal incidence (*i.e.* $\theta_i = 0$). The force density $< \bar{f} >= \frac{1}{2}\Re\{-i\omega\bar{P} \times \bar{B}^*\}$ results in only a z component $< f_z > \equiv \hat{z} \cdot < \bar{f} >$ and is plotted in Fig. 2-3 as a function of position inside the slab for three cases. The force patterns are determined by the standing waves inside the slab. Regions of high force density can be identified in the plots. Furthermore, it

can be seen that parts of the slabs may be either in compression or in tension. For example, Fig. 2-3 (b) shows that the two halves of a half wavelength slab are pulled away from each other by equal amounts so that the total force on the slab is zero. This observation is explored further in Chapter 5 as a explanation of the optical binding. The radiation pressure on each slab is determined by integration over z. Although the integration can be carried out analytically for this simple geometry, it is implemented here numerically as is necessary with more complicated 2-D and 3-D scattering problems. The integration is given by simple discretization in the z coordinate

$$< F_z >= \int_0^d dz \frac{1}{2} \Re\{ -i\omega \bar{P} \times \bar{B}^* \} \approx \sum_{l=1}^{L} \Delta z \frac{1}{2} \Re\{ -i\omega \mu_0 (\epsilon - \epsilon_0) \bar{E}_l \times \bar{H}_l^* \}, \quad (2.15)$$

where $z_1 = 0$, $z_L = d$, and the fields $\bar{E}_l$ and $\bar{H}_l$ are evaluated at z_l.

Momentum conservation can also be used to calculate the radiation pressure on a slab due to oblique incidence. The Maxwell stress tensor is applied at the boundaries of the slab. It is expected that the total radiation pressure results from the incident and scattered (reflected and transmitted) momenta. Since there are no free currents, the total force results completely from the force on bound currents. The force per unit area on the slab of thickness d is, therefore, given by

$$< \bar{F} >= \frac{1}{2} \Re\{ \hat{z} \cdot \bar{\bar{T}}(z = 0^-) - \hat{z} \cdot \bar{\bar{T}}(z = 0^+) + \hat{z} \cdot \bar{\bar{T}}(z = d^-) - \hat{z} \cdot \bar{\bar{T}}(z = d^+) \}, \quad (2.16)$$

where $\bar{\bar{T}}(z = z_0)$ is the Maxwell stress tensor given by (2.14) evaluated at the point

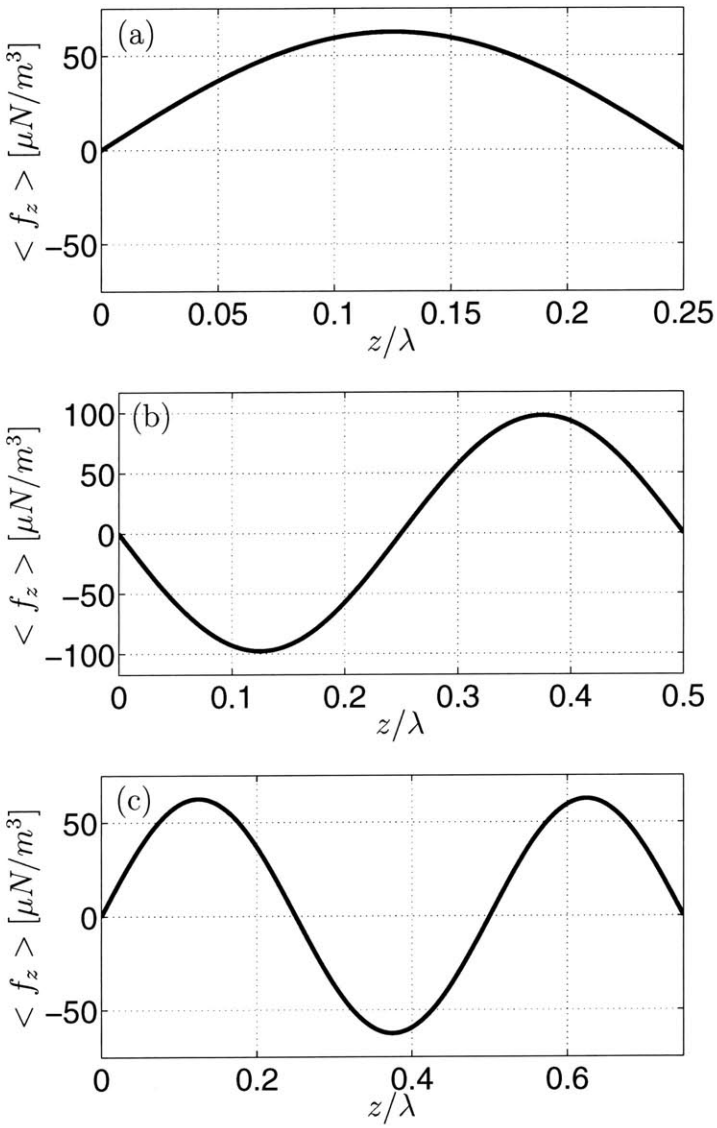

Figure 2-3: Force density inside a dielectric slab due to an in impinging electromagnetic wave of unit amplitude. The electromagnetic wave is incident at $\theta_i = 0$ onto a slab with permittivity $\epsilon = 4\epsilon_0$. The thickness of the slab is normalized to the wavelength inside the material for (a) $d = \lambda/4$, (b) $d = \lambda/2$, and $d = 3\lambda/4$.

$z = z_0$. The contributions from the fields inside the slab are restricted to the terms

$$\hat{z} \cdot \bar{\bar{T}}(z = 0^+) = \hat{z} \left[\frac{\epsilon}{2} |E_y(z = 0^+)|^2 + \frac{\mu}{2} \left(|H_x(z = 0^+)|^2 - |H_z(z = 0^+)|^2 \right) \right] + \hat{x} \left[-\mu H_z(z = 0^+) H_x^*(z = 0^+) \right] \tag{2.17a}$$

$$\hat{z} \cdot \bar{\bar{T}}(z = d^-) = \hat{z} \left[\frac{\epsilon}{2} |E_y(z = d^-)|^2 + \frac{\mu}{2} \left(|H_x(z = d^-)|^2 - |H_z(z = d^-)|^2 \right) \right] + \hat{x} \left[-\mu H_z(z = d^-) H_x^*(z = d^-) \right]. \tag{2.17b}$$

By substitution of the fields in the slab, it can be easily shown that

$$\hat{z} \cdot \bar{\bar{T}}(z = 0^+) = \hat{z} \cdot \bar{\bar{T}}(z = d^-), \tag{2.18}$$

which is expected since the force on free currents is zero. The radiation pressure on the slab reduces to

$$< \bar{F} >= \frac{1}{2} \Re \{ \hat{z} \cdot \bar{\bar{T}}(z = 0^-) - \hat{z} \cdot \bar{\bar{T}}(z = d^+) \}. \tag{2.19}$$

Therefore, the force on a lossless slab can be computed solely from the knowledge of the fields outside the slab. This is to be expected and can be generalized to media of arbitrary geometry since the divergence of the stress tensor applied to continuous, lossless media is zero. Simplification of (2.19) with knowledge of the reflected and transmitted fields gives the closed form expression for force per unit area on the slab

$$< \bar{F} >= \hat{z} \frac{\epsilon_0}{2} |E_i|^2 \cos^2 \theta_i \left[1 + |R_{slab}|^2 - |T_{slab}|^2 \right], \tag{2.20}$$

where θ_i is the incident angle and R_{slab} and T_{slab} are the slab reflection and transmission coefficients, respectively [39]. This analytic expression shows that the $\hat{x}$-component of the radiation pressure on a lossless slab is zero ($F_x = 0$), regardless of incident angle [55]. At normal incidence, the radiation pressure given by (2.20)

can be written simply as the summation of force components $\hat{z}\frac{\epsilon_0}{2}E_i^2$, $\hat{z}\frac{\epsilon_0}{2}E_i^2|R_{slab}|^2$, and $-\hat{z}\frac{\epsilon_0}{2}E_i^2|T_{slab}|^2$ due to the incident, reflected, and transmitted wave momenta, respectively.

Numerical integration of the Lorentz force in (2.15) is applied to calculate the Lorentz force on the slab, and the results are compared with the analytical expression of (2.20). Figure 2-4 shows excellent agreement between the two methods applied to compute the force on a lossless dielectric slab ($\mu = \mu_0, \epsilon = 4\epsilon_0$). The maxima and minima in the force are due to the periodic dependence of the reflection coefficient R_{slab} and the transmission coefficient T_{slab} on the slab thickness. Minimum force is observed for slab thicknesses equal to multiples of half wavelength $m\frac{\lambda}{2}$ and maximum force is observed for slab thicknesses equal to odd multiples of quarter wavelength $(2m+1)\frac{\lambda}{4}$, where λ is the wavelength of the electromagnetic wave inside the slab and $m \in [0, 1, 2, \ldots]$. For comparison, note that for $d = \lambda/4$, $< F_z >= 3.182\ [pN/m^2]$ is calculated using (2.15) and $< F_z >= 3.184\ [pN/m^2]$ is calculated by the application of (2.20), which is in agreement with $< F_z >= 3.188\ [pN/m^2]$ previously calculated using FDTD and the Lorentz force density [44].

Figure 2-5 shows the radiation pressure on a permeable slab ($\mu = 4\mu_0, \epsilon = \epsilon_0$) as a function of incident angle, measured from the surface normal. This example requires the calculation of both magnetic currents from (2.9a) and magnetic surface charge from (2.9b), which are used to compute the Lorentz force. As seen in Fig. 2-5, there is excellent agreement between the two force calculation methods at all incident angles. It is well know that a TM wave incident upon a dielectric surface at the Brewster angle gives zero reflection. By duality, the Brewster angle for total transmission of a TE incident wave is given by [39]

$$\theta_B = \tan^{-1}\sqrt{\frac{\mu}{\mu_0}}, \tag{2.21}$$

and is calculated for this example to be $\theta_B = 63.4°$. This is evident in Fig. 2-5 by the

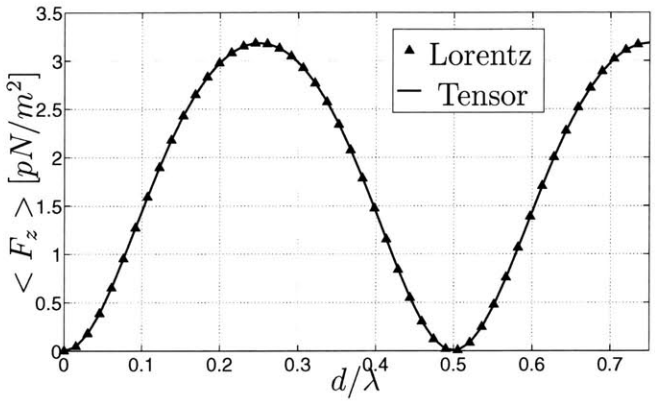

Figure 2-4: Radiation pressure on a dielectric slab as a function of slab thickness. The unit amplitude electromagnetic wave is incident onto a slab with permittivity $\epsilon = 4\epsilon_0$ and thickness $d = \lambda/4$ at $\theta_i = 0$. The pressure is calculated from the divergence of the Maxwell stress tensor (line) or numerical integration of the Lorentz force density (markers). © 2005 Optical Society of America, Inc. [1].

zero force at this particular angle.

The radiation pressure is shown as a function of dielectric constant ϵ/ϵ_0 for a lossless dielectric slab in Fig. 2-6. Again, there is excellent agreement between the two force calculation methods. It is seen that the force goes to zero as expected when the slab is impedance matched to free space $\epsilon = \epsilon_0$. For all positive permittivities, including the region $0 < \epsilon/\epsilon_0 < 1$, the force is in the positive $\hat{z}$-direction, indicating that the force is pushing the slab.

2.2.2 Momentum transfer to absorbing dielectrics

The two methods are applied to model known experiments by considering the general solution of a TE electromagnetic wave obliquely incident on the surface of an infinite nonmagnetic medium ($\mu = \mu_0$) occupying the region $z > 0$. The radiation pressure on bound currents is found by integrating the Maxwell stress tensor in (2.14) along a

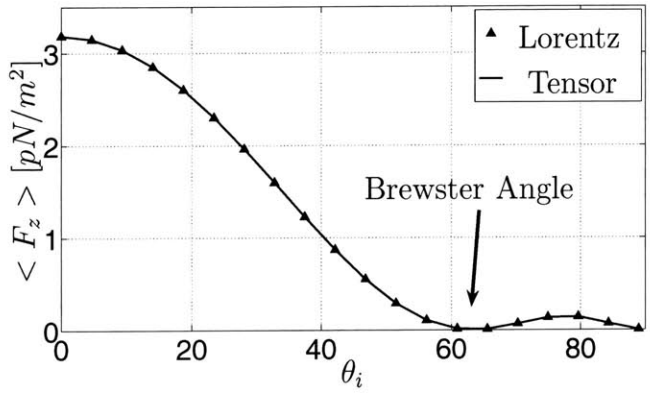

Figure 2-5: Radiation pressure on a dielectric slab as a function of incident angle. The TE polarized, unit amplitude electromagnetic wave is incident onto a slab with permittivity $\epsilon = \epsilon_0$ and permeability $\mu = 4\mu_0$. The thickness of the slab is $d = \lambda/4$. The pressure is calculated from the divergence of the Maxwell stress tensor (line) or numerical integration of the Lorentz force density (markers). © 2005 Optical Society of America, Inc. [1].

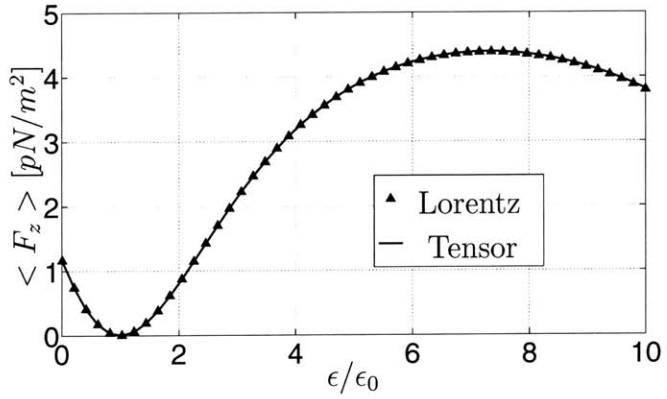

Figure 2-6: Radiation pressure on a dielectric slab as a function of dielectric constant. The unit amplitude electromagnetic wave is incident at $\theta_i = 0$ onto the dielectric slab of thickness $d = \lambda/4$. The pressure is calculated from the divergence of the Maxwell stress tensor (line) or numerical integration of the Lorentz force density (markers). © 2005 Optical Society of America, Inc. [1].

path that just encloses the boundary and, for a weakly absorbing dielectric, is

$$< \bar{F}_b >= \hat{z} E_i^2 \left[\frac{\epsilon_0}{2} \left(1 + |R_{hs}|^2\right) \cos^2\theta_i - \frac{\epsilon_R}{2} |T_{hs}|^2 \cos^2\theta_t \right], \tag{2.22}$$

where R_{hs} is the reflection coefficient, T_{hs} is the transmission coefficient, and θ_i and θ_t are the incident and transmitted angles, respectively. Thus, the total force on bound currents is normal to the surface and directed toward the incoming wave for $\epsilon_R > \epsilon_0$, while the tangential component of wave momentum is conserved across the boundary due to phase matching. To formally prove this assertion, it is necessary to consider the tangential component of the Lorentz force density

$$\hat{x} \cdot < \bar{f}_b >= \frac{1}{2} \Re \Big\{ -i(\epsilon_R - \epsilon_0) k_x^* |E_i|^2 |T|^2 e^{-2k_{zI} z} \Big\}, \tag{2.23}$$

which is due to the transmitted field $\bar{E} = \hat{y} E_i T e^{-k_{zI} z} e^{ik_{zR} z} e^{ik_x x}$. The tangential force density on bound currents in (2.23) is zero when k_x is real, yielding a normal pressure on a half-space void of free currents. The total radiation pressure on an absorbing half-space is found from (2.4) with the tensor integration extended to $z \to \infty$

$$\hat{z} \cdot < \bar{F} > = \frac{\epsilon_0}{2} E_i^2 \left(1 + |R|^2\right) \cos^2\theta_i \tag{2.24a}$$

$$\hat{x} \cdot < \bar{F} > = \frac{\epsilon_0}{2} E_i^2 \left(1 - |R|^2\right) \cos\theta_i \sin\theta_i, \tag{2.24b}$$

which is in agreement with the Lorentz force density integrated over the region $z \in [0, \infty)$ as in [41, 43]. The result (2.24b) was originally demonstrated by Poynting in 1905 [11], who observed a tangential force given by $\frac{\epsilon_0}{2} E_i^2 \sin\theta_i \cos\theta_i$ for a nearly perfect absorbing medium ($R \approx 0$ and $\epsilon_I \neq 0$) and zero tangential force for the reflection from a mirror $|R| = 1$. Thus, the radiation pressure is normal to the surface of a perfect reflector and is given by the force on free currents at the surface $< \bar{F} >=< \bar{F}_c >= \hat{z} \epsilon_0 |E_i|^2 \cos^2\theta_i = \hat{z} \frac{2}{c} < S_i > \cos^2\theta_i$, where $< S_i >= \frac{1}{2} \Re\{E_i H_i\}$ is the average incident Poynting power.

2.2.3 Radiation pressure on a lossless half-space

Calculation of the Lorentz force on a half-space is more involved than what might be expected. For a lossless half-space, the fields propagate inside the medium without attenuation. This poses a problem in finding the radiation pressure by integrating over the Lorentz force from $z = 0$ to $z \to \infty$. Previously, this issue has been sidestepped by introducing a small amount of loss in the medium, applying the distributed Lorentz force, and allowing the losses to approach zero after integration [41, 43]. The problem with this approach is that the momentum transfer to free charges does not approach zero in the lossless limit because of the assumption that the fields approach zero at $z \to \infty$. Some of the wave energy may be lost, such as ohmic losses in a conducting medium, which must be considered when calculating the total force on a material body. This problem will be addressed subsequently.

First, the Maxwell stress tensor is applied to derive the radiation pressure on a dielectric and magnetic medium occupying the region $z > 0$ due to a TE polarized plane wave incident from free space. The wave propagates in the free-space region (μ_0, ϵ_0) with wave vector $\bar{k}_0 = \hat{x}k_x + \hat{z}k_{0z}$ and in the material with wave vector $\bar{k} = \hat{x}k_x + \hat{z}k_z$. Because there are no losses anywhere, the Maxwell stress tensor can be applied via (2.4) along any surface that includes a unit area of the boundary. Also, since the problem is invariant in x and y, the radiation pressure can be calculated by evaluating the stress tensor at discrete points as was done for the slab. The force per unit area on the half space medium is given by

$$< \bar{F} >= \frac{1}{2}\Re\{\hat{z} \cdot \bar{\bar{T}}(z = 0^-) - \hat{z} \cdot \bar{\bar{T}}(z = 0^+)\}. \tag{2.25}$$

The contributions on the two sides of the interface are

$$\hat{z}\cdot\bar{\bar{T}}(z=0^-) = \hat{z}\left[\frac{\epsilon_0}{2}|E_y(z=0^-)|^2 + \frac{\mu_0}{2}\left(|H_x(z=0^-)|^2 - |H_z(z=0^-)|^2\right)\right] + \hat{x}\left[-\mu_0 H_z(z=0^-)H_x^*(z=0^-)\right], \tag{2.26a}$$

$$\hat{z}\cdot\bar{\bar{T}}(z=0^+) = \hat{z}\left[\frac{\epsilon}{2}|E_y(z=0^+)|^2 + \frac{\mu}{2}\left(|H_x(z=0^+)|^2 - |H_z(z=0^+)|^2\right)\right] + \hat{x}\left[-\mu H_z(z=0^+)H_x^*(z=0^+)\right], \tag{2.26b}$$

and the force tangential to the boundary is seen to be

$$< F_x >= \frac{1}{2}\Re\Big\{ -\mu_0 H_z(z=0^-)H_x^*(z=0^-) + \mu H_z(z=0^+)H_x^*(z=0^+)\Big\}. \tag{2.27}$$

Upon substitution of the fields on both sides of the boundary, the tangential force simplifies to

$$< F_x >= \frac{1}{2}E_i^2\frac{k_x}{\omega^2}\Re\left\{\left(\frac{k_{0z}}{\mu_0}\right)^*\left[(1+R_{hs})(1-R_{hs})^* - p_{0t}^*|T_{hs}|^2\right]\right\} \tag{2.28}$$

where the parameter p_{0t} is given by [39]

$$p_{0t} = \frac{\mu_0 k_z}{\mu k_{0z}}. \tag{2.29}$$

The simplification to (2.28) is a direct result of phase matching, which requires k_x to be continuous across the boundary. Applying the formulas $T_{hs} = 1 + R_{hs}$ and $p_{0t}T_{hs} = 1 - R_{hs}$ obtained from the boundary conditions, it immediately follows that

$$p_{0t}^*|T_{hs}|^2 = (1+R_{hs})(1-R_{hs})^* \tag{2.30}$$

so that the tangential force is zero ($F_x = 0$). This result is a direct consequence of the boundary conditions and phase matching at a single interface, and it can be

generalized to multiple interfaces, including the lossless slab discussed previously, the details of which are omitted for brevity. This differs from previous reports of derived nonzero tangential force at a planar boundary [43, 44]. The radiation pressure on a lossless half-space medium is found from (2.25) and simplifies to

$$\bar{F} = \hat{z}|E_i|^2 \left[\frac{\epsilon_0}{2}\cos^2\theta_i \left(1 + |R_{hs}|^2\right) - \frac{\epsilon}{2}\cos^2\theta_t T_{hs}^2\right], \tag{2.31}$$

where θ_t is the transmitted angle found from Snell's law. Note that this equation also accounts for $\mu \neq \mu_0$, the contribution of which appears in the reflection and transmission coefficients. Again we can see the contribution from the incident, reflected, and transmitted wave momenta to the force on the medium. In this regard, the transmitted momentum is different from the free space momentum due to the response of the material. This is discussed extensively in the next chapter.

Equation (2.31) is applied to evaluate the radiation pressure on the half-space medium due to a normal incident plane wave. By taking the limit $\epsilon \to \infty$, it is simple to show that the radiation pressure approaches

$$\lim_{\epsilon\to\infty} < \bar{F} >= -\hat{z}\epsilon_0 E_i^2. \tag{2.32}$$

This limit is seen in Fig. 2-7 where $E_i = 1V/m$ such that $< F_z > \to -\epsilon_0(1V/m) = -8.85\ [pN/m^2]$ for very large ϵ. Thus, the force of a normally incident plane wave on a lossless dielectric half-space is pulling toward the incoming wave, while in the slab case the plane wave pushes the medium in the wave propagating direction. Likewise, the analytical limit of $\epsilon \to 0$ gives

$$\lim_{\epsilon\to 0} \bar{F} = +\hat{z}\epsilon_0 E_i^2, \tag{2.33}$$

which is also seen in Fig. 2-7.

The analytical expression (2.31) differs from (2.24a) and (2.24b), which retain

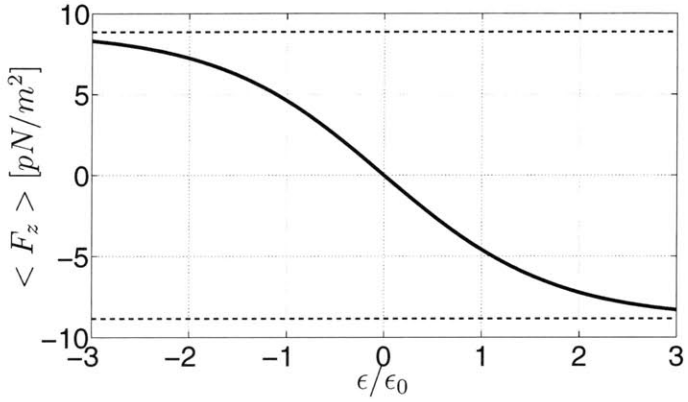

Figure 2-7: Pressure due to an electromagnetic wave incident at $\theta_i = 0$ upon a lossless half-space medium as calculated from the Maxwell stress tensor. The $\hat{z}$-directed force is shown as a function of the relative permittivity ϵ/ϵ_0. The free space wavelength is $\lambda_0 = 640nm$ and $\mu = \mu_0$, $E_i = 1\ V/m$. The incident media (region 0) is free space. The dotted lines denote $\pm\epsilon_0 E_i^2 = \pm 8.85\ pN/m^2$. © 2005 Optical Society of America, Inc. [1].

their form in the limiting case of a lossless medium [41, 43]. In particular, (2.24a) and (2.24b) produce different values from (2.31) for three cases involving a lossless half-space. First, for an impedance matched interface such as a fictive interface between two free space media, $R_{hs} = 0$, which would yield a nonzero value of $< F_z >= \hat{z}\frac{\epsilon_0}{2}E_i^2$. Since such a fictive boundary could be placed anywhere, it would indicate that forces in free space are present everywhere. Second, a nonzero tangential force $< F_x > \neq 0$ at oblique incidence [43] disagrees with the zero sheering force predicted by (2.31) and Stratton [55]. Third, the predicted normal force $< F_z >$ is always positive for a lossless dielectric, which contradicts the known theory that the force of a normally incident plane wave on a lossless half-space is pulling toward the incident wave [39, 61].

The differing results obtained from the distribution of Lorentz force and the Maxwell stress tensor do not imply that either result is incorrect. Instead, we interpret the force on a semi-infinite half-space obtained from the method of [43] to be the total Lorentz force on all bound and free charges and currents with the assump-

tion that the fields attenuate to zero as $z \rightarrow \infty$ due to some finite loss. This holds once the force density is integrated, even if the losses approach zero. To illustrate this point, the force on a lossless half-space due to a normally incident wave can be computed from the distributed Lorentz force by considering the ohmic loss due to the conductivity $\sigma \equiv \omega\epsilon_I$ in a slightly lossy medium. Some of the energy transferred from the wave to the conduction current $\bar{J}_c$ is dissipated as ohmic loss. The time average power dissipated is [39]

$$< P_c >= \frac{1}{2}\Re\left\{ \int_V dV \bar{J}_c(\bar{r}) \cdot \bar{E}^*(\bar{r}) \right\}, \tag{2.34}$$

which must be accounted for in computing the momentum transfer. The corresponding momentum transfer to the free-currents due to the attenuation of the wave is given by (2.12). Integrating over the entire medium and allowing the conductivity to approach zero yields

$$< \bar{F}_c >= \lim_{\sigma \rightarrow 0} \frac{1}{2}\Re\left\{ \int_0^\infty dz \left[\hat{z}\frac{n}{c}\left(\bar{J}_c \cdot \bar{E}^*\right)\right] \right\} = \frac{\epsilon}{2} E_i^2 T_{hs}^2. \tag{2.35}$$

This nonzero contribution to the conduction currents is precisely the difference between (2.31) and the result reported by [43] for the normal incidence case. This momentum contribution to the free currents leads to the conclusion that (2.31) is the radiation pressure on a lossless half-space, while (2.24) is interpreted as the total radiation pressure on a half-space with the assumption that the fields attenuate to zero as $z \rightarrow \infty$. To further enforce this point, it is emphasized that the Maxwell stress tensor was applied to derive (2.24). It was only necessary to assume that the fields attenuate to zero at infinity, then the total force given by $< \bar{F} >= \frac{1}{2}\Re\{\bar{\bar{T}}(z = 0^-)\}$ is equivalent to (2.24) and includes nonzero contribution from $< \bar{F}_c >= \frac{1}{2}\Re\{\bar{\bar{T}}(z = 0^+)\}$. In fact, the tangential force (2.24b) is due entirely to $< \bar{F}_c >$ as expected.

2.2.4 Mirrors submerged in dielectrics

A significant amount of attention has been given to the form of the electromagnetic wave momentum in media. Equation (2.12) proves that the momentum transfer to free carriers due to the absorption of electromagnetic energy is proportional to the index of refraction n. This result is confirmed by experimental evidence; the photon drag effect [51, 60] and the photon recoil in a dilute gas of atoms [52] have been interpreted in favor of the Minkowski momentum flux $\bar{p}_M = \frac{n}{c}\bar{S}$ as opposed to the Abraham momentum flux $\bar{p}_A = \frac{1}{nc}\bar{S}$. An alternate mode of experimental research deals with the reflection of electromagnetic waves from mirrors submerged in dielectrics. In 1954, Jones and Richards measured the deflection of reflectors as a function of refractive index of the submerging fluids [49]. The invention of the laser allowed Jones and Leslie in 1978 to improve upon the precision of the original experiment [50]. The observed forces upon the mirrors in the Jones-Richards-Leslie (JRL) experiments were directly proportional to the index of reflection n, thus supporting the Minkowski momentum for the electromagnetic wave.

Recently, this conclusion has been reconsidered by Mansuripur, who shows that the transfer of momentum to the mirror may be the Minkowski value, the Abraham value, or any value between depending upon the phase of the mirror reflection coefficient [62]. Thus, it is argued that the momentum of a photon inside a dielectric host has the arithmetic mean value of the Abraham and Minkowski momenta. This argument is based on the direct application of the Lorentz force to a reflector which is incident by an electromagnetic wave from a dielectric background. The results demonstrate that, for a perfect electrical conductor (PEC) mirror, the electromagnetic pressure on the mirror is equal to the Minkowski momentum flux, while the pressure on a perfect magnetic conductor (PMC) mirror is equal to the Abraham momentum flux. The mirrors used in the JRL experiments are well modeled as PEC, thus the derived results agree with the experiment. However, if the mirrors were PMC, Mansuripur claims that the Abraham momentum would be measured. Here,

the theoretical calculations of [62] are reproduced via the Maxwell stress tensor formalism. Then the results are interpreted to predict that the observed pressure in most experiments will be the Minkowski form, regardless of the phase of the mirror reflection coefficient.

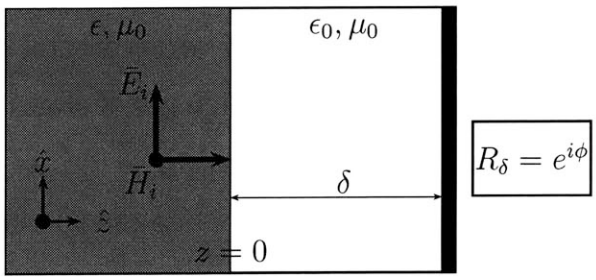

Figure 2-8: TEM plane wave incident upon a reflector. The reflector is defined by $R = e^{i\phi}$ and is separated from the incident dielectric with index of refraction $n = \sqrt{\epsilon/\epsilon_0}$ by an air gap of thickness δ.

The problem under consideration is shown in Fig. 2-8. An electromagnetic wave $\bar{E} = \hat{x}E_i e^{ikz}$ is incident from a dielectric medium with index of refraction $n = \sqrt{\epsilon/\epsilon_0}$ onto a mirror with reflection coefficient $R_\delta = e^{i\phi}$. Since $|R_\delta| = 1$, the properties of the mirror are contained completely within the phase parameter ϕ. It is assumed that an air gap of thickness δ may exist between the dielectric and the mirror, which allows us to completely separate the electromagnetic force on the mirror and the force on the dielectric. However, the problem of a mirror submerged in a dielectric liquid may be treated by simply letting $\delta = 0$.

The electromagnetic force on the mirror is given by the change in electromagnetic momentum at $z = \delta$

$$< \bar{F}_\delta > = \frac{1}{2}\Re\{\hat{z} \cdot \bar{\bar{T}}(z = \delta^-)\} = \frac{1}{2}\Re\{\hat{z} \cdot \bar{\bar{T}}(z = 0^+)\}$$
$$= \hat{z}\frac{1}{2}\left[\frac{\epsilon_0}{2}|E_x(z = 0^+)|^2 + \frac{\mu_0}{2}|H_y(z = 0^+)|^2\right] = \hat{z}\frac{\epsilon_0}{2}\left(|A|^2 + |B|^2\right), \quad (2.36)$$

where the coefficients A and B give the amplitudes of the forward and backward propagating waves in the air gap and are given in terms of the reflection coefficient

R in Appendix A. The force on the mirror surface at $z = \delta$ reduces after some manipulation to

$$< \bar{F}_\delta >= \hat{z}\frac{1}{nc}\left[(1+n^2) + \Re\{R\}(1-n^2)\right] < S_i >, \tag{2.37}$$

where $< S_i >= \frac{1}{2}\Re\{E_i H_i^*\}$ is the average Poynting power of the incident wave, and the real component of the reflection coefficient R is

$$\Re\{R\} = \frac{1 - n^2\tan^2(k_0\delta + \phi/2)}{1 + n^2\tan^2(k_0\delta + \phi/2)}. \tag{2.38}$$

Equations (2.37) and (2.38) show the direct dependence of the radiation pressure on the mirror upon the phase term $k_0\delta + \phi/2$ and are applied to study the momentum transfer to the mirror. In the case of a submerged PEC, $\phi = \pi$ and $\delta = 0$ gives $\Re\{R\} = -1$. Thus, the radiation pressure $< F_\delta >= 2\frac{n}{c} < S_i >$ on the mirror is given by twice the Minkowski momentum flux (the factor of two indicates that the incident momentum is completely reflected). However, the electromagnetic pressure $< F_\delta >= \frac{2}{nc} < S_i >$ on a PMC submerged in a dielectric is twice the Abraham momentum flux since $\phi = 0$ and $\delta = 0$ yields $\Re\{R\} = 1$. Thus Mansuripur's results [62] have been reproduced via the stress tensor formalism and, in the discussion that follows, an interpretation of these results is given that is different from [62].

Mansuripur argues that the momentum of light inside a dielectric host is has the arithmetic mean of the Abraham and Minkowski momentum since all values within this range are equally likely to be observed in experiments. However, while the dependence upon the phase term $k_0\delta + \phi/2$ is oscillatory, the average value does not take the arithmetic mean of the Abraham and Minkowski momenta in general. This is shown in Fig. 2-9 for a mirror submerged in dielectric ($\delta = 0$). The pressure on the mirror takes on values between the Minkowski momentum and the Abraham momentum depending upon ϕ. As the index of refraction of the mirror is increased from $n = 2$ in Fig. 2-9 (a) to $n = 16$ in Fig. 2-9 (b), the momentum transfer to the

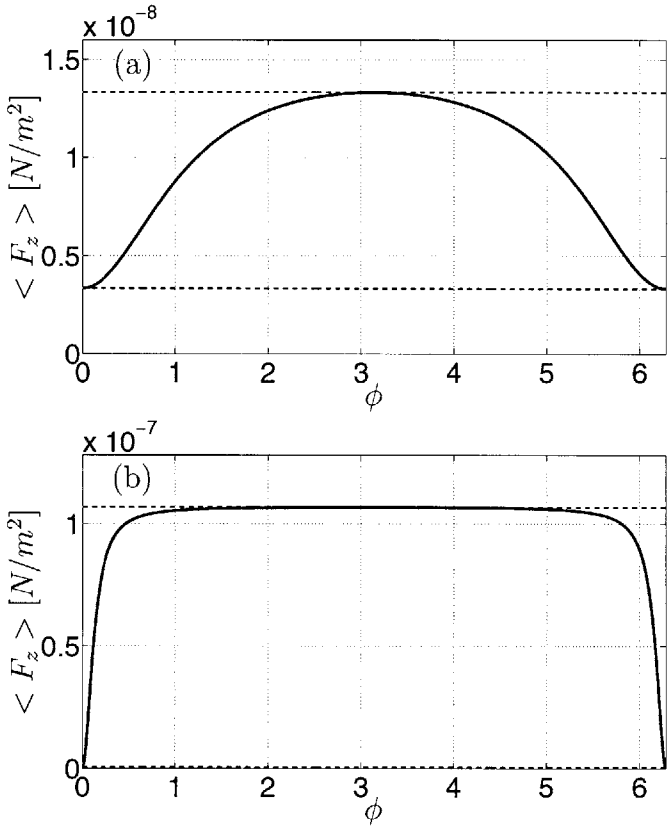

Figure 2-9: Radiation pressure on a mirror submerged in a dielectric ($\delta = 0$) as a function of the phase $\phi \in \{0, 2\pi\}$ of the reflection coefficient $R = e^{i\phi}$. The incident medium is (a) $n = 2$ and (b) $n = 16$. The incident power is unit amplitude at normal incidence $< \bar{S}_i >= \hat{z}$. The radiation pressure oscillates between the upper limit $2p_M = 2\frac{n}{c} < S_i >$ and the lower limit $2p_A = \frac{2}{nc} < S_i >$ represented by the dashed lines.

mirror follows more closely the Minkowski value for a larger range of ϕ. However, the pressure on a PMC retains the association with the Abraham momentum even for large index of refraction.

The pressure of the electromagnetic fields upon the mirror is directly related to the standing wave pattern in the region in front of the mirror. In addition to changing the phase of the reflected wave at the mirror, the standing wave may also be altered by adding an air gap between the dielectric and the mirror. This relationship is given explicitly by the phase term $k_0\delta + \phi/2$ in (2.38) and is illustrated in Fig. 2-

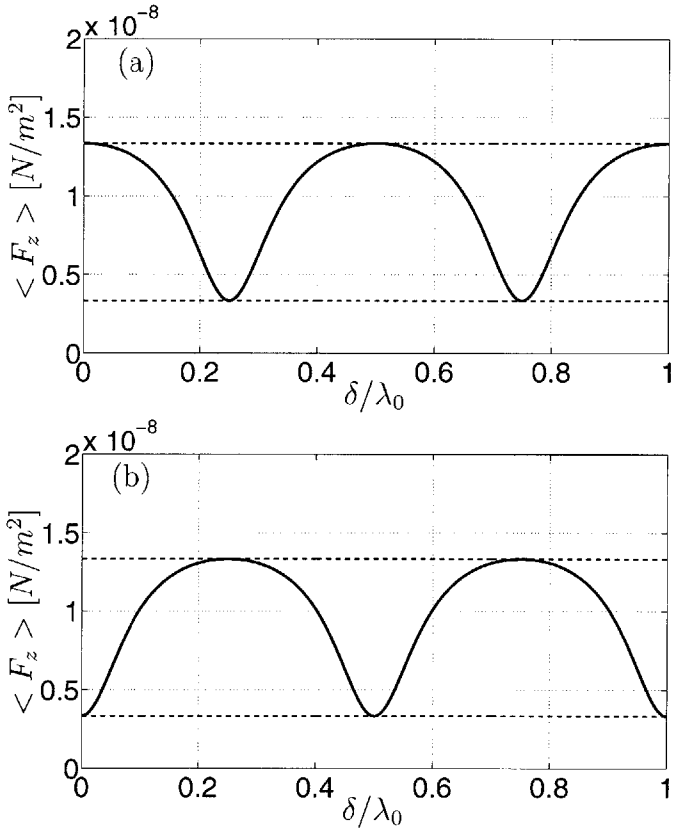

Figure 2-10: Radiation pressure on a mirror submerged ($\delta = 0$) in a dielectric with index of refraction $n = 2$. The incident power is unit amplitude at normal incidence $< \bar{S}_i >= \hat{z}$. The mirror is (a) PEC ($\phi = \pi$) and (b) PMC ($\phi = 0$). The radiation pressure oscillates between the upper limit $2p_M = 2\frac{n}{c} < S_i >$ and the lower limit $2p_A = \frac{2}{nc} < S_i >$ represented by the dashed lines.

10. It is seen that the pressure on the mirror oscillates between the Minkowski and Abraham momentum with a period of $\lambda_0/2$. Indeed, an electromagnetic wave imparts the Minkowski momentum upon a PEC mirror for $\delta = m\lambda_0/2$ ($m = 0, 1, 2, \ldots$). However, the pressure on the PEC mirror is given by the Abraham momentum for $\delta = (2m+1)\lambda_0/4$. This is shown in Fig. 2-10 (a), while the PMC case is simply phase shifted as shown in Fig. 2-10 (b).

The analysis presented here confirms the recent results of Mansuripur [62]. However, while the pressure exerted upon the mirror by the electromagnetic field is un-

questionable, we may still ponder which momentum transfer, Minkowski or Abraham, will be observed in experiment. To answer this question, we must compute the pressure on the dielectric surface at $z = 0$. This force is derived in previous sections and for this particular geometry is given by the momentum balance

$$< \bar{F}_0 >= \hat{z}\left[\frac{\epsilon}{2}|E_i|^2(1+|R|^2) - \frac{\epsilon_0}{2}(|A|^2+|B|^2)\right], \tag{2.39}$$

where the second term is simply the negative of the force on the mirror. Since $|R|^2 = 1$, the pressure on the dielectric reduces to

$$< \bar{F}_0 >= \hat{z}\left\{2\frac{n}{c} - \frac{1}{nc}\left[(1+n^2)+(1-n^2)\Re\{R\}\right]\right\} < S_i > . \tag{2.40}$$

The result of (2.40) implies that there is an additional pressure on the host dielectric which accompanies the pressure on the mirror. If the surface of the dielectric and the mirror are mechanically linked, such as a submerged mirror in a liquid dielectric (*i.e.* $\delta = 0$), the total force on the interface is $< \bar{F} >=< \bar{F}_\delta > + < \bar{F}_0 >= \hat{z}2\frac{n}{c} < S_i >$. Thus, it is predicted that in most experiments the Minkowski momentum will be observed regardless of the mirror reflection coefficient phase ϕ. In the previous examples, $< \bar{F}_0 >= 0$ for a submerged PEC ($\delta = 0$, $\phi = \pi$), while $< \bar{F}_0 >= \hat{z}2\frac{n^2-1}{nc} < S_i >$ restores the total force on a submerged PMC ($\delta = 0$, $\phi = 0$) to twice the Minkowski momentum.

This result can be obtained simply by applying the concept of electromagnetic wave momentum introduced by Gordon [21]. In this regard, we may apply the Maxwell-Minkowski stress tensor $\bar{\bar{T}}(\bar{r})$ in (2.14) directly to predict many experimental observations, and, in the process, reduce greatly the complexity in analysis. Thus, we may model the momentum transfer to objects submerged in dielectrics by applying an effective wave momentum while treating the background medium as a reference.

For example, the effective pressure on the submerged mirror with $\delta = 0$ is

$$< \bar{F} > = \frac{1}{2}\Re\{\hat{z} \cdot \bar{\bar{T}}(z = 0^-) - \hat{z} \cdot \bar{\bar{T}}(z \to \infty)\}. \tag{2.41}$$

We may assume that the fields are zero as $z \to \infty$ due to the mirror, but in reality, we only need to suppose that the fields are sufficiently small on the unilluminated side of the mirror. Thus, the pressure is simply

$$\begin{aligned} < \bar{F} > &= \hat{z}\frac{1}{2}\Re\left\{\frac{\epsilon}{2}|E_x|^2 + \frac{\mu}{2}|H_y|^2\right\} \\ &= \hat{z}\left[\frac{\epsilon}{4}(1 + e^{i\phi})(1 + e^{-i\phi}) + \frac{\mu}{4}\frac{\epsilon}{\mu}(1 - e^{i\phi})(1 - e^{-i\phi})\right] \\ &= \hat{z}2\frac{n}{c} < S_i >, \end{aligned} \tag{2.42}$$

which is twice the Minkowski momentum and is independent of ϕ. Thus, we may apply the conservation of electromagnetic wave momentum to calculate the effective momentum transfer to the mirror, which may include force contributions to the surrounding medium. This concept of wave momentum will be discussed thoroughly in Chapter 3 and applied in Chapter 4 and Chapter 5 to model the optical manipulation of particles in a dielectric medium.

2.3 An alternate formulation

Although the Abraham-Minkowski controversy has been debated for the better part of a century, researchers have gradually become less concerned with the identification of a single form for the momentum density. Instead, focus has shifted to the separation of electromagnetic field and material subsystems in the framework of momentum conservation [21, 38, 53, 63–67]. In this regard, it is accepted that the Minkowski momentum, which has been directly observed in experiments [49–52, 60], includes contributions from both the electromagnetic fields and the response of the medium.

While the electromagnetic contribution to the momentum density was originally assumed to be the Abraham form [21, 63, 64], some reports [38, 65–67] assign $\epsilon_0 \bar{E} \times \bar{B}$ as the component of the momentum density residing in the fields; the difference between these two forms originates from the choice of formulation for the Maxwell equations.

Alternatively, the previous sections have demonstrated that the Lorentz force can be applied directly to media via bound and free currents and charges, thus avoiding *a priori* assumptions of momentum [41–43]. However, various formulations of the electromagnetic theory have been applied to derive different expressions for the force densities, and each may be associated with a particular momentum stress tensor and momentum density vector. The Amperian, Chu, and Minkowski formulations are the most widely used and differ in how matter is modeled in the Maxwell equations [39]. The Amperian formulation, which is also called the EB representation, models matter as electric currents and charges and has been proposed as a suitable basis for the force on matter [67, 68]. In contrast, the Chu formulation, which is also referred to EH representation, treats matter as a combination of electric and magnetic charges and currents. The Maxwell-Chu theory has also been applied to predict the force on matter [69]. The Minkowski formulation, on the other hand, makes no claims to the separation of fields and matter. In fact, the source terms in the Minkwoski formulation represent the free charges and currents. In this section, the Amperian formulation is applied to develop an alternate form of the Lorentz force. A simple argument is given to prove the equivalence of this form of the average force on matter.

The contribution of matter in the Amperian formulation is expressed in terms of the electric current density $\bar{\mathcal{J}}_{eb} = \partial \bar{\mathcal{P}}/\partial t + \nabla \times \bar{\mathcal{M}}$ and the electric charge density

Table 2.1: Summary of momentum stress tensors and momentum densities.

	Momentum Stress Tensor	Momentum Density
Minkowski	$\frac{1}{2}\left(\bar{\mathcal{D}}\cdot\bar{\mathcal{E}}+\bar{\mathcal{B}}\cdot\bar{\mathcal{H}}\right)\bar{\bar{I}}-\bar{\mathcal{D}}\bar{\mathcal{E}}-\bar{\mathcal{B}}\bar{\mathcal{H}}$	$\bar{\mathcal{D}}\times\bar{\mathcal{B}}$
Chu	$\frac{1}{2}\left(\epsilon_0\bar{\mathcal{E}}\cdot\bar{\mathcal{E}}+\mu_0\bar{\mathcal{H}}\cdot\bar{\mathcal{H}}\right)\bar{\bar{I}}-\epsilon_0\bar{\mathcal{E}}\bar{\mathcal{E}}-\mu_0\bar{\mathcal{H}}\bar{\mathcal{H}}$	$\epsilon_0\mu_0\bar{\mathcal{E}}\times\bar{\mathcal{H}}$
Amperian	$\frac{1}{2}\left(\epsilon_0\bar{\mathcal{E}}\cdot\bar{\mathcal{E}}+\bar{\mathcal{B}}\cdot\bar{\mathcal{B}}/\mu_0\right)\bar{\bar{I}}-\epsilon_0\bar{\mathcal{E}}\bar{\mathcal{E}}-\bar{\mathcal{B}}\bar{\mathcal{B}}/\mu_0$	$\epsilon_0\bar{\mathcal{E}}\times\bar{\mathcal{B}}$

$\rho_{eb}=\nabla\cdot\bar{\mathcal{P}}$ in a region free of sources. The Maxwell-Amperian equations are [39]

$$\nabla\times\frac{1}{\mu_0}\bar{\mathcal{B}}-\epsilon_0\frac{\partial\bar{\mathcal{E}}}{\partial t}=\bar{\mathcal{J}}_{eb} \tag{2.43a}$$

$$\nabla\times\bar{\mathcal{E}}+\frac{\partial\bar{\mathcal{B}}}{\partial t}=0 \tag{2.43b}$$

$$\nabla\cdot\bar{\mathcal{B}}=0 \tag{2.43c}$$

$$\epsilon_0\nabla\cdot\bar{\mathcal{E}}=\rho_{eb}. \tag{2.43d}$$

In the Amperian formulation $\bar{\mathcal{E}}$ and $\bar{\mathcal{B}}$ are regarded as the fundamental fields and the Lorentz force density

$$\bar{f}_{eb}=\rho_{eb}\bar{\mathcal{E}}+\bar{\mathcal{J}}_{eb}\times\bar{\mathcal{B}} \tag{2.44}$$

may be interpreted as relating the mechanical action of the electromagnetic fields on media [68]. The conservation equation derived by substituting the sources on the right-hand side of (2.43) into (2.44) is

$$\bar{f}_{eb}=-\frac{\partial\bar{G}_{eb}}{\partial t}-\nabla\cdot\bar{\bar{T}}_{eb}, \tag{2.45}$$

where the momentum density vector $\bar{G}_{eb}\equiv\epsilon_0\bar{\mathcal{E}}\times\bar{\mathcal{B}}$ and the stress tensor $\bar{\bar{T}}_{eb}\equiv\frac{1}{2}\left(\epsilon_0\bar{\mathcal{E}}\cdot\bar{\mathcal{E}}+\bar{\mathcal{B}}\cdot\bar{\mathcal{B}}/\mu_0\right)\bar{\bar{I}}-\epsilon_0\bar{\mathcal{E}}\bar{\mathcal{E}}-\bar{\mathcal{B}}\bar{\mathcal{B}}/\mu_0$ have been proposed to represent the electromagnetic subsystem [38, 65–67]. Such an interpretation implies the isolation of material contributions on the right-hand side of the Maxwell-Amperian equations (2.43). Likewise, the Chu and Minkowski formulations are associated with momentum density vectors and momentum stress tensors. The associations are summarized in Table 2.1.

The time-average force density resulting from the Amperian formulation is

$$< \bar{f}_{eb} >= \frac{1}{2}\Re\left\{\epsilon_0(\nabla\cdot\bar{E})\bar{E}^* + i\omega\left[\epsilon_0\bar{E} - \frac{\mu}{\mu_0}\epsilon\bar{E} + \frac{1}{\mu_0}(\nabla\mu)\times\bar{H}\right]\times\bar{B}^*\right\}. \quad (2.46)$$

The total time-average Amperian force density $< \bar{F}_{eb} >$ is given by

$$< \bar{F}_{eb} >= \int_V dV\frac{1}{2}\Re\left\{i\omega\bar{E}\times\bar{B}^* - i\omega\frac{\mu}{\mu_0}\epsilon\bar{E}\times\bar{B}^*\right\} + \oint_A dA\frac{1}{2}\Re\left\{\rho_e\bar{E}^*_{ave} + \bar{J}_s\times\bar{B}^*\right\}, \quad (2.47)$$

where the bound surface charge density ρ_e was previously defined and the bound surface current density is

$$\bar{J}_s = \left(\frac{\mu}{\mu_0} - 1\right)\hat{n}\times\bar{H}. \quad (2.48)$$

Thus, the Amperian formulation provides a description of optical forces on matter in terms of surface charge, surface current, volume charge, and volume current. It should be obvious that this formulation provides identical predictions for the time-average force on a material body since it can be equivalently cast in terms of the free space Maxwell stress tensor. That is, all of the stress tensors in Table 2.1 reduce to the same expression when applied to the free space region external to a material body. This has been confirmed via numerical application of (2.47) to various examples. One such example of the radiation pressure on an absorbing slab at oblique incidence is shown in Fig. 2-11. While this formulation provides yet another viewpoint for the force density (*e.g.* the inclusion of bound surface current instead of bound magnetic charges), the prediction of experimental observations is equivalent to the Chu formulation. However, the Chu model is simpler to study and apply due to the duality of the electric and magnetic field models [53]. It will therefore be employed in the following chapter to model the more complicated problem of electromagnetic momentum in dispersive and lossy media.

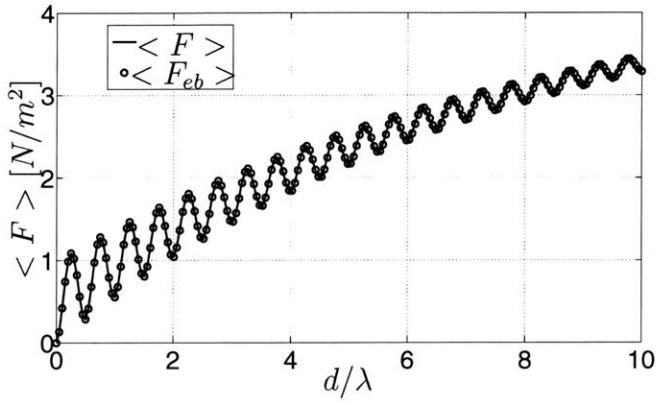

Figure 2-11: Radiation pressure on an absorbing slab as a function of thickness d. The unit amplitude wave is incident at $\theta_i = \pi/6$. The slab is characterized by $\mu = (2 + i0.02)\mu_0$ and $\epsilon = (1 + i0.01)\epsilon_0$, and the thickness is normalized to the wavelength inside the material. The line is computed via the Maxwell stress tensor and the circles represent the force given in (2.47).

2.4 Discussion

The distributed Lorentz force method of [43] was generalized to include contribution from magnetic material. This method was shown to provide results equivalent to those obtained from the application of the Maxwell stress tensor, which was used to derive simple closed form expressions for the force on a lossless slab in equation (2.20) and the force on a lossless half-space in equation (2.31). It was shown that in both cases, the force tangential to the interface is zero. A normally incident plane wave pushes a dielectric slab in the wave propagation direction and pulls a lossless dielectric half-space toward the incident wave [39, 61].

It was shown that the previous application of the distributed Lorentz force to the half-space problem lacks to account for the residual absorption [43]. This is because the fields are assumed to approach zero at infinity, an assumption that holds for a conducting medium in the limit as $\sigma \to 0$. As an example, (2.31) was derived for the normal incidence case from the Lorentz force with consideration given to ohmic energy loss in the conduction current.

A very important contribution contained herein is the separation of force on bound currents and charges and the force on free currents. This separation formalizes a view of momentum transfer in lossy media based on an adiabatic transfer of momentum due to reflection and refraction of the wave and momentum transfer due to absorption inside the medium. This view was applied to explain relevant experiments in terms of an effective electromagnetic wave momentum. The wave momentum includes contributions from both the field and matter as a coupled system, which explains experimental observations of adiabatic momentum transfer to objects immersed in dielectric and magnetic fluids. This concept is extended to dispersive materials and applied to calculate the forces on colloidal particles in the following chapters.

Although the two force calculation methods can be applied to calculate the total force on media, there are inherent advantages and disadvantages for each method. Through numerous examples, [44] demonstrated that the distributed Lorentz method is easily applied to finite-difference time domain (FDTD) computational and can be used to find the forces distributed throughout a host medium. In particular, the tension and compression forces due to a light beam inside a dielectric medium were calculated. In contrast, the advantage of the Maxwell stress tensor is that it reduces a volume integral in three dimensions to a surface integral, thus reducing the computation required to calculate the total force on a material object.

As a concluding note to this chapter, it may not be assumed that the time-domain Chu and Amperian formulations for the force on matter will have the same interpretations for all time. This is discussed in detail by Penfield and Haus in their research monograph, which applies the principle of virtual power to close the overall system [53]. For a broad range of problems, their work ensures that an overall system can be found which conserves energy and momentum. However, the additional subsystems required to form a closed system differ based on which formulation of the Maxwell equations is applied. Thus, the Chu and Amperian subsystems for the electromagnetic waves do not have the same interpretation. A simple illustration of

this point follows.

The Lorentz force $\bar{F}$ is often expressed in terms of the momentum density vector $\bar{G}$ and the Maxwell stress tensor $\bar{\bar{T}}$ as [70]

$$\bar{F} = -\int_V dV\left\{\frac{\partial}{\partial t}\bar{G}\right\} - \oint_A dA\left\{\hat{n}\cdot\bar{\bar{T}}\right\}, \tag{2.49}$$

where the volume V is enclosed by the surface A with outward pointing unit normal vector $\hat{n}$. The issue of "how much electromagnetic momentum is transferred to macroscopic bodies" was recently addressed by considering a spatially finite pulse interacting with a slab [68]. The authors compared different forms of the momentum density vector with the Lorentz force applied directly to media. The isolation of the momentum density vector from the stress tensor is possible since the volume V can be made arbitrarily large so that the fields tend to zero on A [71]. In this case, the force exerted on the media is interpreted according to the choice of $\bar{G}$, which results directly from the formulation of the Maxwell equations applied to separate field and material contributions. The recent theoretical study of the momentum of light pulses in matter favors $\epsilon_0\mu_0\bar{E}\times\bar{H}$ as the momentum of the electromagnetic fields [68]. It is agreed, however, that experimental verification is needed and that such verification could be difficult because of the coupling of momentum between fields and matter [72]. The numerical results of that study show that the predicted pressure on a slab evolves in time differently depending upon which value for the momentum density vector is applied. In all cases however, the total momentum transferred to the slab as $t\to\infty$ approaches the same value as expected [72]. In contrast, the time-average force due to time-harmonic fields results entirely from the stress tensor contribution. Thus, the radiation pressure on a material body in free space can be determined unambiguously by considering the divergence of the free space Maxwell stress tensor. It is, of course, the latter situation that is treated in this thesis.

Chapter 3

Reversal of Wave Momentum in Isotropic LHM

3.1 Negative Index Materials

Left-handed materials (LHM) have received much attention since their realization in 2001 [73] due to interesting physics such as negative refraction [74–76], reversal of the Čerenkov effect [77–80], and the potential to create a perfect lens [81]. However, the reversal of radiation pressure in LHM first predicted in 1968 by Veselago [82] has received much less attention. Veselago's results show that the momentum of an electromagnetic wave

$$< \bar{G} >= \frac{1}{2}\Re\left\{\epsilon\mu\bar{E}\times\bar{H}^{*}+\frac{\bar{k}}{2}\left(\frac{\partial\epsilon}{\partial\omega}|\bar{E}|^{2}+\frac{\partial\mu}{\partial\omega}|\bar{H}|^{2}\right)\right\} \tag{3.1}$$

is antiparallel to the average Poynting power in materials with simultaneously negative permeability μ and permittivity ϵ, giving rise to light attraction instead of light pressure [82]. Researchers still have not observed experimentally the predicted

reversal of electromagnetic wave momentum. Experiments have revealed optical momentum transfer to dielectric media in direct proportion to the macroscopic index of refraction [50–52, 60], but observations have not revealed dependence on the slope of the dielectric function as in (3.1). Furthermore, identification of electromagnetic momentum in media continues to be a controversial subject; various definitions and interpretations have been proposed [21, 38, 40, 43, 65–68].

Recent application of electromagnetic momentum conservation at the interface separating free-space and an isotropic LHM led to the conclusion that the change in momentum of the electromagnetic wave due to refraction must produce a force with a nonzero component directed parallel to the boundary [83]. This sheering force is claimed to be unique to LHM, thus supporting the notion that the tangential component of the momentum is conserved at the boundary separating two right-handed materials (RHM). However, the aforementioned sheering force is predicted to be nonzero because the momentum flux in LHM was assumed to be in the same direction as the power flow, which is in contrast to Veselago's prediction for the momentum density [82]. Thus, electromagnetic wave momentum and radiation pressure in LHM remains topical.

In this chapter, the momentum transfer to isotropic LHM is rigourously treated by applying the classical electromagnetic wave theory. It is argued that previous attempts to describe the momentum of the electromagnetic wave in LHM fail to include material losses and/or dispersion, which cannot be ignored in a causal system with negative index of refraction. We apply the concept of wave momentum, which includes contributions from the material response as proposed by the seminal work of Gordon [21]. The derived expressions define the wave momentum density and wave momentum flux similar to previous derivations for dispersive dielectrics [65, 66]. The results presented here are analogous to the wave energy density and wave energy flux previously derived using the standard Lorentz model for the polarization and magnetization [84]. The Lorentz force is also applied directly to derive the wave momentum

flux density in an LHM half-space resulting from oblique incidence of a monochromatic wave. It is shown that the force tangential to the interface results solely from the momentum transfer as the wave attenuates in the medium. Thus, the tangential component of wave momentum is conserved due to reflection and refraction at the interface of any isotropic medium, and the tangential force on a hypothetical lossless medium is zero regardless of the direction of phase propagation. In the process, we provide a rigorous derivation for the cycle-averaged force on free-currents, which, along with the force on bound currents and charges, gives the total force and describes the details of momentum transfer in lossy media. Furthermore, the force on free currents due to the attenuation of the electromagnetic wave in a material with negative index of refraction is opposite to the direction of power flow.

3.2 Energy and Momentum in Unbounded Media

In order to accurately describe wave propagation in an LHM, it is necessary to include material dispersion and losses. That is, the coupled electromagnetic field and material response must be considered together in determining the form of the energy and momentum of the electromagnetic wave. The equations governing the energy and momentum of an arbitrary subsystem generally take the form [53]

$$\nabla \cdot \bar{S} + \frac{\partial W}{\partial t} = -\varphi \tag{3.2a}$$

$$\nabla \cdot \bar{\bar{T}} + \frac{\partial \bar{G}}{\partial t} = -\bar{f}, \tag{3.2b}$$

where the energy flow $\bar{S}$, energy density $\bar{W}$, momentum flow $\bar{\bar{T}}$, and momentum density $\bar{G}$ interact with other subsystems via φ and $\bar{f}$. In this section, the equations that govern the energy and momentum of the wave are derived from the classical electromagnetic theory and the equations governing the dielectric and magnetic response of a Lorentz medium.

3.2.1 Energy and momentum of the electromagnetic fields

We begin with the Maxwell-Minkowski fields $\bar{\mathcal{E}}(\bar{r},t)$, $\bar{\mathcal{H}}(\bar{r},t)$, $\bar{\mathcal{D}}(\bar{r},t)$, and $\bar{\mathcal{B}}(\bar{r},t)$ in a source free region [39]. The electromagnetic fields and the material response fields are separated by defining the polarization $\bar{\mathcal{P}} \equiv \bar{\mathcal{D}} - \epsilon_0\bar{\mathcal{E}}$ and magnetization $\mu_0\bar{\mathcal{M}} \equiv \bar{\mathcal{B}} - \mu_0\bar{\mathcal{H}}$ for a stationary medium, where the dependence upon space and time is now implied in the notation. The resulting Maxwell-Chu equations [39, 53]

$$\nabla \times \bar{\mathcal{H}} - \epsilon_0 \frac{\partial \bar{\mathcal{E}}}{\partial t} = \frac{\partial \bar{\mathcal{P}}}{\partial t} \equiv \bar{\mathcal{J}}_e \tag{3.3a}$$

$$\nabla \times \bar{\mathcal{E}} + \mu_0 \frac{\partial \bar{\mathcal{H}}}{\partial t} = -\mu_0 \frac{\partial \bar{\mathcal{M}}}{\partial t} \equiv -\bar{\mathcal{J}}_h \tag{3.3b}$$

$$\mu_0 \nabla \cdot \bar{\mathcal{H}} = -\nabla \cdot \mu_0 \bar{\mathcal{M}} \equiv \rho_h \tag{3.3c}$$

$$\epsilon_0 \nabla \cdot \bar{\mathcal{E}} = -\nabla \cdot \bar{\mathcal{P}} \equiv \rho_e \tag{3.3d}$$

give the electromagnetic fields $\bar{\mathcal{E}}$ and $\bar{\mathcal{H}}$ in the presence of the material represented by the source terms $\bar{\mathcal{J}}_e$, $\bar{\mathcal{J}}_h$, ρ_e, and ρ_h. The energy and momentum quantities for the electromagnetic subsystem can be derived without specifying models for $\bar{\mathcal{P}}$ and $\bar{\mathcal{M}}$.

The energy equation is derived in the usual way by subtracting (3.3a) dot multiplied by $\bar{\mathcal{E}}$ from (3.3b) dot multiplied by $\bar{\mathcal{H}}$ and applying the vector identity [39] $\bar{\mathcal{H}} \cdot (\nabla \times \bar{\mathcal{E}}) - \bar{\mathcal{E}} \cdot (\nabla \times \bar{\mathcal{H}}) = \nabla \cdot (\bar{\mathcal{E}} \times \bar{\mathcal{H}})$. The quantities corresponding to the electromagnetic subsystem in (3.2a) are identified as [53]

$$\bar{S}_{eh} = \bar{\mathcal{E}} \times \bar{\mathcal{H}} \tag{3.4a}$$

$$W_{eh} = \frac{\epsilon_0}{2}\bar{\mathcal{E}} \cdot \bar{\mathcal{E}} + \frac{\mu_0}{2}\bar{\mathcal{H}} \cdot \bar{\mathcal{H}} \tag{3.4b}$$

$$\varphi_{eh} = \bar{\mathcal{J}}_e \cdot \bar{\mathcal{E}} + \bar{\mathcal{J}}_h \cdot \bar{\mathcal{H}}, \tag{3.4c}$$

where the subscript eh denotes quantities relating to the electromagnetic subsystem.

Likewise, the equation describing the transfer of momentum to and from the electromagnetic subsystem is derived by adding the cross product of the vector equation (3.3a) and $\mu_0\bar{\mathcal{H}}$, the cross product of the vector equation (3.3b) and $\epsilon_0\bar{\mathcal{E}}$, the

product of the scaler equation (3.3c) and $\bar{\mathcal{H}}$, and the product of the scaler equation (3.3d) and $\bar{\mathcal{E}}$. After some manipulation of the resulting vector equation, the momentum conservation equation for the electromagnetic subsystem can be written in the form of (3.2b) with the quantities given by [53]

$$\bar{\bar{T}}_{eh} = \frac{1}{2}(\epsilon_0 \bar{\mathcal{E}} \cdot \bar{\mathcal{E}} + \mu_0 \bar{\mathcal{H}} \cdot \bar{\mathcal{H}})\bar{\bar{I}} - \epsilon_0 \bar{\mathcal{E}}\bar{\mathcal{E}} - \mu_0 \bar{\mathcal{H}}\bar{\mathcal{H}} \tag{3.5a}$$

$$\bar{G}_{eh} = \epsilon_0 \mu_0 \bar{\mathcal{E}} \times \bar{\mathcal{H}} \tag{3.5b}$$

$$\bar{f}_{eh} = \rho_e \bar{\mathcal{E}} + \rho_h \bar{\mathcal{H}} + \bar{\mathcal{J}}_e \times \mu_0 \bar{\mathcal{H}} - \bar{\mathcal{J}}_h \times \epsilon_0 \bar{\mathcal{E}}, \tag{3.5c}$$

where $\bar{\bar{I}}$ is the 3×3 identity dyad and $\bar{\mathcal{E}}\bar{\mathcal{E}}$ represents a dyadic product. The quantities in (3.4) and (3.5) represent the electromagnetic subsystem and may be regarded as the electromagnetic contributions to energy and momentum [53]. The quantities W_{eh} and $\bar{S}_{eh}$ are identified as the energy density of the electromagnetic fields and the Poynting power, respectively. The momentum density $\bar{G}_{eh}$ is often referred to as the Abraham momentum [36], and the momentum flux $\bar{\bar{T}}_{eh}$ takes the form of the free-space Maxwell stress tensor [54, 55]. It is well know that a material contribution to the energy density accompanies the propagation of electromagnetic energy in dielectrics [85–87]. In the section that follows, we derive the corresponding material contribution to the wave momentum.

3.2.2 Energy and momentum contribution from dispersive media

To model many experimental observations, it is necessary to include the dispersive characteristics of the material in describing the observed behavior of the electromagnetic wave. The inclusion of losses requires that a specific model for $\bar{\mathcal{P}}$ and $\bar{\mathcal{M}}$ be applied. The material response to the electromagnetic fields is described by the

differential equations for a Lorentz medium

$$\left(\frac{\partial^2}{\partial t^2}+\gamma_e\frac{\partial}{\partial t}+\omega_{e0}^2\right)\bar{\mathcal{P}}=\epsilon_0\omega_{ep}^2\bar{\mathcal{E}} \tag{3.6a}$$

$$\left(\frac{\partial^2}{\partial t^2}+\gamma_m\frac{\partial}{\partial t}+\omega_{m0}^2\right)\bar{\mathcal{M}}=F\omega_{mp}^2\bar{\mathcal{H}}, \tag{3.6b}$$

where the parameters of the equations have their usual meanings [84]. To derive the energy of the electromagnetic wave, the material equations (3.6a) and (3.6b) are dot multiplied by $\bar{\mathcal{J}}_e$ and $\bar{\mathcal{J}}_h$, respectively. The resulting equations

$$\bar{\mathcal{J}}_e\cdot\bar{E}=\frac{1}{2\epsilon_0\omega_{ep}^2}\frac{\partial}{\partial t}\left\{\frac{\partial\bar{\mathcal{P}}}{\partial t}\cdot\frac{\partial\bar{\mathcal{P}}}{\partial t}+\omega_{e0}^2\bar{\mathcal{P}}\cdot\bar{\mathcal{P}}\right\}+\frac{\gamma_e}{\epsilon_0\omega_{ep}^2}\frac{\partial\bar{\mathcal{P}}}{\partial t}\cdot\frac{\partial\bar{\mathcal{P}}}{\partial t} \tag{3.7a}$$

$$\bar{\mathcal{J}}_h\cdot\bar{\mathcal{H}}=\frac{\mu_0}{2F\omega_{mp}^2}\frac{\partial}{\partial t}\left\{\frac{\partial\bar{\mathcal{M}}}{\partial t}\cdot\frac{\partial\bar{\mathcal{M}}}{\partial t}+\omega_{m0}^2\bar{\mathcal{M}}\cdot\bar{\mathcal{M}}\right\}+\frac{\gamma_m\mu_0}{F\omega_{mp}^2}\frac{\partial\bar{\mathcal{M}}}{\partial t}\cdot\frac{\partial\bar{\mathcal{M}}}{\partial t} \tag{3.7b}$$

are then added to the energy conservation equation of the electromagnetic subsystem given by (3.2a) with the quantities defined by (3.4). The resulting energy conservation equation for the electromagnetic wave is in the form of (3.2a) with the energy flow $\bar{S}$, energy density W, and energy dissipation φ given by [84]

$$\bar{S}=\bar{S}_{eh}=\bar{\mathcal{E}}\times\bar{\mathcal{H}} \tag{3.8a}$$

$$\begin{aligned}W=&\frac{\epsilon_0}{2}\bar{\mathcal{E}}\cdot\bar{\mathcal{E}}+\frac{\mu_0}{2}\bar{\mathcal{H}}\cdot\bar{\mathcal{H}}+\frac{1}{2\epsilon_0\omega_{ep}^2}\left[\frac{\partial\bar{\mathcal{P}}}{\partial t}\cdot\frac{\partial\bar{\mathcal{P}}}{\partial t}+\omega_{e0}^2\bar{\mathcal{P}}\cdot\bar{\mathcal{P}}\right]\\&+\frac{\mu_0}{2F\omega_{mp}^2}\left[\frac{\partial\bar{M}}{\partial t}\cdot\frac{\partial\bar{\mathcal{M}}}{\partial t}+\omega_{m0}^2\bar{\mathcal{M}}\cdot\bar{\mathcal{M}}\right]\end{aligned} \tag{3.8b}$$

$$\varphi=\frac{\gamma_e}{\epsilon_0\omega_{ep}^2}\frac{\partial\bar{\mathcal{P}}}{\partial t}\cdot\frac{\partial\bar{\mathcal{P}}}{\partial t}+\frac{\gamma_m\mu_0}{F\omega_{mp}^2}\frac{\partial\bar{\mathcal{M}}}{\partial t}\cdot\frac{\partial\bar{\mathcal{M}}}{\partial t}. \tag{3.8c}$$

A few remarks are in order regarding the quantities in (3.8), which are written without subscript to indicate values corresponding to the electromagnetic wave. First, the energy flow $\bar{S}$ is generally regarded as the Poynting power and retains its free-space form even in the presence of a lossy, dispersive material. Second, the energy density W contains contributions from the potential energy and kinetic energy of the electric and

magnetic dipoles. Furthermore, the form of (3.8b) has been regarded as significant since the energy density remains positive in left-handed media [84]. Third, the energy dissipation term φ depends upon the damping factors γ_e and γ_m in (3.6). Thus, $\varphi = 0$ in the limiting case of a lossless material (*i.e.* the energy of the electromagnetic wave is conserved).

A similar mathematical derivation exists for the wave momentum. To determine the contribution of the material response fields to the wave momentum, the material dispersion equations (3.6) are dot multiplied by the dyads $-\nabla\bar{\mathcal{P}}$ and $-\mu_0\nabla\bar{\mathcal{M}}$, respectively. The resulting vector equations are then added to the electromagnetic conservation equation given by (3.2b) and (3.5) to yield

$$\begin{aligned}\nabla\cdot\bar{\bar{T}}_{eh} + \frac{\partial\bar{G}_{eh}}{\partial t} + \bar{f}_{eh} + \bar{\mathcal{E}}\cdot\nabla\bar{\mathcal{P}} + \mu_0\bar{\mathcal{H}}\cdot\bar{\mathcal{M}} \\ - \nabla\bar{\mathcal{P}}\cdot\left(\frac{\partial^2\bar{\mathcal{P}}}{\partial t^2} + \omega_{e0}^2\bar{\mathcal{P}}\right)\frac{1}{\epsilon_0\omega_{ep}^2} - \mu_0\nabla\bar{\mathcal{M}}\cdot\left(\frac{\partial^2\bar{\mathcal{M}}}{\partial t^2} + \omega_{m0}^2\bar{\mathcal{M}}\right)\frac{\mu_0}{F\omega_{mp}^2} \\ = \nabla\bar{\mathcal{P}}\cdot\frac{\partial\bar{\mathcal{P}}}{\partial t}\frac{\gamma_e}{\epsilon_0\omega_{ep}^2} + \nabla\bar{\mathcal{M}}\cdot\frac{\partial\bar{\mathcal{M}}}{\partial t}\frac{\gamma_m\mu_0}{F\omega_{mp}^2}.\end{aligned} \tag{3.9}$$

Application of identities from vector calculus allows us to write

$$\begin{aligned}-\nabla\bar{\mathcal{P}}\cdot\left(\frac{\partial^2\bar{\mathcal{P}}}{\partial t^2} + \omega_{e0}^2\bar{\mathcal{P}}\right)\frac{1}{\epsilon_0\omega_{ep}^2} &= \nabla\cdot\left[\frac{1}{2\epsilon_0\omega_{ep}^2}\left(\frac{\partial\bar{\mathcal{P}}}{\partial t}\cdot\frac{\partial\bar{\mathcal{P}}}{\partial t} - \omega_{e0}^2\bar{\mathcal{P}}\cdot\bar{\mathcal{P}}\right)\right] \\ &\quad - \frac{\partial}{\partial t}\left[\frac{1}{\epsilon_0\omega_{ep}^2}\left(\nabla\bar{\mathcal{P}}\cdot\frac{\partial\bar{\mathcal{P}}}{\partial t}\right)\right] \qquad (3.10a) \\ -\nabla\bar{\mathcal{M}}\cdot\left(\frac{\partial^2\bar{\mathcal{M}}}{\partial t^2} + \omega_{m0}^2\bar{\mathcal{M}}\right)\frac{\mu_0}{F\omega_{mp}^2} &= \nabla\cdot\left[\frac{\mu_0}{2F\omega_{mp}^2}\left(\frac{\partial\bar{\mathcal{M}}}{\partial t}\cdot\frac{\partial\bar{\mathcal{M}}}{\partial t} - \omega_{m0}^2\bar{\mathcal{M}}\cdot\bar{\mathcal{M}}\right)\right] \\ &\quad - \frac{\partial}{\partial t}\left[\frac{\mu_0}{F\omega_{mp}^2}\left(\nabla\bar{\mathcal{M}}\cdot\frac{\partial\bar{\mathcal{M}}}{\partial t}\right)\right] \qquad (3.10b) \\ \bar{f}_{eh} + \bar{\mathcal{E}}\cdot\nabla\bar{\mathcal{P}} + \mu_0\bar{\mathcal{H}}\cdot\bar{\mathcal{M}} &= \nabla\cdot\left[\left(\bar{\mathcal{P}}\cdot\bar{\mathcal{E}} + \mu_0\bar{\mathcal{M}}\cdot\bar{\mathcal{H}}\right)\bar{\bar{I}} - \bar{\mathcal{P}}\bar{\mathcal{E}} - \mu_0\bar{\mathcal{M}}\bar{\mathcal{H}}\right] \\ &\quad + \frac{\partial}{\partial t}\left[\bar{\mathcal{D}}\times\bar{\mathcal{B}} - \epsilon_0\mu_0\bar{\mathcal{E}}\times\bar{\mathcal{H}}\right]. \qquad (3.10c)\end{aligned}$$

By combining (3.9) and (3.10), the momentum conservation equation for the elec-

tromagnetic wave can be written in the form of (3.2b) with the momentum flow, momentum density, and force density

$$\bar{\bar{T}} = \frac{1}{2}(\bar{\mathcal{D}}\cdot\bar{\mathcal{E}}+\bar{\mathcal{B}}\cdot\bar{\mathcal{H}})\bar{\bar{I}} - \bar{\mathcal{D}}\bar{\mathcal{E}} - \bar{\mathcal{B}}\bar{\mathcal{H}} + \frac{1}{2}\left[\frac{1}{\epsilon_0\omega_{ep}^2}\left(\frac{\partial\bar{\mathcal{P}}}{\partial t}\cdot\frac{\partial\bar{\mathcal{P}}}{\partial t} - \omega_{e0}^2\bar{\mathcal{P}}\cdot\bar{\mathcal{P}}\right)\right.$$
$$\left. + \frac{\mu_0}{F\omega_{mp}^2}\left(\frac{\partial\bar{\mathcal{M}}}{\partial t}\cdot\frac{\partial\bar{\mathcal{M}}}{\partial t} - \omega_{m0}^2\bar{\mathcal{M}}\cdot\bar{\mathcal{M}}\right) + (\bar{\mathcal{P}}\cdot\bar{\mathcal{E}}+\mu_0\bar{\mathcal{M}}\cdot\bar{\mathcal{H}})\right]\bar{\bar{I}} \tag{3.11a}$$

$$\bar{G} = \bar{\mathcal{D}}\times\bar{\mathcal{B}} - \frac{1}{\epsilon_0\omega_{ep}^2}\nabla\bar{\mathcal{P}}\cdot\frac{\partial\bar{\mathcal{P}}}{\partial t} - \frac{\mu_0}{F\omega_{mp}^2}\nabla\bar{\mathcal{M}}\cdot\frac{\partial\bar{\mathcal{M}}}{\partial t} \tag{3.11b}$$

$$\bar{f} = -\frac{\gamma_e}{\epsilon_0\omega_{ep}^2}\nabla\bar{\mathcal{P}}\cdot\frac{\partial\bar{\mathcal{P}}}{\partial t} - \frac{\gamma_m\mu_0}{F\omega_{mp}^2}\nabla\bar{\mathcal{M}}\cdot\frac{\partial\bar{\mathcal{M}}}{\partial t}. \tag{3.11c}$$

The expressions in (3.11) define the quantities for the wave momentum conservation equation analogous to the wave energy quantities given by (3.8). The momentum density $\bar{G}$ contains the Minkowski [35] momentum $\bar{\mathcal{D}}\times\bar{\mathcal{B}}$ plus material dispersion terms. Likewise, the momentum flow $\bar{\bar{T}}$ is the Maxwell stress tensor $\frac{1}{2}(\bar{\mathcal{D}}\cdot\bar{\mathcal{E}}+\bar{\mathcal{B}}\cdot\bar{\mathcal{H}})\bar{\bar{I}} - \bar{\mathcal{D}}\bar{\mathcal{E}} - \bar{\mathcal{B}}\bar{\mathcal{H}}$ in non-dispersive media [39, 54] plus dispersive terms. We note that the momentum dissipation term $\bar{f}$ depends upon the damping factors γ_e and γ_m in (3.6). Thus, $\bar{f}=0$ in the limiting case of a lossless, unbounded material (*i.e.* the momentum of the electromagnetic wave is conserved).

3.2.3 Energy and momentum of a monochromatic wave

For the remainder of this chapter, we consider the propagation of time-harmonic electromagnetic waves and employ complex notation such that the complex field $\bar{E}$ is related to the time-domain field by $\bar{\mathcal{E}} = \Re\{\bar{E}e^{-i\omega t}\}$. To arrive at various quantities of interest, the substitutions $\partial/\partial t \to -i\omega$ and $\nabla \to i\bar{k}$ are made, which are valid for plane wave solutions to the wave equation [39]. The constitutive parameters,

$$\epsilon(\omega) = \epsilon_0\left(1 - \frac{\omega_{ep}^2}{\omega^2 - \omega_{e0}^2 + i\omega\gamma_e}\right) \tag{3.12a}$$

$$\mu(\omega) = \mu_0\left(1 - \frac{F\omega_{mp}^2}{\omega^2 - \omega_{m0}^2 + i\omega\gamma_m}\right), \tag{3.12b}$$

are functions of the frequency ω and consist of real and imaginary parts denoted by $\epsilon = \epsilon_R + i\epsilon_I$ and $\mu = \mu_R + i\mu_I$. Likewise, the time-average of the squared polarization and magnetization are

$$|\bar{P}|^2 = \frac{\epsilon_0^2 \omega_{ep}^4}{\left(\omega^2 - \omega_{e0}^2\right)^2 + \gamma_e^2 \omega^2} |\bar{E}|^2 \tag{3.13a}$$

$$|\bar{M}|^2 = \frac{F^2 \omega_{mp}^4}{\left(\omega^2 - \omega_{m0}^2\right)^2 + \gamma_m^2 \omega^2} |\bar{H}|^2. \tag{3.13b}$$

Similarly, $|\partial \bar{P}/\partial t|^2 = \omega^2 |\bar{P}|^2$ and $|\partial \bar{M}/\partial t|^2 = \omega^2 |\bar{M}|^2$. These quantities can now be applied to determine the time-average values relating to energy and momentum conservation given in the previous section.

The time average energy density found from (3.8b) is

$$\begin{aligned} < W > = & \frac{\epsilon_0}{2} \left[1 + \frac{\omega_{ep}^2 \left(\omega^2 + \omega_{e0}^2\right)}{\left(\omega^2 - \omega_{e0}^2\right)^2 + \gamma_e^2 \omega^2} \right] |\bar{E}|^2 \\ & + \frac{\mu_0}{2} \left[1 + \frac{F \omega_{mp}^2 \left(\omega^2 + \omega_{m0}^2\right)}{\left(\omega^2 - \omega_{m0}^2\right)^2 + \gamma_m^2 \omega^2} \right] |\bar{H}|^2 . \end{aligned} \tag{3.14}$$

We note that in the lossless case, $\gamma_e = 0$ and $\gamma_m = 0$ implies that both $\epsilon_I = 0$ and $\mu_I = 0$, and the energy density satisfies the well-known relation [39, 54, 85, 86]

$$< W >= \frac{1}{4} \frac{\partial(\epsilon\omega)}{\partial\omega} |\bar{E}|^2 + \frac{1}{4} \frac{\partial(\mu\omega)}{\partial\omega} |\bar{H}|^2 . \tag{3.15}$$

The extension of (3.15) to lossy materials has been criticized due to the possibility of negative values for LHM [84]. In contrast, the average energy density in (3.14) remains positive for all ω. However, it is the rate of change in energy that appears in the conservation equation (3.2a), which tends to zero upon cycle averaging. That is, $< \partial W/\partial t >= 0$, and the resulting conservation equation

$$- < \nabla \cdot \bar{S} >= \frac{1}{2} \left[\omega \epsilon_I |\bar{E}|^2 + \omega \mu_I |\bar{H}|^2 \right] \tag{3.16}$$

is generally regarded as the complex Poynting's theorem, where $< \bar{S} >= \frac{1}{2}\Re\{\bar{E} \times \bar{H}^*\}$ is the time average Poynting power [39].

A similar analysis is applied to the wave momentum conservation equation. The average momentum density,

$$\langle \bar{G} \rangle = \frac{1}{2}\Re\Bigg\{ \bar{D} \times \bar{B}^* + \bar{k}\frac{\epsilon_0 \omega \omega_{ep}^2}{(\omega^2 - \omega_{e0}^2)^2 + \gamma_e^2 \omega^2}|\bar{E}|^2 + \bar{k}\frac{\mu_0 \omega F \omega_{mp}^2}{(\omega^2 - \omega_{m0}^2)^2 + \gamma_m^2 \omega^2}|\bar{H}|^2 \Bigg\}, \tag{3.17}$$

is obtained from (3.11b). It is simple to show using (3.12) that the average momentum given in (3.17) satisfies (3.1) when the medium is lossless. Thus, the expression for the momentum given by Vesselago is valid only when absorption of electromagnetic energy can be ignored. The momentum flow reduces to

$$< \bar{\bar{T}} >= \frac{1}{2}\Re\Bigg\{ \frac{1}{2}(\bar{D} \cdot \bar{E}^* + \bar{B} \cdot \bar{H}^*)\bar{\bar{I}} - \bar{D}\bar{E}^* - \bar{B}\bar{H}^* \Bigg\} \tag{3.18}$$

since the dispersive terms in (3.11a) tend to zero upon cycle averaging. The momentum flow in (3.18) is also referred to as the Maxwell stress tensor in matter [39, 54]. Since the average rate of change in momentum density is zero (*i.e.* $< \partial \bar{G}/\partial t >= 0$), the momentum conservation theorem for a monochromatic wave reduces to

$$- < \nabla \cdot \bar{\bar{T}} >= \frac{1}{2}\Re\Bigg\{ \omega \epsilon_I \bar{E} \times \bar{B}^* - \omega \mu_I \bar{H} \times \bar{D}^* \Bigg\}. \tag{3.19}$$

The right-hand side of (3.19) is recognized as the force density on free currents.

It is now possible to study the propagation of electromagnetic energy and momentum in a dispersive LHM. Consider an electromagnetic wave $\bar{E} = \hat{x}E_x = \hat{x}e^{ikz}$ propagating in an unbounded medium with complex index of refraction $n + i\kappa = kc/\omega = c\sqrt{\epsilon\mu}$, where c is the speed of light in vacuum. The magnetic field satisfies the relation $\sqrt{\mu}H_y = \sqrt{\epsilon}E_x$. The analysis is simplified by taking the ratio of the energy flow and energy density. This ratio $< S_z > / < W > \equiv v_e$ is generally

referred to as the energy velocity of the wave [85, 87]. The $\hat{z}$-directed time-average Poynting power is simply $< S_z >= \frac{1}{2}\Re\{E_x H_y^*\}$. Similarly, a momentum velocity $< T_{zz} > / < G_z > \equiv v_m$ may also be defined [65]. The average momentum flux is

$$< T_{zz} >= \frac{1}{4}\Re\{\epsilon|E_x|^2 + \mu|H_y|^2\} = \frac{n}{c} < S_z > . \tag{3.20}$$

It is obvious from (3.20) that the momentum flow is antiparallel to the energy flow when the index of refraction is negative. Furthermore, it has been previously argued that the momentum density $< G_z >$ is also antiparallel to $< S_z >$ when both $n < 0$ and when absorption is negligible [82]. As an illustration, the energy velocity and momentum velocity have been plotted along with the index of refraction for a lossless medium in Fig. 3-1. Since there is no loss, v_e and v_m are both equivalent to the group velocity [39]. In the negative index region, both $< W >$ and $< S_z >$ are positive while $< G_z >$ and $< T_{zz} >$ are negative. This latter point is evident by the fact that $v_m > 0$, which implies that $< G_z >$ and $< T_{zz} >$ have the same sign for all ω. A lossy medium is considered for a second illustration as shown in Fig. 3-2. In this example, the energy velocity and momentum velocity are quite different in the region where $n < 0$. The energy velocity remains positive since both $< W >$ and $< S_z >$ are positive. However, the momentum velocity becomes negative for part of this region. While the sign of $< T_{zz} >$ follows exactly the sign of n via (3.20), the momentum density $< G_z >$ may be positive or negative in a frequency band with negative index of refraction.

The results of this section prove that the momentum density $< \bar{G} >$ may be parallel or antiparallel to the power flow $< \bar{S} >$ in a lossy LHM. This is in contrast to the results for a lossless LHM, where the momentum density is always antiparallel to the energy flow [82]. However, the momentum transfer from a monochromatic wave is independent of the momentum density. Instead, the momentum conservation equation reduces to (3.19). Thus, it is expected that observed forces due a continuous

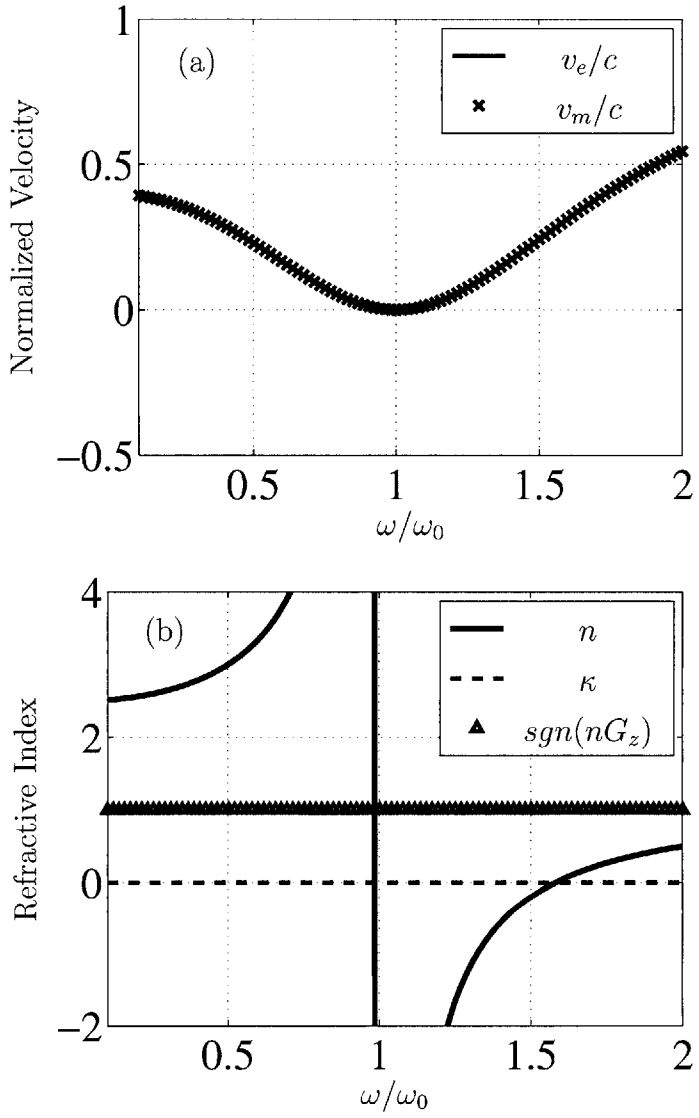

Figure 3-1: (a) Normalized energy velocity and momentum velocity for an electromagnetic wave in a lossless medium. (b) The complex index of refraction is given by $n + i\kappa = c\sqrt{\mu\epsilon}$, where μ and ϵ are given in (3.12). The triangles clearly show that n and G_z have the same signs over the entire frequency range. The parameters of the material are $\omega_{e0} = \omega_{m0} \equiv \omega_0$, $\omega_{ep}^2 = F\omega_{mp}^2 = 1.5\omega_0^2$, and $\gamma_e = \gamma_m = 0$. © 2007 The American Physical Society [2].

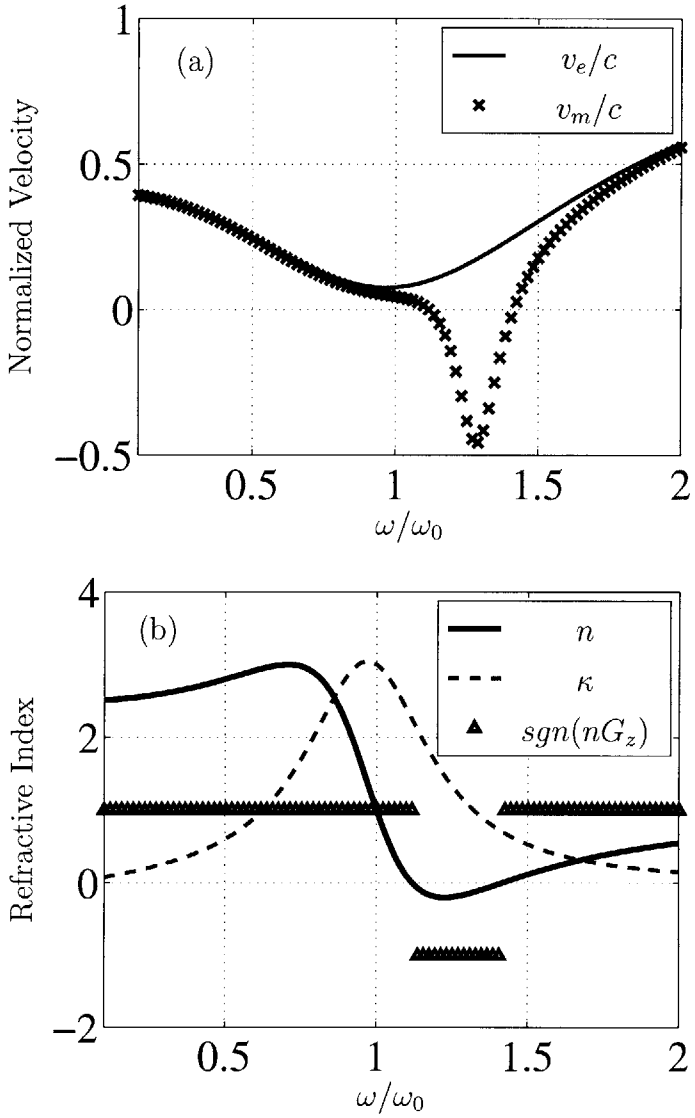

Figure 3-2: (a) Normalized energy velocity and momentum velocity for an electromagnetic wave in a lossy medium. (b) The complex index of refraction is given by $n + i\kappa = c\sqrt{\mu\epsilon}$, where μ and ϵ are given in (3.12). The triangles clearly show the frequency range where n and G_z have different signs (*i.e.* $sgn(nG_z) = -1$). The parameters of the material are $\omega_{e0} = \omega_{m0} \equiv \omega_0$, $\omega_{ep}^2 = F\omega_{mp}^2 = 1.5\omega_0^2$, and $\gamma_e = \gamma_m = 0.5\omega_0$. © 2007 The American Physical Society [2].

wave depend upon the average momentum flow, which, due to the direct dependence upon n shown in (3.20), is opposite to the flow of energy in an LHM. In the following section, this conservation equation for a monochromatic wave will be applied to predict the reversal of radiation pressure in LHM.

3.3 Electromagnetic Force

The average force exerted by a monochromatic wave upon matter is given by the Lorentz force density applied directly to matter

$$< \bar{f} >= \frac{1}{2}\Re\Big\{\epsilon_0(\nabla\cdot\bar{E})\bar{E}^* + \mu_0(\nabla\cdot\bar{H})\bar{H}^* - i\omega\bar{P}\times\mu_0\bar{H}^* + i\omega\mu_0\bar{M}\times\epsilon_0\bar{E}^*\Big\} \quad (3.21)$$

is the time average of (3.5c). Furthermore, the Lorentz force density can be decomposed into the force on free currents and the force on bound currents and charges. The total force density $< \bar{f} >=< \bar{f}_b > + < \bar{f}_c >$ is separated based on the real and imaginary contributions to the complex permittivity $\epsilon = \epsilon_R + i\epsilon_I$ and $\mu = \mu_R + i\mu_I$. According to (3.19), the force density

$$< \bar{f}_c >= \frac{1}{2}\Re\Big\{\omega\epsilon_I\bar{E}\times\bar{B}^* - \omega\mu_I\bar{H}\times\bar{D}^*\Big\}, \quad (3.22)$$

relates the force density on free currents to the momentum transfer as the wave attenuates in the medium, and the force density on bound charges and currents

$$\begin{aligned} < \bar{f}_b > = \frac{1}{2}\Re\Big\{&\epsilon_0(\nabla\cdot\bar{E})\bar{E}^* + \mu_0(\nabla\cdot\bar{H})\bar{H}^* \\ &- i\omega(\epsilon_R-\epsilon_0)\bar{E}\times\bar{B}^* + i\omega(\mu_R-\mu_0)\bar{H}\times\bar{D}^*\Big\} \end{aligned} \quad (3.23)$$

gives the remaining momentum transfer to the host material. Therefore, the theory presented in the previous chapter may be applied to a dispersive medium, and the total forces $< \bar{F} >$, $< \bar{F}_c >$, and $< \bar{F}_b >$ resulting from the total volume integration

of the corresponding force densities can be found equivalently, after application of the divergence theorem, by appropriate integration of the Maxwell stress tensor. In what follows, we apply the force on free currents and the force on bound currents and charges to determine the electromagnetic momentum transfer to LHM.

3.3.1 Radiation pressure on an LHM interface

The radiation pressure on an LHM interface was previously calculated by applying momentum conservation at the boundary separating free space and the material [83]. However, the momentum transmitted into the LHM was assumed to be parallel to the Poynting power. In contrast, we derive the radiation pressure on the interface by applying the Lorentz force directly. That is, the force density (3.22) is applied to derive the electromagnetic wave momentum transmitted into a medium occupying the region $z > 0$. The TE and TM polarized waves are treated identically by considering the fields $\bar{E} = \hat{e}E_0 e^{i\bar{k}\cdot\bar{r}}$ and $\bar{H} = \hat{h}H_0 e^{i\bar{k}\cdot\bar{r}}$ transmitted into the medium, where E_0 and H_0 are the magnitudes of the electric field and magnetic field at $z = 0^+$, $\bar{k} = k\hat{s}$ is the complex wave vector, and $\hat{s} = \hat{e} \times \hat{h}$. The fields satisfy the relations $\omega\mu\bar{H} = \bar{k} \times \bar{E}$ and $\omega\epsilon\bar{E} = -\bar{k} \times \bar{H}$, and the field solutions are omitted since the details of the reflection/transmission (R/T) of an electromagnetic wave incident onto an LHM interface have been extensively treated by analytical methods [75, 88–90]. Since $\epsilon = |\epsilon| \exp(i\phi_\epsilon)$ and $\mu = |\mu| \exp(i\phi_\mu)$ are complex, the phase propagation direction is determined by the sign of k_R, which is defined by $k = k_R + ik_I = \omega\sqrt{|\epsilon||\mu|}\exp[i(\phi_\epsilon + \phi_\mu)/2]$. Inserting the fields into (3.22) and using the relationship $\hat{s} = \bar{k}/k = (\bar{k}/k)^*$ yields

$$< \bar{f}_c >= \frac{1}{2}\Re\left\{ \bar{k}^* \left[\epsilon_I |\bar{E}|^2 + \mu_I |\bar{H}|^2\right] \right\}. \tag{3.24}$$

By applying Poynting's theorem (3.16), the force density on free currents (3.24) is written as

$$< \bar{f}_c >= -\frac{1}{2}\frac{\bar{k}_R}{\omega}\Re\left\{\nabla \cdot \bar{S}\right\} \equiv -\hat{s}\frac{1}{2}\Re\left\{\nabla \cdot \bar{p}\right\}, \tag{3.25}$$

where $\bar{S} = \bar{E} \times \bar{H}^*$ is the complex Poynting power and $\bar{p} \equiv n\bar{S}/c$ is the momentum flux density of the wave. Thus, the direction of the force on free currents depends upon the sign of the index of refraction $n = ck_R/\omega$.

Transmission of the momentum flux density $\bar{p}$ ensures that the tangential force due to R/T at the boundary is zero. To demonstrate this fact, we treat a TE polarized wave $\bar{E} = \hat{y}E_0 e^{-k_{zI}z} e^{ik_{zR}z} e^{ik_x x}$ transmitted into the material and integrate the force density on free currents over the region $z \in [0, \infty)$. The analysis is simplified by applying the divergence theorem to (3.25). Thus the total pressure on free currents is $\bar{p}$ evaluated at $z = 0^+$, where it is assumed that the fields attenuate to zero as $z \to \infty$ due to losses. The tangential component of the resulting force is

$$\hat{x} \cdot < \bar{F}_c >= \frac{\epsilon_0}{2} |E_i|^2 (1 - |R_{hs}|^2) \cos\theta_i \sin\theta_i, \tag{3.26}$$

where $|E_i|^2$ is the intensity of the incident wave and θ_i is the incident angle. In deriving (3.26), we have applied $E_0 = E_i T_{hs}$ and the fundamental relationship between the half-space reflection coefficient R_{hs} and transmission coefficient T_{hs} resulting from the boundary conditions [39]. The fact that (3.26) gives the total tangential momentum transfer to the half-space leads to the conclusion that the tangential component of $< \bar{F}_b >$ is identically zero. In fact, it is straightforward to verify that this is true by integrating (3.23) over $z \in [0, \infty)$. Thus, the force on a half space void of free currents is normal to the surface. Just as $< \bar{F}_c >$ gives the momentum transfer to free carriers inside the medium, $< \bar{F}_b >$ can be interpreted as the momentum transfer due to R/T at the boundary since it can be computed by the application of the Maxwell stress tensor along a surface that just encloses the boundary. This view of momentum conservation is shown in Fig. 3-3 for the case of $\epsilon = -\epsilon_0$ and $\mu = -\mu_0$ previously considered [83]. The momentum flux is seen to be in the opposite direction of the Poynting power and the tangential projection of the wave momentum is conserved at the interface with an LHM resulting in zero tangential force.

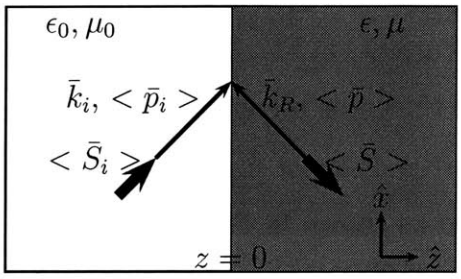

Figure 3-3: Average power and momentum flux of a monochromatic wave refracted at the boundary of free space (μ_0, ϵ_0) and a matched LHM $(\mu = -\mu_0, \epsilon = -\epsilon_0)$ occupying the region $z > 0$. The incident power $< \bar{S}_i >$ and incident momentum flux $< \bar{p}_i >$ are parallel, while the transmitted power $< \bar{S} >$ and transmitted momentum flux $< \bar{p} >$ are antiparallel. © 2007 The American Physical Society [2].

3.3.2 Radiation pressure on an LHM slab

A more physically realistic situation of an electromagnetic wave incident from free space onto an absorbing slab is now considered. The expression for the radiation pressure

$$< \bar{F} >= \frac{\epsilon_0}{2}|E_i|^2 \left[1 + |R_{slab}|^2 - |T_{slab}|^2\right], \tag{3.27}$$

due to a plane wave of intensity $|E_i|^2$ incident normal to the surface of a slab occupying the region $0 < z < d$ satisfies the conservation of free space electromagnetic momentum. The reflection coefficient R_{slab} and transmission coefficient T_{slab} have well-known closed form solutions [39]. Also, the total force can be decomposed into the force on bound currents and the force on free currents.

Figure 3-4 (a) gives an example of momentum transfer to an absorbing dielectric. In most situations, the observed force is expected to be the total force $< F >$, which is always positive. However, several experiments have been devised to confirm the dependence of $< F_c >$ upon n. Indeed, the photon drag effect [51, 60], photon recoil in a dilute gas of atoms [52], and the deflection of mirrors immersed in dielectric fluids [49, 50] provide experimental evidence that the wave momentum is directly

proportional to the index of refraction in dielectrics. This direct dependence upon n explains the force on free currents in Fig. 3-4 (a), which is greater than the total force on the slab when the slab thickness is comparable to or greater than the penetration depth of the wave. By virtue of linear momentum conservation, a negative force on bound currents is required as shown in Fig. 3-4 (a). This recoil force is unobserved in most experiments. However, we believe that one of the earliest observations of this force was made by J.H. Poynting and G. Barlow. In an experiment to measure the recoil of light against its source, Poynting and Barlow measured the deflection of disks under steady illumination [48]. One of these experiments involving light incident upon the absorbing side of a disk produced an initial suction. It was explained that the effect was due to heating of occluded gas from the silver film on the unilluminated side of the disk causing a back pressure on the film. From the theory presented here, the heated gas obtained a momentum greater than the incident radiation pressure due to the absorption of electromagnetic energy in the disk. However, Poynting and Barlow observed the recoil force directly, which we explain as the force on bound currents $< F_b >$.

A similar situation may be envisioned for an LHM slab as shown in Fig. 3-4 (b). As with the dielectric slab in Fig. 3-4 (a), the total pressure is always positive. However, the momentum transfer to free currents in LHM is negative since $< \bar{f}_c >$ is proportional to n. Therefore, as the wave attenuates in an LHM, the free currents are pulled toward the incident wave, thus proving that radiation pressure in LHM is negative. As required by momentum conservation, the force on bound currents is positive. Thus, while the total force remains positive, the force on free currents is negative, and the force on bound currents is positive for an absorbing LHM slab, which is in contrast to the situation for an RHM slab.

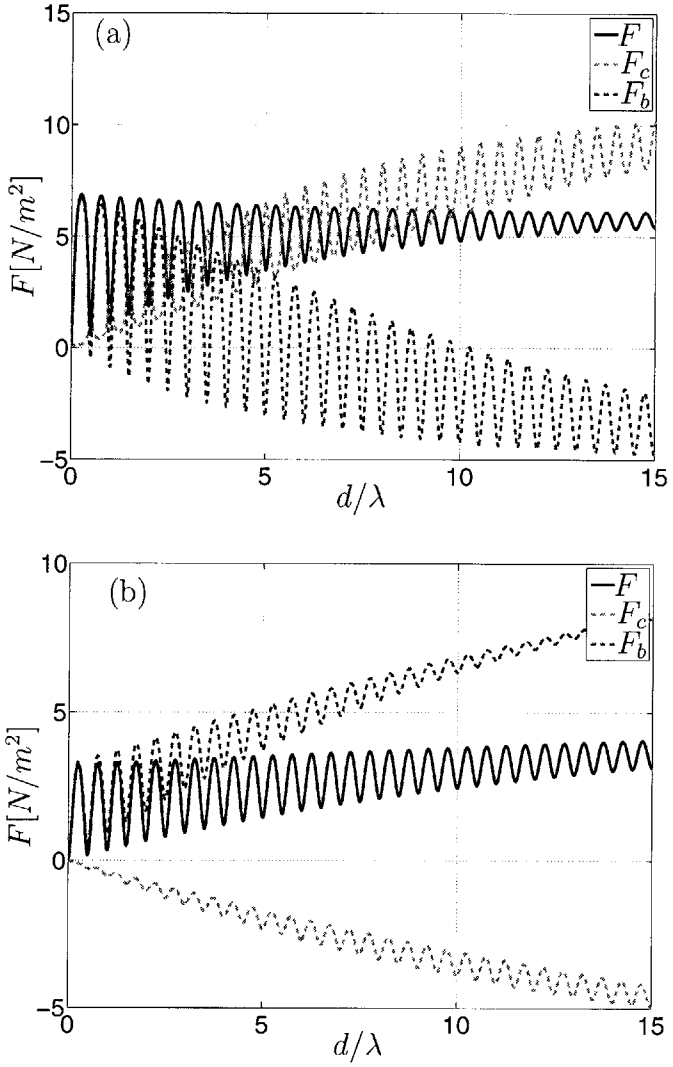

Figure 3-4: Radiation pressure due to a unit amplitude electromagnetic wave incident normally upon an absorbing slab as a function of thickness d. The radiation pressure is decomposed into the force on free currents and the force on bound currents for (a) dielectric slab ($\mu = \mu_0$) with index of refraction $n + i\kappa = 4 + i0.04$ and (b) LHM with $\mu = (-1 + 0.01)\mu_0$ and $\epsilon = (-4 + i0.04)\epsilon_0$. The thickness is normalized to the wavelength inside the material. © 2007 The American Physical Society [2].

3.4 Discussion

The momentum transfer to isotropic LHM has been rigourously treated by applying the classical electromagnetic wave theory. Contrary to previous attempts to describe the momentum of the electromagnetic wave in LHM, material dispersion and losses have been included, which are necessary for a causal medium with negative index of refraction. In this regard, the standard Lorentz model was employed for the polarization and magnetization, which is consistent with a previous derivation of the electromagnetic wave energy [84]. Thus, the derived expressions for the momentum given by (3.11) is analogous to the energy of the wave in (3.8). It is recognize that the results in (3.8) and (3.11) are open to some interpretation. It is known that while the mathematical validity of Poynting's theorem is unquestionable, its interpretation is subject to some criticism [55]. For example, it is certainly possible in many cases to algebraically rearrange terms in (3.8) so that the energy flow and energy density take different forms, while the prediction of measurable quantities such as time-average Poynting power and energy dissipation remain unaltered. Likewise, one may assume that the momentum conservation theorem given by (3.11) may also be subject to similar manipulations. However, the measurable results predicted by the application of the cycle-average theorems (3.16) and (3.19) are unambiguous. Also, the results presented here depend upon the model used for the material response in the presence of the electromagnetic fields. For example, the two time derivative Lorentz material model

$$\left(\frac{\partial^2}{\partial t^2}+\gamma_m\frac{\partial}{\partial t}+\omega_{m0}^2\right)\bar{\mathcal{M}}=\left(\omega_{mp}^2\chi_\alpha^m+\omega_{mp}\chi_\beta^m\frac{\partial}{\partial t}+\chi_\gamma^m\frac{\partial^2}{\partial t^2}\right)\bar{\mathcal{H}} \tag{3.28}$$

was previously employed to describe the magnetic response of an LHM [69]. This model reduces to the standard Lorentz model for $\xi_\beta^m=\xi_\gamma^m=0$. Another variation in which $\xi_\alpha^m=\xi_\beta^m=0$ was recently applied to derive an alternate form of the electromagnetic energy density in LHM, and it was acknowledged that this alternate form

maps very closely to the result derived from the standard Lorentz media model [91]. In this regard, the various models produce equations for the electromagnetic wave energy that differ in form, but give similar quantitative results in the negative index frequency ranges where the models have overlapping validity. Thus, it is expected that the results for momentum, like the energy, should remain both qualitatively and quantitatively similar in frequency bands where multiple models are valid. Furthermore, it is noted that the results derived here for momentum and energy reduce to the known expressions for a single resonance Lorentz dielectric [65, 87].

The average momentum density vector of a monochromatic wave may be either parallel or antiparallel to the average Poynting vector in a material with negative index of refraction. However, the momentum conservation equation given by (3.19) depends only upon the average momentum flow in (3.18). Thus, it is expected that any observation of momentum transfer in RHM or LHM due to a monochromatic wave is independent of the details of dispersion. Furthermore, these results provide a rigorous derivation of the force on free currents and further validation of the theoretical separation of force based on the real and imaginary parts of the permittivity and permeability. The theory was applied to calculate the radiation pressure on an infinite half-space and a lossy slab. For the hypothetical problem of a lossless half-space (*i.e.* $\mu_I = \epsilon_I = 0$), the material is pulled toward the incident wave when $n > 1$ [61] and pushed when $n < 1$, which includes the negative index regime. Also, a slab in vacuum is pushed by a monochromatic wave regardless of the values for μ and ϵ. This differs from the results previously reported for a finite pulse, where it was concluded that the pulse attracts a slab when $0 < \mu, \epsilon < 1$. It is possible, however, to consider a slab embedded in a left-handed vacuum [92], where the replacements $\mu_0 \rightarrow -\mu_0$ and $\epsilon_0 \rightarrow -\epsilon_0$ are made for the free space background. In this case, the slab is pulled toward the incident wave consistent with the prediction of radiation attraction by Veselago [82].

Finally, we may conclude that the theory presented here attaches fundamental

physical meaning to Snell's law; the reflected and transmitted wave vectors ensure conservation of the momentum component which is parallel to the boundary. Likewise, the magnitudes of the reflected and transmitted waves ensure conservation of wave energy at the interface. This assertion holds for LHM and ensures that no sheering force exists due to R/T at the interface.

Chapter 4

Optical Manipulation of Mesoscopic Particles

In this chapter, the previously derived theory is applied to model the forces exerted on particles by an optical field. The modeling process requires two steps, which may be carried out independently. First, the total fields must be found, which can be done by numerical or analytical techniques. The particles considered here are canonical geometries so that an analytical solution for the total field is known. Second, the force on the particle is calculated by either applying the Lorentz force directly to the material or by invoking the momentum conservation theorem derived in the previous chapters. It is shown that analytical solution for the fields and the Maxwell stress tensor divergence provide a numerically efficient solution. Both two-dimensional (2-D) particles and three-dimensional (3-D) particles are modeled using the Mie theory for a cylinder and sphere, respectively. The cylindrical particle is used as a computationally efficient way to understand phenomena and will be used in the following chapter to model the optical binding phenomenon, while the sphere more closely resembles 3-D particles used in many experiments.

4.1 Two-dimensional dielectric and magnetic particles

The total fields due to the scattering of an in-plane electromagnetic wave by an infinite cylinder is calculated from the Mie solution given in Appendix B. The incident field is s-polarized (*i.e.* the electric field is parallel to the cylinder axis). In this section, three configurations of incident waves are considered. First, the scattering force due to a single plane wave incidence is described in terms of momentum scattering and, equivalently, in terms of a gradient force. Second, multiple plane wave interference patterns are considered. The three and four plane wave incidences are such that the net incident momentum is zero so that the force on particles in the Rayleigh regime are described simply in terms of the gradient of the incident intensity pattern. However, it is shown that this simple description is not valid for larger particles. Third, an incident laser is modeled as a spectral Gaussian beam. This configuration is applied in a 2-D study of optical trapping.

4.1.1 Scattering force on a dielectric cylinder

In this section, an infinite cylinder in $\hat{z}$ is incident by a s-polarized (TM) wave as shown in Fig. 4-1. That is, an electromagnetic wave $\bar{E}_{inc} = \hat{z}e^{\bar{k}_i \cdot \bar{\rho}}$ is incident upon an infinite cylinder of radius a and characterized by (μ_p, ϵ_p) set in a background of (μ_b, ϵ_b). The incident wave vector is in the plane so that $\bar{k}_i = k_i(\hat{x}\cos\phi_i + \hat{y}\sin\phi_i)$, where $k_i = \omega\sqrt{|\mu_p||\epsilon_p|}exp(i(\arg\mu_p + \arg\epsilon_p)/2)$ and ϕ_i is the incident angle in the xy plane. Various field distributions, such as a Gaussian beam, can be described by a sum of plane-waves.

The so-called scattering force results from the transfer of linear momentum from an incident wave to a dielectric particle. Alternatively, the force can be computed by applying the Lorentz force directly. Since the incident electric field is polarized parallel to the cylinder axis, the bound electric charges at the surface are zero, and the

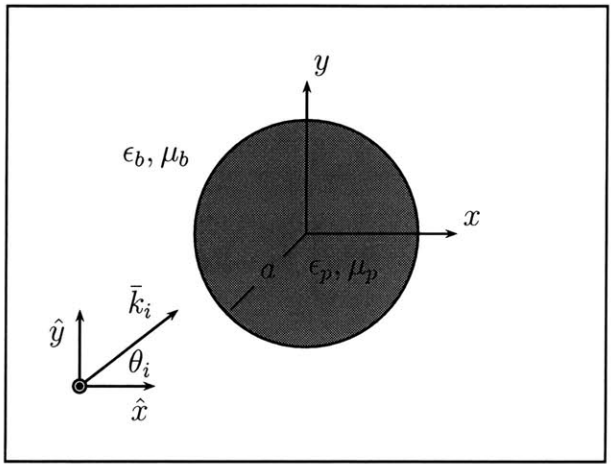

Figure 4-1: An infinite cylinder is used to represent optical manipulation of mesoscopic particles in 2-D. The cylinder of radius a is composed of isotropic material (μ_p, ϵ_p) in a background of (μ_b, ϵ_b). Various incident fields are given by a sum of plane waves each with a different wave vector $\bar{k}_i$. The total fields inside and outside the cylinder are computed using the formulation of Appendix B.

total force $< \bar{F} >$ per unit length (N/m) is obtained by integrating the bulk Lorentz force density $< \bar{f}_{bulk} >= \frac{1}{2}\Re\{-i\omega\bar{P} \times \bar{B}^*\}$ over the cross section of the cylinder. The numerical integration is performed by summing the contribution from discrete area elements. The area elements $\Delta A = \Delta x \Delta y$ are taken to be identical so that the numerical integration is

$$< \bar{F} >= \iint_S dA \frac{1}{2}\Re\{\bar{f}_{bulk}\} \approx \Delta A \sum_{l=1}^{L} \frac{1}{2}\Re\{-i\omega\bar{P}_l \times \mu_0 \bar{H}_l^*\}, \tag{4.1}$$

where the dielectric polarization $\bar{P}_l$ and magnetic field $\bar{H}_l$ are evaluated at each point indexed by l in the cross section of the cylinder.

In contrast, the stress tensor divergence reduces to a line integral for the 2-D problem. The line integral is evaluated by simple numerical integration, although Grzegorczyk recently derived an analytical expression for the force on a dielectric cylinder by integrating the line integral analytically [93]. However, this analytic expression for the force is valid only for a single nonmagnetic cylinder and was published

after the work contained in this chapter was completed. The integration path chosen is a circle of radius $R > a$ concentric with the particle and the integration steps ($R\Delta\phi$) are constant. The numerical integration is computed by

$$< \bar{F} >= -\frac{1}{2}\Re\left\{ \int_0^{2\pi} \hat{n} \cdot \bar{\bar{T}}(R,\phi) R d\phi \right\} \approx -R\Delta\phi \sum_{m=1}^{M} \frac{1}{2}\Re\{\hat{n} \cdot \bar{\bar{T}}(R,\phi_m)\}, \qquad (4.2)$$

where the values of ϕ_m result from the discretization of $\phi \in [0, 2\pi]$.

As an example, Fig. 4-2 shows the total field intensity resulting from an electromagnetic plane wave incident at $\phi_i = \pi/4$, which demonstrates that the Mie solution presented in Appendix B is easily rotated to model an arbitrary incident angle. Typically, the radiation pressure on a particle is described in terms of the scattering of incident electromagnetic momentum. Of course this viewpoint is formalized by calculating the divergence of the Maxwell stress tensor. However, a more fundamental viewpoint is obtained by considering the Lorentz force applied directly to the particle. In this regard, it may be argued that the optical forces exist everywhere inside the particle once the incident field is present. This force distribution is represented in Fig. 4-2 by the arrows, which are seen to point toward regions of high electric field intensity. Thus, regions of compression and tension may be identified inside the particle. Such distributions of high force densities may be detrimental to certain types of particles such as living cells. Furthermore, the scattering force on a particle may be equivalently described by a pulling toward the high intensity focus.

4.1.2 Multiple plane wave interference pattern

Optical manipulation of colloidal particles is typically achieved by creation of an incident optical intensity gradient. One such configuration consists of three lasers with $2\pi/3$ incident angle separation [94]. Such a configuration results in a zero net incident momentum since $\sum_i^3 \bar{k}_i = 0$, which allows us to isolate the so-called gradient force. Furthermore, we may also consider any number of symmetric incidences. For

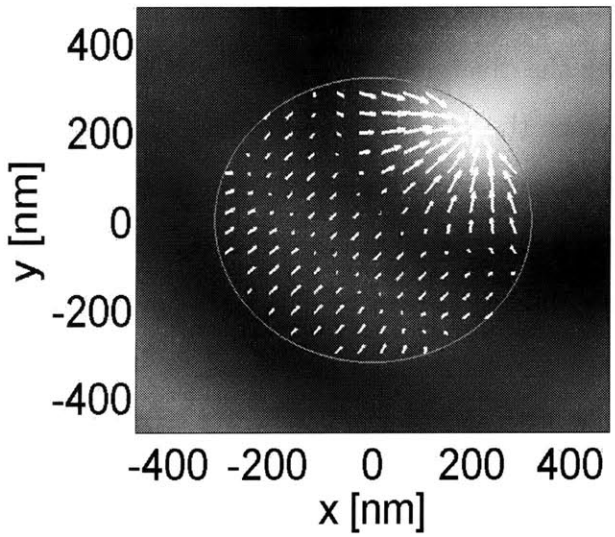

Figure 4-2: Lorentz force density on bound currents (arrows) overlayed on the electric field intensity $|E_z|^2$ $[(V/m)^2]$. The force on the dielectric cylinder results from a $\hat{z}$ polarized plane wave of unit amplitude incident from free-space ($\epsilon_b = \epsilon_0, \mu_b = \mu_0$) with wavelength $\lambda_0 = 1064\ nm$. The constitutive parameters for the lossless cylinder are $\epsilon_p = 2\epsilon_0$ and $\mu_p = \mu_0$. The angle of incidence is $\phi_i = \pi/4$.

example, a pair of counter propagating waves produce an optical potential landscape in one dimension. Here the analysis is focused on interference fringes created by three and four symmetric incidences.

The interference of three plane waves having wave vectors with incident angles separated by $2\pi/3$ in the xy plane creates a hexagonal intensity pattern. This interference is represented by the background of Fig. 4-3 where white denotes regions of high intensity. The effective force on a polystyrene particle ($\epsilon_p = 2.56\epsilon_0, \mu_p = \mu_0$) in water ($\epsilon_b = 1.69\epsilon_0, \mu_b = \mu_0$) is calculated from the incident and scattered electromagnetic wave momenta via the divergence of the Maxwell-Minkowski stress tensor. The overlayed arrows represent the relative force pattern on a dielectric cylinder, which spans the plane. That is, each arrow represents the direction and relative magnitude of force on a dielectric cylinder placed at the tail of the arrow. The force on the small particle with radius $a = 0.15\lambda_0$ is seen to closely follow the high intensity gradient of the incident field with stable optical traps occurring in the high intensity regions. However, larger particles with radius $a = 0.30\lambda_0$ are repelled from the high intensity regions and find stable trapping positions in the dark regions of the incident optical interference pattern. This is in contrast to the gradient force obtained in the Rayleigh approximation and demonstrates that such an approximation yields results which are both quantitatively and qualitatively incorrect for particles that are on the order of a wavelength. The reason, of course, is that the larger particles cause greater disturbance of the incident field pattern and interact with the neighboring high intensity traps. Thus, a larger particle my find an equilibrium such that it's center is in a dark region while the particle is held in place by the interaction with multiple bright regions.

Next, the interference of four plane waves having wave vectors with incident angles separated by $\pi/2$ is considered. The intensity pattern in this case forms a square pattern as shown by the background of Fig. 4-4. Again, the effective momentum transfer to a polystyrene cylinder in water is calculated and represented by the arrows

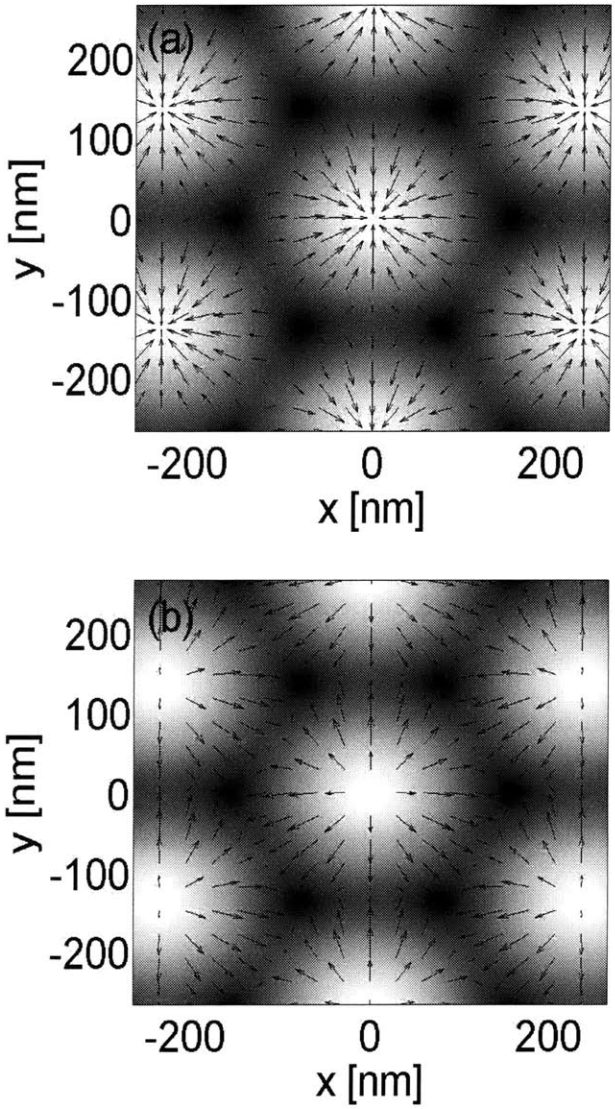

Figure 4-3: Force per unit length (represented by the arrows) on a single infinite cylinder due to the interference of three plane waves (represented by the background pattern) of equal amplitude $E_i = 1\ [V/m]$ and wavelength $\lambda_0 = 532\ nm$. The incident angles of the plane waves are $\{\pi/2, 7\pi/6, 11\pi/6\}$. The background medium is water $\epsilon_b = 1.69\epsilon_0$, and the cylinder is polystyrene $\epsilon_p = 2.56\epsilon_0$ with radius (a) $a = 0.15\lambda_0$ and (b) $a = 0.30\lambda_0$.

for a small particle $a = 0.15\lambda_0$ in Fig. 4-4 (a) and a larger particle $a = 0.30\lambda_0$ in Fig. 4-4 (b). As before, the small particle is attracted to the high intensity regions while the large particle is repelled from the regions of incident high intensity.

One obvious question regarding the analysis of multiple plane wave interference patterns pertains to the transition from small to large particles. That is, we may ponder what happens to the distribution of arrows in the previous two figures when a particle is between $a = 0.15\lambda_0$ and $a = 0.30\lambda_0$. Although we have not completed the analysis of this regime, we may consider an example case of a single intermediate value of radius. For example, the force on a particle with radius $a = 0.225\lambda_0$ is plotted over the background of the incident three plane wave interference pattern in Fig. 4-5. An interesting feature of this plot is that the force field appears to be non-conservative. That is a particle moving from one side of a vortex in a dark region to the other requires a different amount of work depending upon the path taken. Therefore, it may not be possible to describe such an interference pattern as an optical potential landscape. A prediction of stable optical trapping in these vortices has been reported by Grzegorczyk [95]. In contrast, no such vortices are seen for the four plane wave interference pattern of Fig. 4-5 (b). However, further investigation into the nature of the forces in such incident interference patterns is still underway using the analytical expressions for the force [93].

The analysis of multiple plane wave interference patterns is concluded with a study of the numerical efficiency of the force calculation methods. Figure 4-6 shows the force versus the number of integration points for application of (4.2) using an integration radius of $R = 1.01a$. The results show that the integration converges rapidly. Because the force is calculated by a divergence integral, the result does not depend on the value of $R > a$, provided enough integration points are chosen and the background medium is lossless. To confirm this, the force was calculated for various choices of integration radius yielding zero for all $R < a$ and $\bar{F} = \hat{y}2.1190 \cdot 10^{-18}[N/m]$ for all $R > a$. Likewise, the $\hat{y}$-directed force is plotted in Fig. (4-7) versus the number

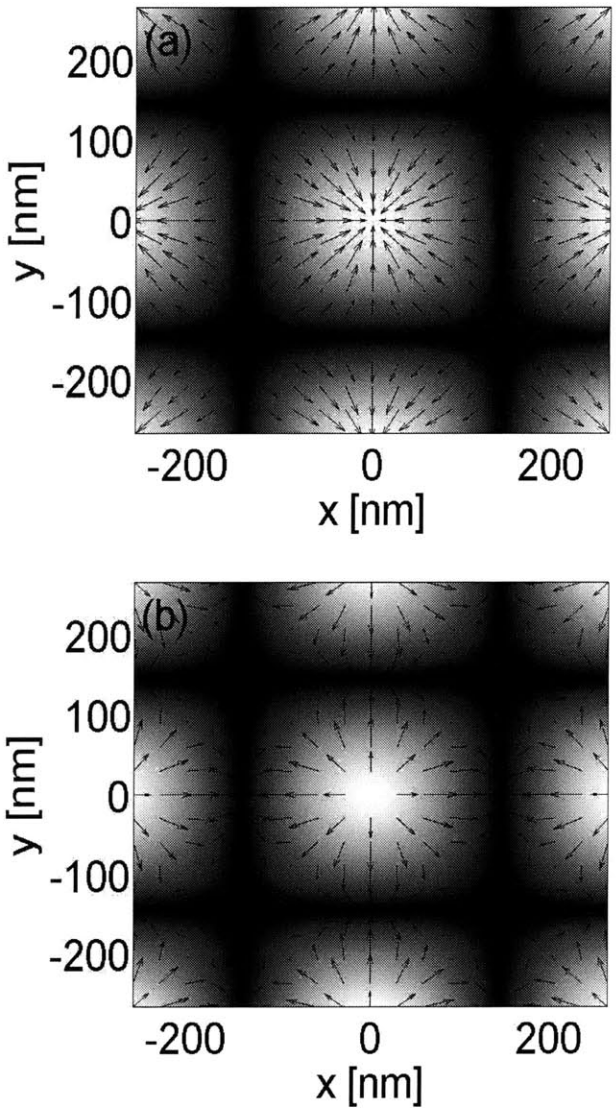

Figure 4-4: Force per unit length (represented by the arrows) on a single infinite cylinder due to the interference of four plane waves (represented by the background pattern) of equal amplitude $E_i = 1\ [V/m]$ and wavelength $\lambda_0 = 532\ nm$. The incident angles of the plane waves are $\{\pi/4, 3\pi/4, 5\pi/4, 7\pi/4\}$. The background medium is water $\epsilon_b = 1.69\epsilon_0$, and the cylinder is polystyrene $\epsilon_p = 2.56\epsilon_0$ with radius (a) $a = 0.15\lambda_0$ and (b) $a = 0.30\lambda_0$

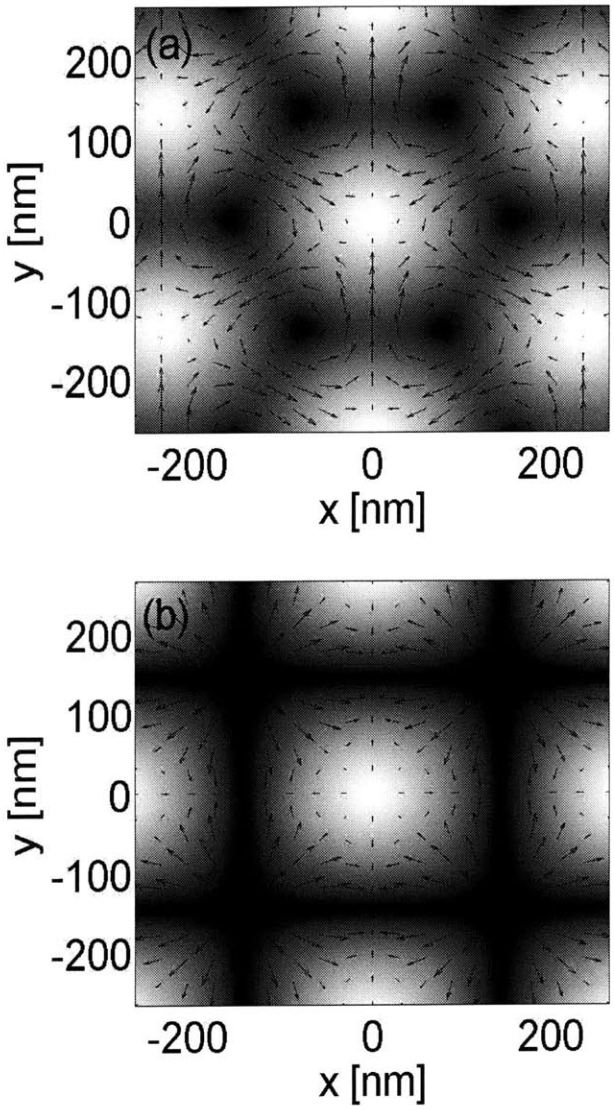

Figure 4-5: Force per unit length (represented by the arrows) on a single infinite cylinder due to the interference of plane waves (represented by the background pattern) of equal amplitude $E_i = 1\ [V/m]$ and wavelength $\lambda_0 = 532\ nm$. The background medium is water $\epsilon_b = 1.69\epsilon_0$, and the cylinder is polystyrene $\epsilon_p = 2.56\epsilon_0$. (a) The 3 plane waves are incident at $\phi_i = \{\pi/2, 7\pi/6, 11\pi/6\}$ onto a cylinder of radius $a = 0.225\lambda_0$. (b) The 4 plane waves are incident at $\phi_i = \{\pi/4, 3\pi/4, 5\pi/4, 7\pi/4\}$ onto a cylinder of radius $a = 0.25\lambda_0$.

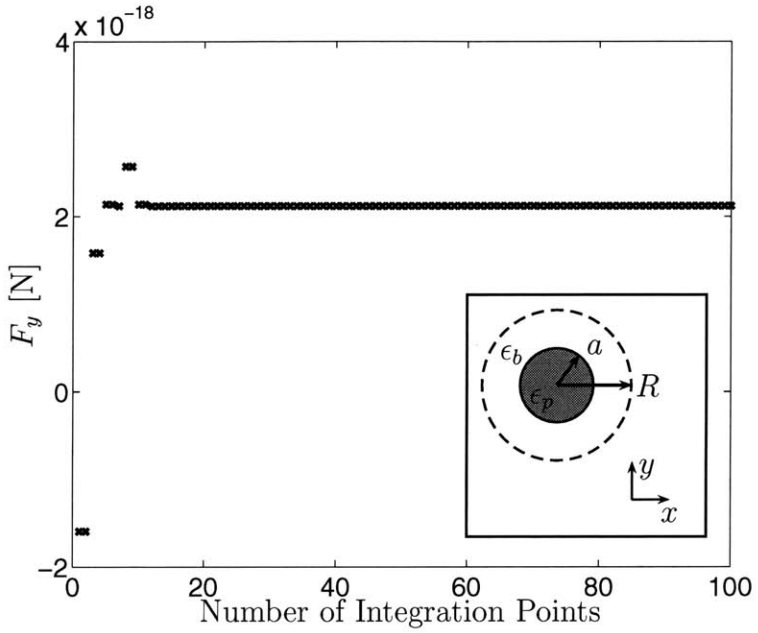

Figure 4-6: Number of integration points used for convergence of the line integral of the Maxwell stress tensor. The integration path, shown by the inset diagram, is a circle of radius of $R = 1.01a$ concentric with the cylinder of radius $a = 0.3\lambda_0$ at center coordinates $(x_c, y_c) = (0, 100)$ $[nm]$. The three identical plane waves are incident upon a polystyrene cylinder ($\epsilon_p = 2.56\epsilon_0$) in water ($\epsilon_b = 1.69\epsilon_0$). © 2006 Koninklijke Brill NV [3]

of integration points used to numerically integrate the Lorentz force in (4.1). Since the background is water ($\epsilon_b = 1.69\epsilon_0$), the effective transfer of electromagnetic wave momentum is calculated via the Lorentz force by making the replacement $\epsilon_0 \rightarrow \epsilon_b$ such that the effective polarization is $\bar{P} = (\epsilon_p - \epsilon_b)\bar{E}$. The integral converges much slower than the line integral applied to the stress tensor, however the resulting force is $\bar{F} = \hat{y}2.1191 \cdot 10^{-18}[N/m]$, thus matching the result from the Maxwell stress tensor.

4.1.3 Dielectric particle in a Gaussian beam

A more commonly used optical intensity gradient is a highly focused laser beam, which is modeled by the spectral Gaussian beam. Focused lasers have been used to trap, levitate, and accelerate particles since the pioneering work of Ashkin [12–14, ?–14].

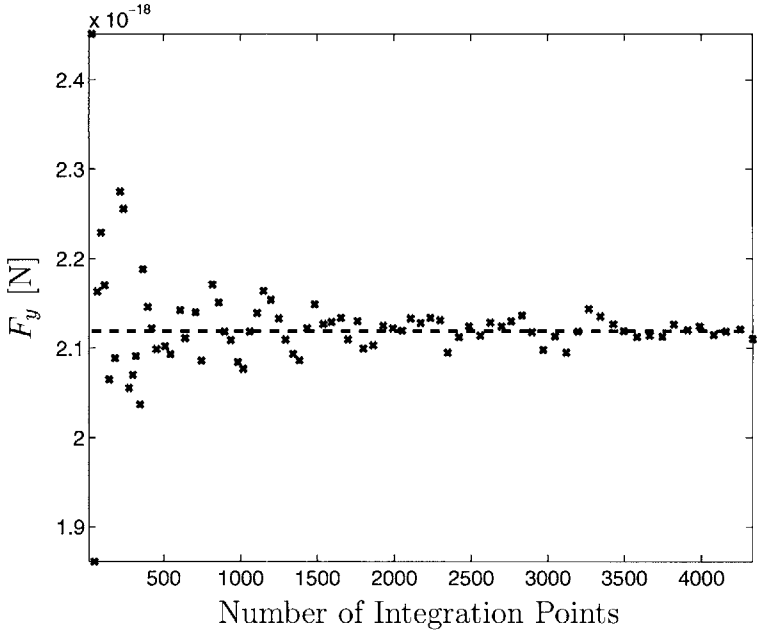

Figure 4-7: Convergence of Lorentz force surface integration for calculation of force on a dielectric cylinder ($\epsilon_p = 2.56\epsilon_0$) in water ($\epsilon_b = 1.69\epsilon_0$). The configuration is the three plane wave interference pattern and particle with radius $a = 0.3\lambda_0$ placed at center coordinates $(x_c, y_c) = (0, 100)$ $[nm]$. The dashed line is the force computed using the stress tensor with 100 numerical integration points on a concentric circle of radius $R = 1.01a$. © 2006 Koninklijke Brill NV [3]

In two dimensions, the incident field of a Gaussian beam polarized in $\hat{y}$ is [96]

$$\bar{E}_{inc} = \hat{y} E_0 \frac{w}{2\sqrt{\pi}} \int_{-\infty}^{\infty} dk_x e^{-\frac{w^2 k_x^2}{4}} e^{ik_x x + ik_z z}, \tag{4.3}$$

where $k_z^2 = k_b^2 - k_x^2$, $k_b^2 = \omega^2 \mu_b \epsilon_b$, and w is the beam waist. The electric field in (4.3) satisfies the Helmholtz wave equation [39] and is implemented as a discrete sum of plane waves. In reality, the spectrum is limited by the optics of the system, and the sum is implemented here within the domain $|k_x| \leq NA\frac{\omega}{c}$, where NA is the numerical aperture of the objective lens [97]. The field in (4.3) is implemented numerically as a discrete sum, with 40 plane waves typically used for the analysis in this thesis.

Figure 4-8 shows the force on a particle in water due to a Gaussian beam with incident intensity represented by the background shading. The force on the particle is calculated at each point by first finding the total field (incident and scattered) and applying the Maxwell-Minkowski stress tensor. In Fig. 4-8 (a), the dielectric particle is optically dense compared to the background medium. It is pulled into the axis of the beam and pushed by radiation pressure. In contrast, Fig. 4-8 (b) shows that an air bubble, which is optically less dense than the water, is pushed out of the beam axis and pushed in the propagation direction. This result qualitatively models the original accelerating and trapping experiments of Ashkin [12]. This is an important result because the effective force on each particle has been calculated from the scattered electromagnetic wave momentum. In reality, the force on the air bubble is zero since the permittivity is closely matched to free space and the polarization is negligible (*i.e.* $\bar{P} \approx 0$). The bubble is actually pushed out of the center of the beam due to the forces on the liquid surrounding the bubble. Here, the analysis is simplified by applying the results of the previous chapters to model the observed behavior of the bubble in a laser beam. This approach to calculation has recently been applied to spherical particles to achieve quantitative agreement with experimental measurements of trap stiffness [97–99].

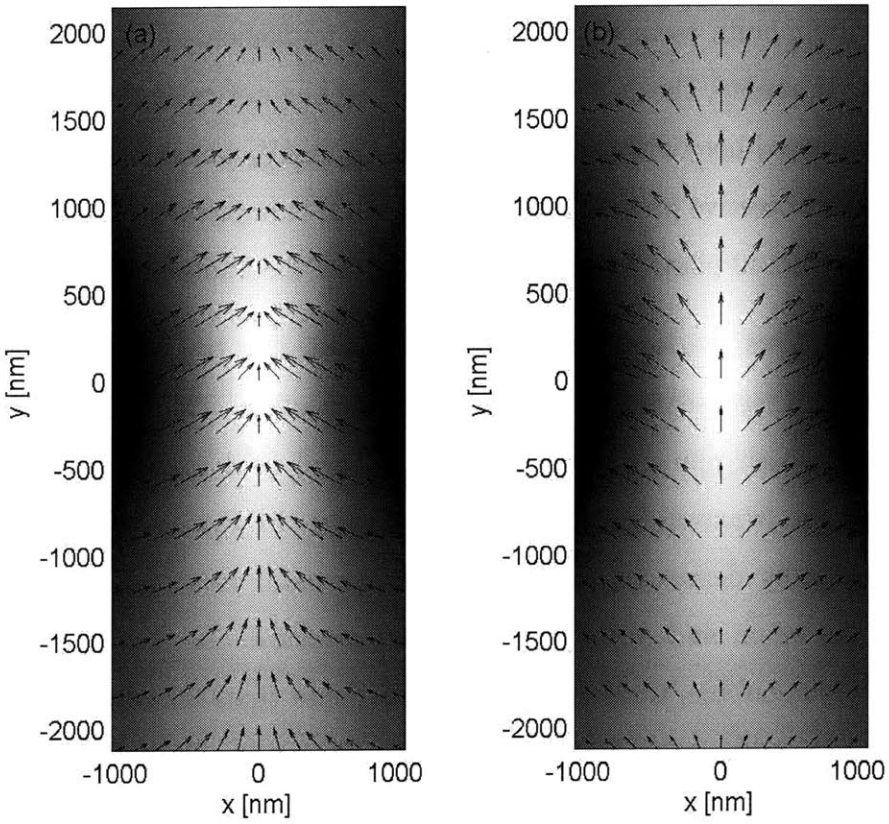

Figure 4-8: Force per unit length (represented by the arrows) on a single infinite cylinder due to an incident Gaussian beam with $NA = 1$, $E_0 = 1$, $w = 0.5\lambda_0$, and wavelength $\lambda_0 = 1064\ nm$. The background medium is water $\epsilon_b = 1.69\epsilon_0$ and the radius of the particle is $a = 0.5\lambda_0$. The particle is (a) polystyrene ($\epsilon_p = 2.56\epsilon_0$) and (b) air bubble ($\epsilon_p = \epsilon_0$).

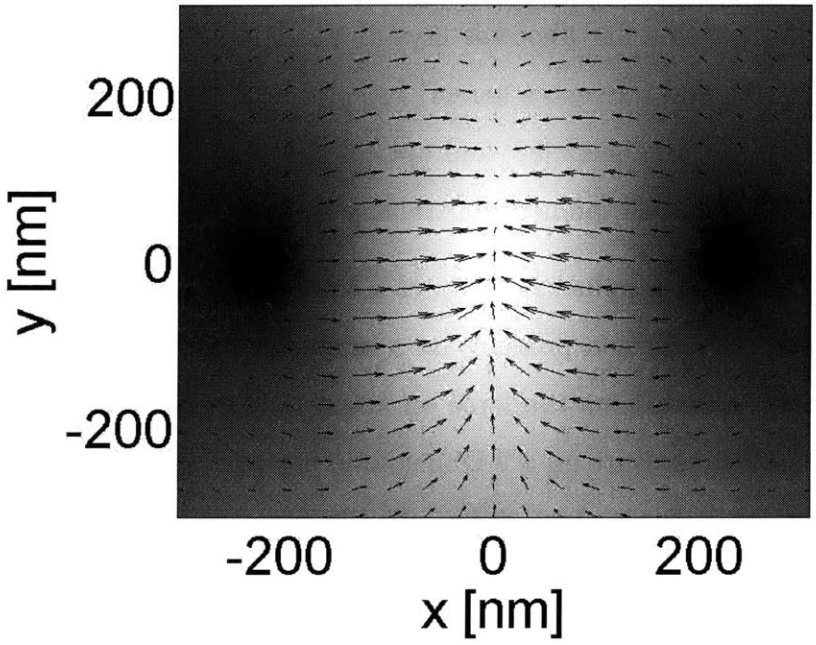

Figure 4-9: Classical optical tweezers modeled by a 2-D dielectric particle in water. The arrows represent the force on a silica particle with index of refraction $n_p = 1.46$ and radius $a = 50\ nm$ in water ($n_b = 1.33$). The incident laser is modeled as a Gaussian beam with waist $w = 0.2\lambda_0$, $\lambda_0 = 514.5\ nm$, and spectrum defined by $NA = 1.25$.

The classical optical tweezers first realized in 1986 by Ashkin and colleagues [22] can also be reproduced with 2-D particles. Figure 4-9 shows the reversal of radiation pressure on a silica cylinder due to a single tightly focused beam. The parameters match closely the experimental conditions used in the original experiments to trap silica beads. Thus, the infinite cylinder can be trapped in the plane by a single focused Gaussian beam.

4.1.4 Scattering force on a magnetic cylinder

Magnetic particles have not been trapped in the laboratory since naturally occurring materials do not exhibit significant magnetic response at optical wavelengths. However, there are materials that exhibit magnetic response up to microwave frequencies,

and researchers have recently trapped large particles (diameters up to 600 μm) by focusing microwaves with a flat photonic crystal lens [100]. Also, metamaterials (see for example [101, 102] and references herein) have recently been developed with magnetic response into the Terahertz [58] and optical [59] frequencies and offer hope for future experiments of optical momentum transfer in magnetic media.

The Lorentz force was applied in Chapter 2 to bound magnetic charges and currents to calculate the radiation pressure on a magnetic slab. However, the method has not been used to determine the force on magnetic particles. In this section, we calculate the radiation pressure on a 2-D magnetic particle represented by an infinite cylinder incident by a single plane wave. The incident plane wave $\bar{E}_i = \hat{z}E_i e^{ik_0 x}$ propagates in free space (ϵ_0, μ_0) with a wavelength $\lambda_0 = 2\pi/k_0 = 640$ $[nm]$. The 2-D magnetic particles $(\epsilon_0, 3\mu_0)$ are infinite in the $\hat{z}$-direction. The Maxwell stress tensor and the distributed Lorentz force methods are applied to calculate the total force on the particles. The direct application of the Lorentz force requires the model of bound magnetic currents $i\omega\mu_0\bar{M}$ in (2.9a) and bound magnetic surface charges ρ_h in (2.9b). Agreement between the two methods is shown in Fig. 4-10 as a function of particle radius. The oscillations in force are a result of internal resonances, which is also evident for the case of dielectric and magnetic slabs incident by plane waves.

There are noticeable differences between the results of the two methods for larger values of a as shown in Fig. 4-10. This is due to increased spatial variations in force distribution for particles on the order of a wavelength or larger. The slow convergence of the total Lorentz force has been observed for small dielectric particles as shown in Fig. 4-7 and becomes a major obstacle for obtaining many digits of accuracy from the Lorentz force for large particles. To illustrate this point, we compare the force calculated for the magnetic particle with radius $a = 1000$ nm with various number of integration points N in Table 4.1. For each calculation, 200 points are used for the calculation of force on bound surface charges, which was determined to be enough for the number of significant digits reported. The force obtained from the stress

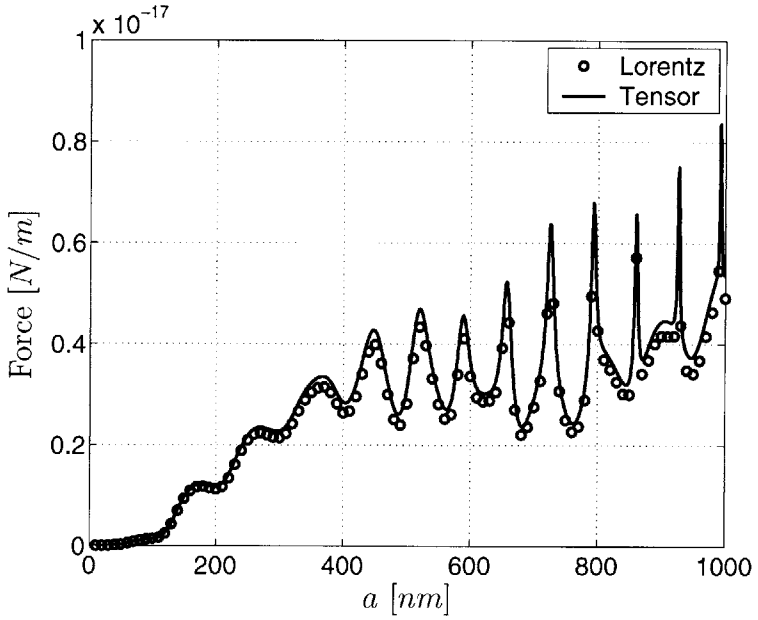

Figure 4-10: Radiation pressure on a magnetic cylinder ($\mu_p = 3\mu_0, \epsilon_p = \epsilon_0$) versus the radius a. The $\hat{z}$-polarized plane wave propagates in the $\hat{x}$-direction in free space ($\mu_b = \mu_0, \epsilon_b = \epsilon_0$), and the wavelength is 640 $[nm]$. The force is calculated by the divergence of the stress tensor (line) and the Lorentz force on bound currents and charges (markers). © 2006 Koninklijke Brill NV [3]

Table 4.1: Radiation Pressure on a Magnetic Particle ($a = 1000$ [nm])

Number of Integration Points	Total Lorentz Force $< F_x >$
25,952	$4.8177 \cdot 10^{-18}$ [N/m]
103,336	$4.9175 \cdot 10^{-18}$ [N/m]
282,868	$4.9498 \cdot 10^{-18}$ [N/m]

tensor approach is $5.3524 \cdot 10^{-18}$ [N/m], which converges within 100 points. It is clear that for this particular case, the total Lorentz force converges so slowly that it could hinder studies involving multiple particles or variations in multiple parameters. For many applications, however, the Lorentz force is useful for getting a picture of force distribution inside the particle, while the divergence of the stress tensor is much more efficient for obtaining the total force on the particle.

4.2 Absorbing Mie particles

The Lorentz force density and momentum conservation are equivalently applied to explain relevant experimental observations and to calculate the radiation pressure on absorbing Mie particles. In contrast to the scattering plus absorption forces derived for small particles, we predict that absorption can reduce the total optical momentum transfer to certain particles due to the balance between the force on free currents and the force on bound currents and charges. Thus, the theory of optical momentum transfer to absorbing macroscopic media is applied to predict and explain new physics in this study.

4.2.1 Lossy dielectric cylinder

The total fields due to plane-wave incidence on a 2-D particle are found from Mie theory applied to an absorbing infinite cylinder. We consider two separate problems of $\bar{E}_{inc} = \hat{z}e^{ik_0 x}$ incident from free space onto a lossless cylinder and onto a lossy cylinder, each of diameter 0.5 μm. The choice of an infinite dielectric cylinder incident by a

TE wave allows for a complete description of the Lorentz force by the distribution inside the particle since the force on bound charges at the boundary is zero. The total electric field intensity is shown in Fig. 4-11(a) for the lossless dielectric particle. The total force is the force on bound currents $< \bar{F} >= \bar{F}_b = \hat{x}4.02 \cdot 10^{-18}\ N/m$, which is computed by integrating the force density (2.8) over the area of the particle or, equivalently, by integrating the stress tensor of (2.14) along the circular path shown in Fig. 2-1(a). The integration is performed by simple numerical integration. Although equivalent in results, the former approach provides the viewpoint that the particle is pulled toward the resulting high intensity focus, while the latter gives the usual intuition of a particle being pushed by the transfer of wave momentum. The total electric field intensity and force density on bound currents for a lossy particle is shown in Fig. 4-11(b). The resulting force density $< \bar{F}_b >= -\hat{x}2.05 \cdot 10^{-18}\ N/m$ indicates that the bound currents are pulled toward the incident wave, which is offset by a positive momentum transfer to free currents represented by $< \bar{F}_c >= \hat{x}5.80 \cdot 10^{-18}\ N/m$, found equivalently by applying an integration path to the stress tensor shown in Fig.2-1(b). The total pressure on the particle is $< \bar{F} >= \hat{x}3.75 \cdot 10^{-18}\ N/m$, which is less than the total force on the transparent particle.

4.2.2 Lossy dielectric sphere

A physically realistic situation of an electromagnetic wave impinging on a spherical particle is studied using Mie theory. For $\epsilon_R/\epsilon_0 = 2$, Fig. 4-12 (a) shows that a maximum optical momentum transfer occurs for a value of ϵ_I near maximum absorption (*i.e.* the penetration depth is on the order of the particle diameter). In contrast, a particle with large value for ϵ_R can exhibit reduced momentum transfer due to significant wave attenuation in the sphere as shown in Fig. 4-12 (b). A further decrease in $< F >$ for the high contrast sphere is observed as ϵ_I approaches the limit of a perfect reflector. The later point is made by comparing the adiabatic momentum transfers to the transparent dielectric sphere and to the reflecting sphere of equal size. How-

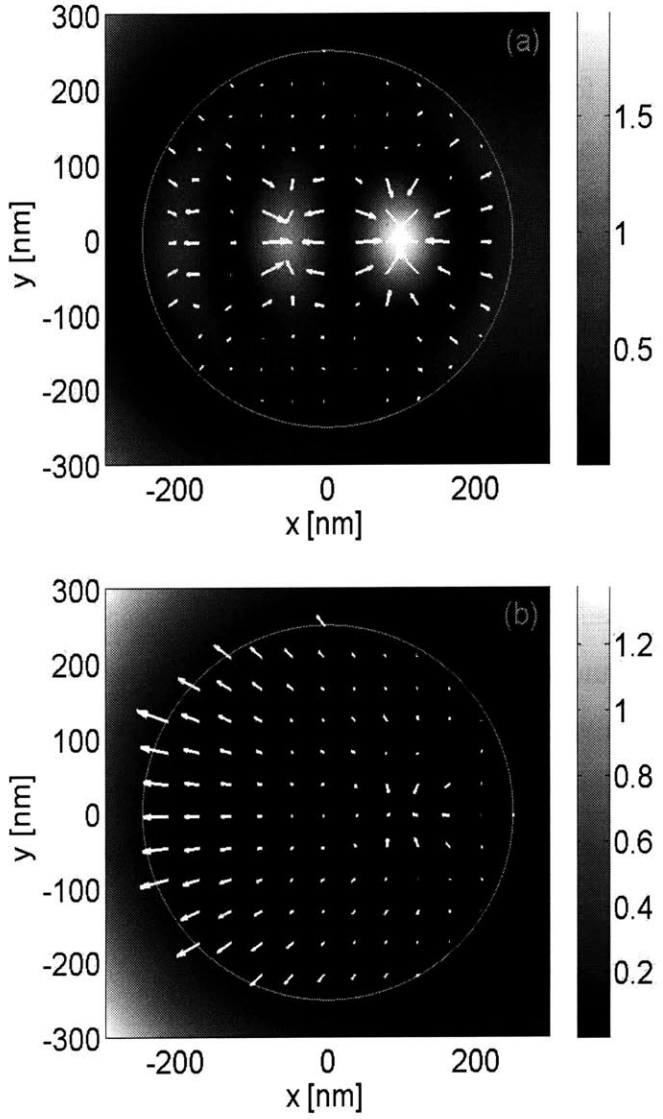

Figure 4-11: Lorentz force density on bound currents (arrows) overlayed on electric field intensity $|E_z|^2$ $[(V/m)^2]$ resulting from a $\hat{z}$ polarized plane wave of unit amplitude incident from free-space with wavelength $\lambda_0 = 1064\,nm$ onto a dielectric cylinder. (a) The lossless cylinder is defined by $\epsilon = 16\epsilon_0$. $(max(| < f_b > |) = 1.25 \cdot 10^{-6}\ [N/m^3])$ (b) The lossy cylinder, described by $\epsilon = (16 + i \cdot 10)\epsilon_0$, contains an additional force density on free currents. $(max(| < f_b > |) = 3.00 \cdot 10^{-9}\ N/m^3)$ ©2006 The American Physical Society [4].

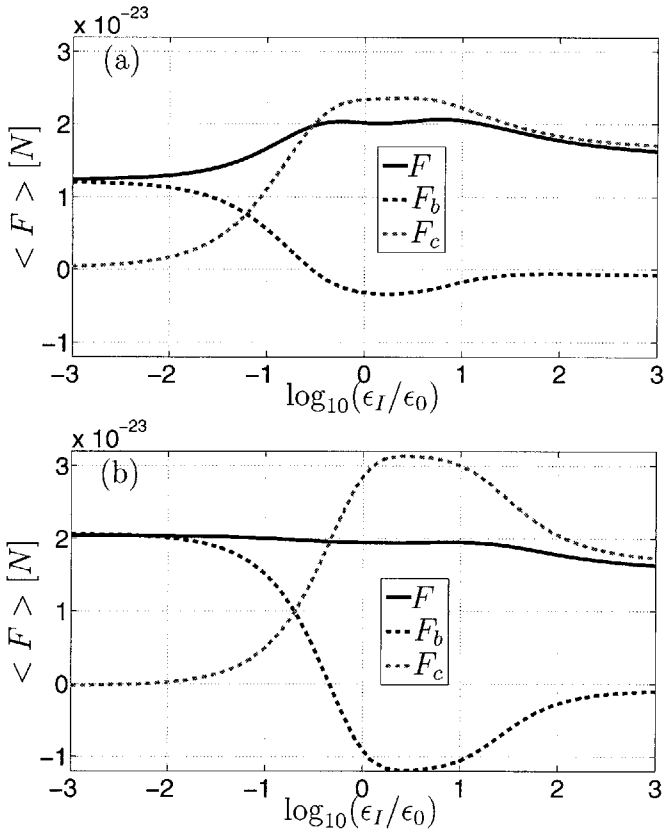

Figure 4-12: Forces on a 2 μm diameter sphere due to a plane wave of unit amplitude. The wave is incident from free space with wavelength $\lambda_0 = 1064\ nm$ onto a nonmagnetic sphere with (a) $\epsilon = 2\epsilon_0 + i\epsilon_I$ and (b) $\epsilon = 16\epsilon_0 + i\epsilon_I$. ©2006 The American Physical Society [4].

ever, the combined effect of $< F_b >$ and $< F_c >$ is required to explain the radiation pressure increase of Fig. 4-12 (a) or decrease of Fig. 4-12 (b) due to absorption. This separation of $< F >$ into $< F_b >$ and $< F_c >$ is further investigated by plotting the force versus sphere diameter for constant material parameters in Fig 4-13. For small spheres, the power absorption is small since the diameter is much less than the penetration depth. When the diameter is of the order of the penetration depth, the force on free currents becomes significant due to the direct dependence upon n given by (2.12).

A perspective of momentum transfer in lossy media has been applied to study

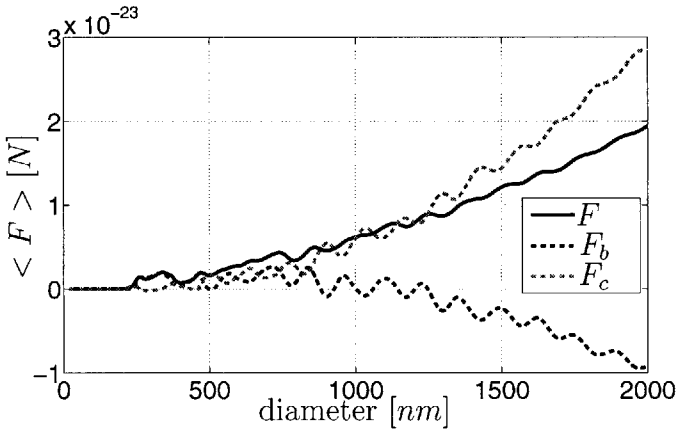

Figure 4-13: Force versus diameter for a dielectric sphere ($\epsilon/\epsilon_0 = 16 + i$) incident by a unit amplitude plane wave. The free space wavelength of the incident wave is $\lambda_0 = 1064\ nm$. ©2006 The American Physical Society [4].

momentum transfer to particles. In the case of an absorbing Mie particle, the contributions from $\bar{F}_b$ and $\bar{F}_c$ sum to give the total force on the particle. The particles we consider consist of $\epsilon_R = 16\epsilon_0$, a value typical for semiconductors, and $\epsilon_R = 2$, which is representative of many insulators. A novelty of our results is the reduction of optical momentum transfer to particles due to absorption, which requires high dielectric contrast with the background medium and an attenuation length on the order of particle diameter. These results differ from the expected result of scattering plus absorption forces resulting from Rayleigh particles [29]. Because a detailed understanding of both $\bar{F}_b$ and $\bar{F}_c$ are required to describe the physics involved, the theory presented here is fundamental to the understanding of optical momentum transfer to absorbing particles.

4.3 Discussion

The optical forces exerted upon 2-D particles have been calculated from both the divergence of the Maxwell stress tensor and the direct application of the Lorentz force to bound currents and charges. The Lorentz force is applied directly to bound

currents and charges used to model dielectric and magnetic materials. The advantage of the stress tensor approach for force calculation on 2-D particles is that it reduces a combination of surface integral over the bulk force density $< \bar{f}_{bulk} >$ and a line integral over the surface force density $< \bar{f}_{surf} >$ to a single line integral over the Maxwell stress tensor. This reduction in computation has been demonstrated by example. The Lorentz force, however, can give the force distribution throughout the particle. Such distributions can be important when optical forces are applied to sensitive objects such as in biological applications. For large particles, the total force may be difficult to obtain accurately from the Lorentz force density, which is illustrated by calculating the radiation pressure on a magnetic particle. It was shown that in some cases the radiation pressure on a cylinder may be described in terms of the gradient of the total field. Likewise, the force on a particle in an optical interference pattern may not always be directed toward the high intensity regions. Thus, there is certainly a need for description of optical manipulation beyond gradient and scattering forces. Furthermore, there may be evidence that particles in an optical interference pattern may be subject to non-conservative forces. That is, in some cases, the work done on a particle moving from one point to another will depend upon path. This line of research is still underway using the analytical expressions developed by Grzegorczyk [93].

Dielectric cylinders in a Gaussian beam were used to model the early trapping experiments by Ashkin [12, 22]. The results presented here are important for two reasons. First, the qualitative agreement with experimental observations of trapped particles submerged in a dielectric liquid is a direct consequence of the scattering of electromagnetic wave momentum derived in the previous chapters. In particular, direct application of the Lorentz force yields a zero force density everywhere inside an air bubble in water. However, calculating the scattered wave momentum, or equivalently calculating the Lorentz force based on the polarization with respect to the background $\bar{P} = (\epsilon_p - \epsilon_b)\bar{E}$, shows that the air bubble is actually pushed out of

the high intensity beam axis as observed in experiment. Second, the validation of a 2-D model with trapping experiments allows us to model binding more efficiently with infinite cylinders subject to an in-plane incidence. Optical binding in 2-D will be discussed in Chapter 5.

In the case of an absorbing particle, the contributions from $< \bar{F}_c >$ and $< \bar{F}_b >$, which is shown have and equivalent representation in momentum conservation, sum to give the total force on the particle. The fact that the total radiation pressure on an absorbing particle may be less than that of a similar lossless particle, differs from the conventional wisdom that absorption forces added to scattering forces must increase the overall radiation pressure on a particle; an assumption taken from experiments and theory involving lossy particles in the Rayleigh regime [29]. This result was confirmed for the physically realistic geometry of an absorbing Mie sphere. The theory presented here is thus fundamental to the understanding of optical momentum transfer in lossy media and necessary for modeling in applications of trapping, binding, and guiding of Mie particles.

Chapter 5

Optical Binding

Optical manipulation of dielectric particles has been accomplished using focused laser beams since the pioneering work by Ashkin [12]. The effects of levitation and trapping have been described by the scattering force and the gradient force, respectively. Optical binding was reported as a third optical force [32] and has been used to create arrays of particles termed optical matter [33]. The formation of two-dimensional optical arrays [94, ?, ?] and one-dimensional optical arrays [103, ?, ?, ?] has been verified by various groups. The description of optical manipulation based on scattering, gradient, and binding forces is an over simplification in many cases, but it is useful for developing some intuition. Rigorous modeling of optical array formation requires the computation of the total electric and magnetic fields within the particles or within the near field of the particles. The exact solution of electromagnetic scattering from an aggregate of spheres is known [104] and was recently applied to study photonic clusters formed by dielectric spheres [105]. However, the complexity of computing the exact field solution of a collection of Mie spheres hinders the ability to develop a fundamental understanding of the underlying optical binding forces and limits the number of particles that can be studied in dynamic systems. Typically, a system of particles is studied by applying an approximate solution, such as the

Rayleigh approximation [34, ?]. In this chapter, an alternate approach to modeling applications of optical binding is taken; exact field solutions are applied to simplified geometric representations of particles. That is, multiple slabs and cylinders are used to study optical binding in one dimension and two dimensions, respectively. Since all fields are time-harmonic in the analysis of optical binding, complex fields are used and all forces are cycle-averaged with the brackets $< \cdot >$ dropped to simplify the notation in this chapter.

5.1 Optical binding in one dimension

The optical binding force is due to interference of multiple waves, which result because of the boundary conditions imposed upon the electromagnetic fields. The optical binding between two slabs was already mentioned in Chapter 2. The Lorentz force density in a half-wave slab shown in Fig. 2-3 (b) can be thought of the binding interaction between two quarter-wave slabs. In this viewpoint, the quarter-wave slab on the left-hand side and the quarter-wave slab on the right-hand side are being pulled apart by equal but opposite forces. It is within this context that the optical binding of equivalent dielectric slabs is studied here.

The geometry of the problem to be studied is shown in Fig. 5-1. The two dielectric slabs of permittivity ϵ and thickness d are separated by a distance δ. A plane wave of unit amplitude is incident from free space in the $\hat{z}$ direction. The field solution is known for an arbitrary number of isotropic, homogeneous layers, each of arbitrary thickness and constitutive parameters [39]. The fields in each region can be thought of as an infinite number of waves being multiply scattered from the boundaries. However, the solution can be written simply as a superposition of a forward $+\hat{z}$ propagating wave and backward $-\hat{z}$ propagating wave within each region. The amplitudes of these waves are determined by writing the boundary conditions as a vector equation and inverting the matrix to determine the unknown coefficients. Therefore, the unique

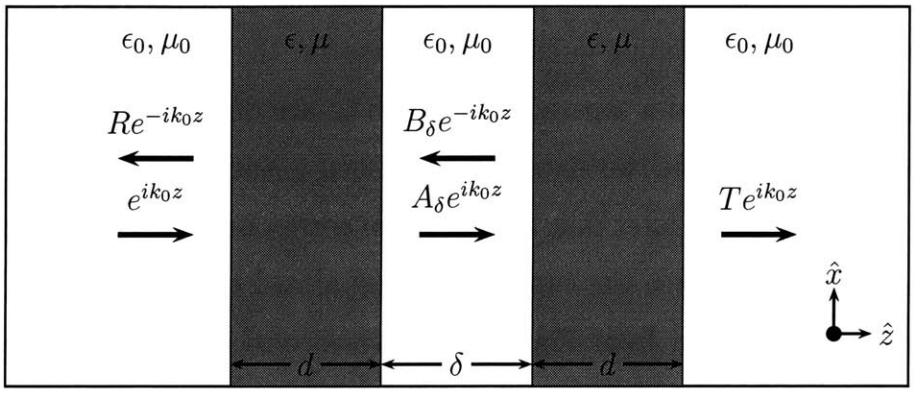

Figure 5-1: The fields resulting from two identical slabs in free space under normal incidence are found by matching the boundary conditions with counter propagating plane wave solutions in each region. The unit amplitude incident electric field produces a reflected wave Re^{-ik_0z}, a transmitted wave Te^{ik_0z}, and counter propagating waves $A_\delta e^{ik_0z}$ and $B_\delta e^{-ik_0z}$ between the slabs. The complex coefficients R, T, A_δ, and B_δ are determined from the boundary conditions. The incident electric field is $\bar{E} = \hat{x}e^{ik_0z}$, where $k_0 = \omega\sqrt{\mu_0\epsilon_0}$.

solution for the electric and magnetic fields in each region is known. The waves considered here are limited to normal incidence, so the forces exerted upon the slabs are in the $\pm\hat{z}$ directions.

It is interesting to study the distribution of force density in the two slabs as the separation δ is varied. Here, we return to the previous case of two dielectric slabs with $d = \lambda/4$ and $\epsilon = 4\epsilon_0$, so that $\lambda_0 = 2\lambda$. When $\delta = 0$, the force density is given in Fig. 2-3 (b). For other values of separation, the force density is plotted in Fig. 5-2. The radiation pressure on each slab is the integration of the Lorentz force density. For example, the pressure on the left-hand slab is

$$F_L \equiv \frac{1}{2}\Re\left\{ \int_0^d dz \left[-i\omega(\epsilon - \epsilon_0)\bar{E} \times \mu_0 \bar{H}^*\right] \right\}. \tag{5.1}$$

The binding force is defined here by the $\hat{z}$ directed force $F_{bind} = F_R - F_L$, which is simply the force exerted upon the slab on the right minus the force exerted upon the slab on the left. In Fig 5-2 (a), the total force on the two slabs are equal in magnitude and direction, thus the binding force is zero. However, the force distributions in each slab, which results due to a separation of $0.096\lambda_0$, are quite different as evident in the figure. In this case, the two slabs will be pushed in the $+\hat{z}$ direction by the same amount. It will be shown later that this situation corresponds to a stable equilibrium in the binding force. When the two slabs are separated by $\lambda_0/4$, the binding force is negative as determined from Fig. 5-2 (b), which indicates that the slab on the left-hand side will be pushed toward the slab on the right-hand side while both are subject to a net $+\hat{z}$ directed force. The force distributions shown in Fig. 5-2 (c) and Fig. 5-2 (d) are equivalent to the force distributions in Fig. 2-3 (b) and Fig 5-2 (a), respectively, except for the added separation of $\lambda_0/2$ in each case. From this analysis, we would expect that the binding between two slabs is a periodic function with respect to separation distance with a period of $\lambda_0/2$.

Next, the binding force is studied to demonstrate phenomena such as optical trapping based on binding forces. Using the more efficient momentum conservation approach, the cycle-average forces exerted upon the left slab and upon the right slab are

$$F_L = \frac{\epsilon_0}{2}(1 + |R|^2 - |A_\delta|^2 - |B_\delta|^2) \tag{5.2a}$$

$$F_R = \frac{\epsilon_0}{2}(|A_\delta|^2 + |B_\delta|^2 - |T|^2). \tag{5.2b}$$

As before, the finding force

$$F_{bind} = \epsilon_0(|A_\delta|^2 + |B_\delta|^2) - \frac{\epsilon_0}{2}(1 + |R|^2 + |T|^2) \tag{5.3}$$

is the difference between the two forces such that a positive binding force indicates that the two slabs are being pushed apart. Energy conservation dictates that $|R|^2 +$

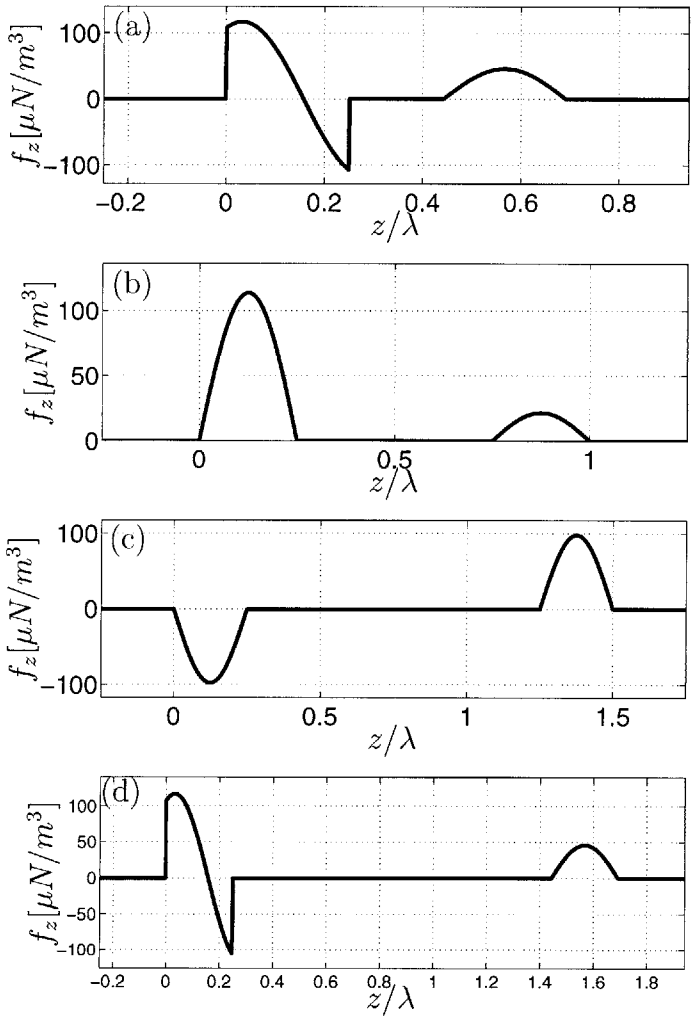

Figure 5-2: Force density distribution within two identical dielectric slabs ($\epsilon = 4\epsilon_0$) of thickness $d = \lambda/4$, where λ is the wavelength inside the slabs. The gap between the slabs is (a) $\delta = 0.096\lambda_0$, (b) $\delta = \lambda_0/4$, (c) $\delta = \lambda_0/2$, and (d) $\delta = 0.596\lambda$. The surrounding medium is free space, which corresponds to regions where both the curve and the slope of the curve are zero. The incident wave is $\bar{E}_i = \hat{x}e^{ik_0 z}$.

$|T|^2 = 1$, and the binding force reduces to

$$F_{bind} = \epsilon_0(|A_\delta|^2 + |B_\delta|^2 - 1). \tag{5.4}$$

Because the coefficients A_δ and B_δ are periodic with respect to the separation distance δ, the binding force given by (5.4) must also be periodic. This periodicity is seen to be $\lambda_0/2$ for all three cases in Fig. 5-3, which is in agreement with the previous conclusion drawn from Fig. 5-2. From Fig. 5-3 we can see a couple of trends with respect to the parameters. First, the binding force exerted upon quarter wave slabs at $\delta = m\pi/2$ $(m = 0, 1, \ldots)$ becomes very large as the permittivity increases. Thus, two quarter wave slabs brought in contact will be pushed apart, and slabs with larger permittivity will experience a larger separation force. However, the thin slabs $(d = 0.01\lambda_0)$ experience a negative binding force for $\delta = m\pi/2$. This means that two thin slabs are pulled together when touching. Second, the force on the right-hand slab approaches a constant and the force on the left-hand slab appears to be harmonic as the slab thickness approaches zero. This limiting case is analogous to the Rayleigh regime for spherical particles.

We first predicted optical trapping based on optical binding forces in two dimensions by analyzing a system of cylinders [6]. The analysis of cylinders is treated in the following section. Here, it is argued that a much simpler manifestation of this phenomenon occurs in one dimension. If we take the right-hand slab to be fixed and allow the left slab-hand to span z, we can see for all three cases in Fig. 5-3 that stable optical trapping occurs for the left-hand slab at values of δ were $F_L = 0$ and $\partial F_L/\partial\delta < 0$. Specifically, the thin slab $(d = 0.01\lambda)$ shown in Fig. 5-3 (c) is trapped at $\delta = 0.154 + m\lambda_0/2$, where again $m = 0, 1, 2, \ldots$. Thus, it is possible to trap a slab in 1-D using only binding forces. However, trapping in multiple dimensions requires the binding force from multiple fixed particles as will be shown in the following section.

Finally, we note that two identical small slabs brought in contact are pushed

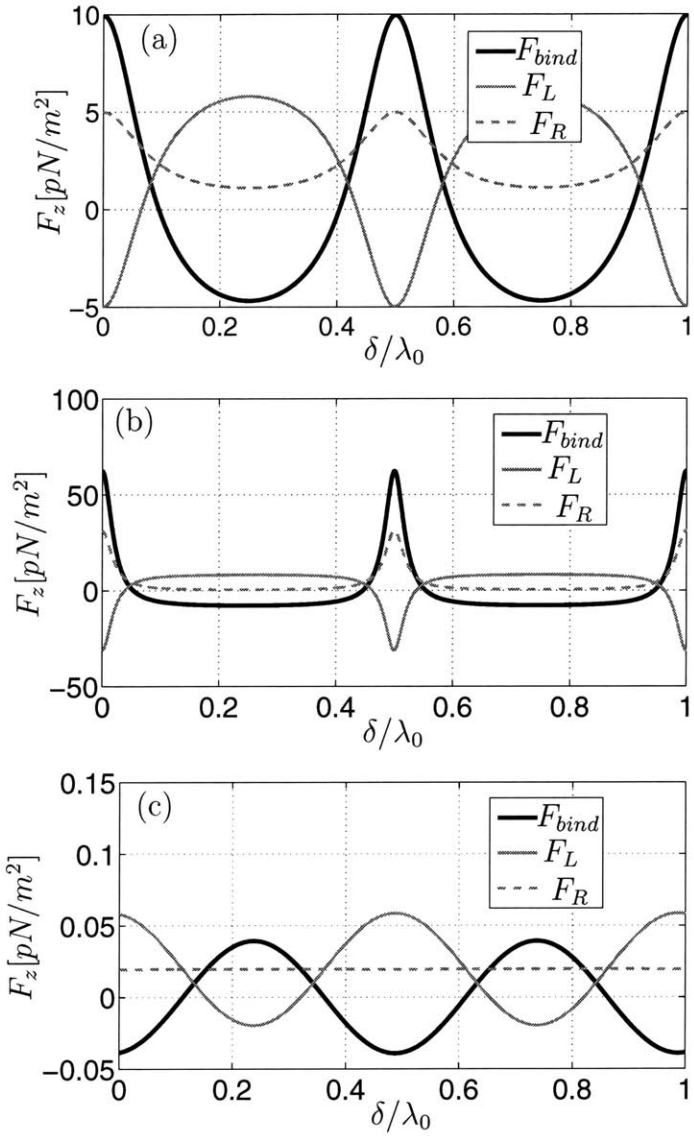

Figure 5-3: Binding force versus separation distance due to two identical dielectric slabs incident by a plane wave. The slabs are (a) quarter wave slabs $d = \lambda/4$ with $\epsilon = 4\epsilon_0$, (b) quarter wave slabs $d = \lambda/4$ with $\epsilon = 16\epsilon_0$, and (c) very thin slabs $d = 0.01\lambda$ with $\epsilon = 4\epsilon_0$, where λ is the wavelength inside the slabs. The separation distance δ is normalized by the free space wavelength $\lambda_0 = 2\lambda$. $F_{bind} = F_R - F_L$ is the binding force exerted upon the slabs, where F_R and F_L are the forces on the individual slabs on the right-hand side and left-hand side, respectively. The incident wave is $\bar{E}_i = \hat{x}e^{ik_0 z}$.

together, while larger slabs such as for $d = \lambda/4$ are pulled apart when touching. This observation is evident from Fig. 5-3 when $\delta = 0$. Here, this issue is studied in more detail. A straightforward analysis of the force density f_z inside a slab reveals that two slabs, each of thickness $\lambda/8$ will experience zero binding force when $\delta = 0$. This is evident in Fig. 5-4 which shows the binding force versus slab thickness for two slabs which are touching. Not only is it confirmed that slabs smaller than $\lambda/8$ will be bound to each other when brought together, but it is seen that there is a periodicity in this plot as well. Two identical slabs of thickness $d = \lambda/2$ experience zero binding force. Furthermore, slabs with thickness $d = \lambda/2 \pm \lambda/8$ will experience a negative (or zero) binding force when brought together. That is, we could expect two identical slabs in this size range can bind together with zero spacing. However, slabs in the range $d = \lambda/4 \pm \lambda/8$ will separate based on the positive sign of the binding force. This result may have implications in forming optical matter when it is desired to have little or no space between adjacent particles. However, a detailed study of multiple 2-D and 3-D particles have not been completed at this time.

5.2 Optical binding in two dimensions

The formation of two dimensional optical arrays of three dimensional particles has been realized in experiments where the motion is typically constrained in one dimension [94]. In this section, the optical binding in two dimensions is modeled by a collection of infinite cylinders. An exact theoretical model based on Mie theory is applied to compute the total fields due to an arbitrary number of 2-D dielectric cylinders subject to in plane incidence. The interactions between the particles are computed using the Foldy-Lax multiple scattering equations [106, ?]. The force on each particle is then computed by numerically integrating the line integral of the Maxwell stress tensor.

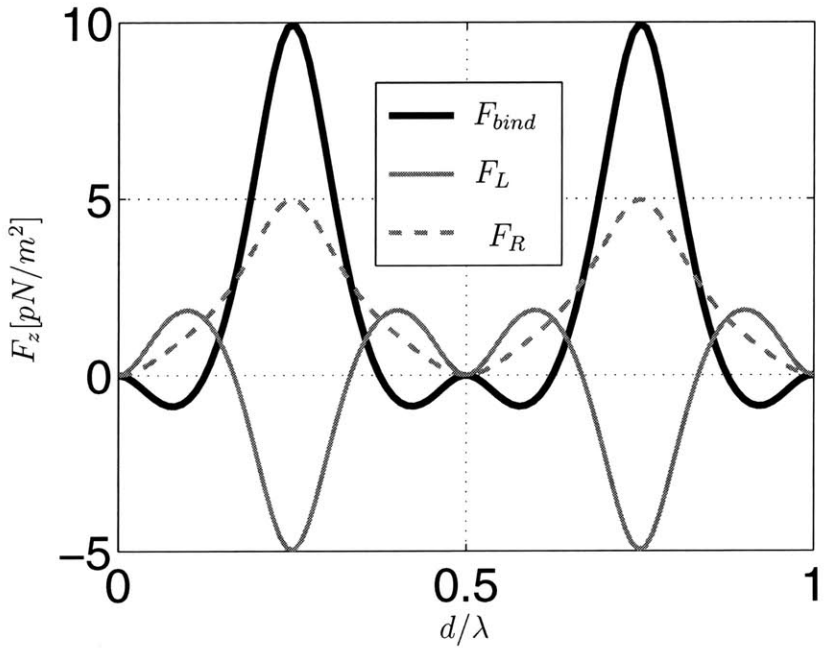

Figure 5-4: Binding force versus individual slab thickness d for two touching ($\delta = 0$) identical dielectric slabs ($\epsilon = 4\epsilon_0$) incident by a plane wave. $F_{bind} = F_R - F_L$ is the binding force exerted upon the slabs, where F_R and F_L are the forces on the individual slabs on the right-hand side and left-hand side, respectively. The incident wave is $\bar{E}_i = \hat{x}e^{ik_0 z}$.

5.2.1 Binding of 2-D particles in an in-plane field

The problem considered here consists of L infinitely long cylinders aligned parallel to the $\hat{z}$ axis incident by one or multiple $\hat{z}$ polarized plane waves. The field solution is given by the cylindrical wave expansions in Appendix B and the multiple scattering equations in Appendix E. First, we consider the two cylinders shown in Fig. 5-5. The two cylinders are separated by a distance x measured center-to-center and incident by a single plane wave propagating in the $\hat{y}$ direction. The $\hat{x}$ directed force exerted on the right-hand particle is shown in Fig. 5-6. Note that the $\hat{x}$ directed force on the left-hand particle is equal in magnitude and opposite in sign due to the symmetry of the problem. There is also a force in the $+\hat{y}$ direction on both particles (not shown, but to be discussed later). It can be seen from Fig. 5-6 that the binding force between the two particles is oscillatory. This force also decreases in magnitude with separation distance as expected. Thus, as with the slab, the array of two cylinders exhibits multi-stability in the equilibrium separation distance. These distances correspond to points in Fig. 5-6 with zero force and negative slope. Fig. 5-7 shows a similar plot for a small particle ($a = 0.015\lambda_0$). The interesting feature of this plot is that the particles experience a negative binding force when the two particles are close to each other, which contrasts the results for the larger particles in Fig. 5-6.

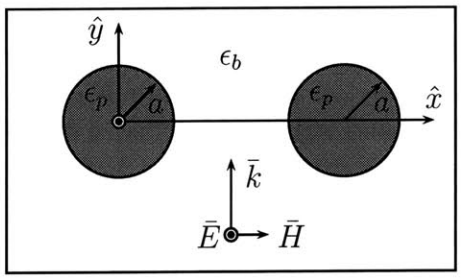

Figure 5-5: Two infinite cylinders of radius a are subject to an electromagnetic wave propagating in the $\hat{y}$ direction. The electric field is polarized parallel to the cylinder axis.

We are now in a position to simulate a system of multiple particles. Here, we reproduce part of the experimental conclusions of Ref. [94] within the limitation

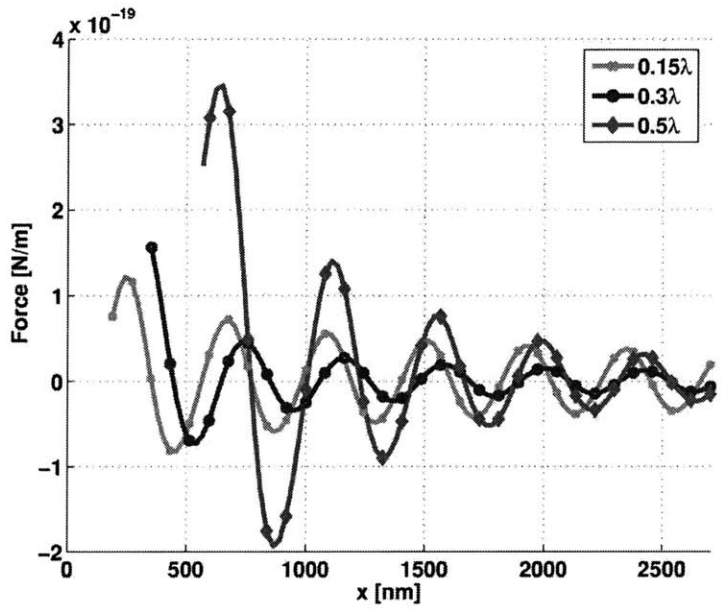

Figure 5-6: Force in the $\hat{x}$ direction as a function of the center-to-center distance between two particles. The plane wave $\bar{E} = \hat{z}e^{iky}$ is incident from water $\epsilon_b = 1.69\epsilon_0$ with free space wavelength $\lambda_0 = 546\ nm$. The radii of the polystyrene cylinders $\epsilon_p = 2.56\epsilon_0$ are indicated by the label. The computation was performed with $N = 10$ in the summation of cylindrical modes. © 2006 Optical Society of America, Inc. [5]

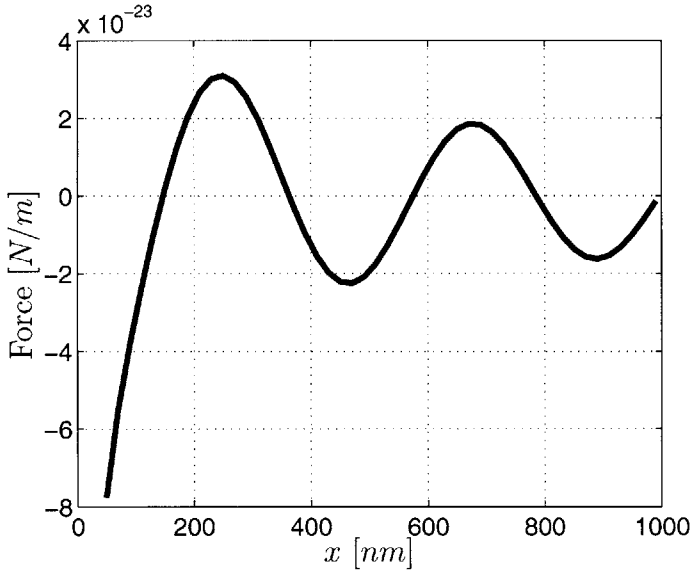

Figure 5-7: Force in the $\hat{x}$ direction as a function of the center-to-center distance between two particles. The plane wave $\bar{E} = \hat{z}e^{iky}$ is incident from water $\epsilon_b = 1.69\epsilon_0$ with free space wavelength $\lambda_0 = 546\ nm$. The radius of the polystyrene cylinder $\epsilon_p = 2.56\epsilon_0$ is $a = 0.015\lambda_0$. The computation was performed with $N = 10$ in the summation of cylindrical modes.

of in-plane incident plane waves. Twenty polystyrene particles ($\epsilon_p = 2.56\epsilon_0$) are placed randomly in water $\epsilon = 1.69\epsilon_0$ and subject to three plane waves of wavelength $\lambda_0 = 546\ nm$ incident at angles $[\pi/2, 7\pi/6, 11\pi/6]$. The particles of radius $a = 0.15\lambda_0$ are placed in the positions given in Table 5.1 and shown in Fig. 5-8 along with the incident electric field interference pattern. The final positions given in Table 5.1 are deduced by an iterative process. At each iteration, the force on the particle is computed from the total fields and the particle is moved just a fraction of a particle radius. This process is repeated until the position of all the particles approaches a constant value. It should be emphasized that the motion of the particles resulting from this iterative process is not derived from the equations of motion. Instead, this iterative process is merely a tool to estimate the final trapping positions for the particles in a liquid such as water, where strong damping is present. It has since been confirmed that the final positions are the same when the equations of motions are implemented to model the dynamics. While the particles tend to trap near the high intensity regions as with a single particle, it is evident that the binding forces resulting from all interactions effects the final trapping positions. Note that the total fields resulting from the final field locations are also shown in Fig. 5-8 (lower left). From this plot, it can be seen that indeed the particles align with the high intensity regions of the total fields resulting from all interactions. Also shown in are the final position for another set of random initial positions). These positions being different from the final positions given in the previous example demonstrates that the final positions depend upon both the incident waves and the initial positions of the particles.

5.2.2 Optical trapping based on optical binding forces

Previously, it was shown that a slab can be trapped by using the binding force resulting from a second stationary slab. In this section, we show that the binding force can be used to create a stable trap in two dimensions. The configuration of the problem

Table 5.1: Initial positions (x_i, y_i) and final positions (x_f, y_f) of 20 particles in a three plane wave interference pattern

x_i (nm)	y_i (nm)	x_f (nm)	y_f (nm)
-148.91	-59.30	-200.08	-120.94
-377.76	-388.95	-410.69	-533.34
296.79	-380.12	179.12	-356.27
30.78	-355.74	-7.45	-486.75
-106.53	396.91	18.50	454.02
286.33	-85.47	398.75	16.19
278.84	301.18	219.68	374.49
-272.76	179.49	-427.16	245.14
-276.50	362.89	-219.12	346.56
279.25	91.55	204.00	111.49
-287.76	-231.91	-388.75	-230.97
42.83	17.06	-5.79	-2.15
70.09	231.64	-7.01	235.09
-310.92	3.13	-409.60	19.53
-151.11	-349.56	-198.72	-402.18
10.59	-162.72	2.95	-247.57
-101.12	118.56	-206.37	118.08
388.51	-224.98	416.51	-199.41
168.19	-235.86	193.02	-125.97
141.00	397.59	249.79	633.45

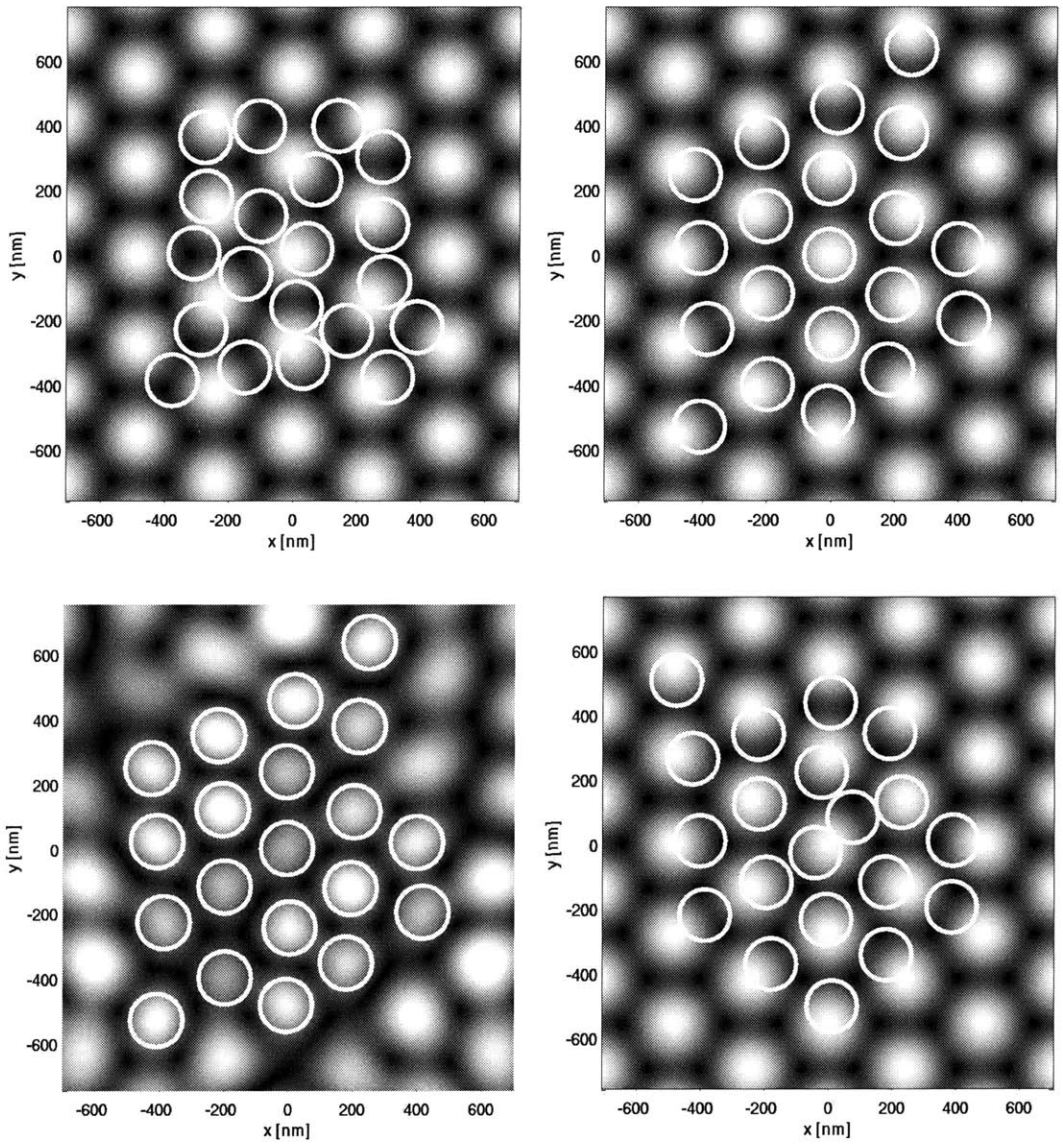

Figure 5-8: Positions of 20 dielectric cylinders overlayed on the absolute value of the (0 to 3 V/m). Initial random initial position in a three plane wave interference pattern (top left). Organized final positions due to the incident interference pattern shown in the background (top right). The positions are the same but with the total field shown (bottom left). Organized final positions corresponding to another set of initial positions different from the previous case (bottom right). The parameters are $\lambda_0 = 546\ nm$, $\epsilon_p = 2.56\epsilon_0$, $\epsilon_b = 1.69\epsilon_0$, and $a = 0.15\lambda_0$. © 2006 Optical Society of America, Inc. [5]

is similar to the one studied previously, where it was shown in Fig. 5-6 that the x directed binding force (denoted F_x) can take on both negative and positive values. A similar geometry is considered in Fig. 5-9 (a). In this configuration the force on the right-hand particle also has a positive $\hat{y}$ directed force (denoted F_y). In order to have stable two dimensional trapping of the particle on the right hand side, it is necessary to reverse the direction of F_y. In this regard, we consider one or multiple polystyrene particles of radius 10 nm which may be fixed in position along the y axis as shown in Fig. 5-9 (b). It is evident that with as few as three fixed particles, a negative F_y is achieved for the identical particle which spans the x axis. For proof of concept, we choose nine particles aligned along the y axis as shown in Fig. 5-9 (c). Note that we can also achieve $F_y < 0$ for nine particles aligned along the negative x axis as shown in Fig. 5-9 (d), although we will from now on consider only the vertically aligned cylinders of Fig. 5-9 (c).

The forces in Fig. 5-9 (c) are symmetric in x and that the first minimum has a magnitude comparable to the first maximum ($F_y \approx -1.1 \cdot 10^{-22}\ N/m$ at $x \approx 155nm$ and $F_y \approx +1.5 \cdot 10^{-22}\ N/m$ at $x \approx 430nm$). In order to achieve the two dimensional trap, we consider the symmetric set of fixed particles shown in Fig. 5-10. The second set of nine vertically aligned particles are placed at $x = 595\ nm$. The location of the second set of nine vertical particles was optimized such that the independent forces tend to cancel each other by superposing their respective minima and maxima. To optimize the location of the particles, an inverse problem was defined based on the multi-scattering equations presented in Appendix E. As a starting point, the F_y and F_x resulting independently from two sets of vertically aligned particles was used to determine the approximate location of a stable trap in both x and y. Although the reasoning based on the independent forces from the two vertical sets is not exact, it gives a good guess ($\approx 585\ nm$) of the initial positions to be used in the optimization. The optimization was run with 19 identical particles (18 are fixed and 1 spans the plane). The force field on the particle allowed to span the plane is plotted using the

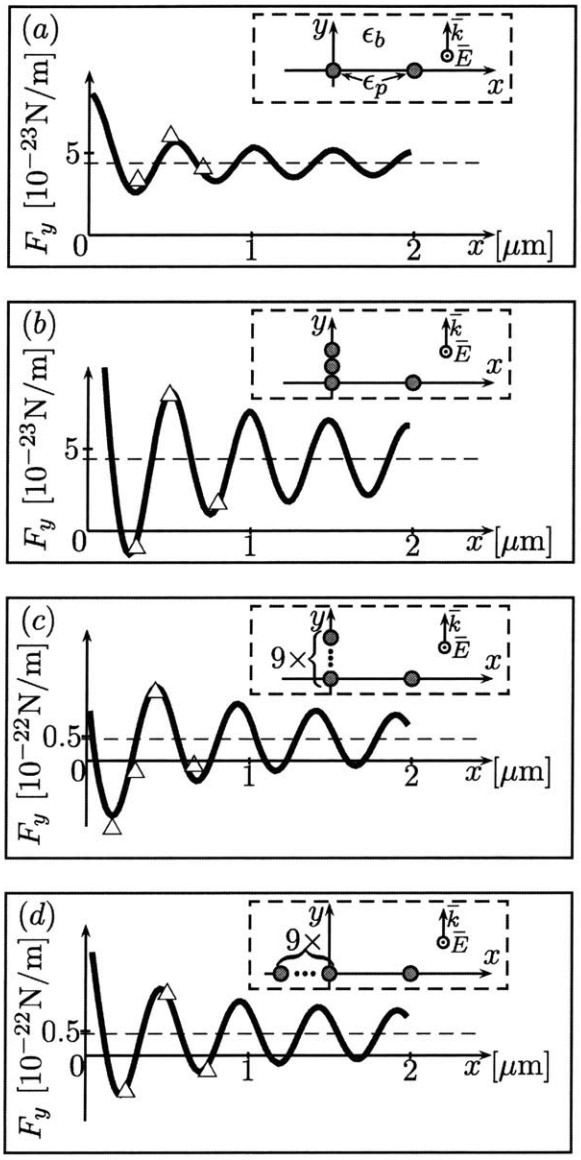

Figure 5-9: Binding force in the $\hat{y}$-direction on a particle to the right as a function of its position along the $\hat{x}$-axis due to a single plane wave $\bar{E} = \hat{z}e^{iky}$ with free space wavelength $\lambda_0 = 632.8\ nm$. The four subplots correspond to different arrangements of the fixed particles to the left.: (a) single particle, (b) three particles aligned in $\hat{y}$, (c) nine particles aligned in $\hat{y}$, (d) and nine particles aligned in $\hat{x}$. All particles have a permittivity $\epsilon_p = 2.25\epsilon_0$, and have a radius of 10 nm. The particles to the left are separated edge-to-edge by 1 nm. The dashed curve indicates the force on a single particle ($F_y \approx 4.36 \cdot 10^{-23}\ N/m$). The triangles represent calculations based on the Lorentz force density integrated over the fields inside the particle obtained from the commercial package CST Microwave Studio ®. © 2006 The American Physical Society.

optimized structure in Fig. 5-10. In each plot, each arrow represents the direction and the relative magnitude of the force on the free particle located at the base of the arrow. Thus, a stable trap is seen to exist at $(x, y) = (297.5nm, 0.4nm)$. Furthermore, this trap remains when multiple particles (up to four shown) occupy the trap already. In fact, our analysis of the potential energy reveals that the addition of up to four particles in the trap strengthens the potential well created by the optical binding forces. Thus, we have demonstrated the concept that optical binding forces can indeed create a stable optical trap.

5.2.3 Sorting of particles using optical binding forces

The ability to sort mesoscopic dielectric particles is of interest to scientist who wish to separate solutions of mono-dispersed particles from poly-dispersed ones. In this regard, sorting based on a combination of a fluid drag and optical forces has been demonstrated as a viable technique for discriminating dielectric particles based on size and index of refraction [107, 108]. Here, we demonstrate proof of concept for particle sorting based solely on the optical binding forces between the free particles and a diffractive structure. Thus, the sorting mechanism presented here is fundamentally different in that it does not rely upon fluid drag.

The configuration of the system is similar to the one studied in the previous section and is shown in Fig. 5-11. An electromagnetic wave of unit amplitude and wavelength 632.8 nm propagating in the $\hat{y}$ direction is incident upon ten fixed particles aligned along the y axis and one free particle is free to move in the xy plane. The configuration can be viewed as a diffractive structure that produces the field gradient shown in the background. In this regard, one may argue that propagation channels exists along the regions of high intensity due simply to the gradient force and the scattering force. However, we model the diffractive structure as a series of particles so that all interactions can be taken into account analytically. This is necessary since the field gradient shown is altered by the presence of the free particle. Thus, optical

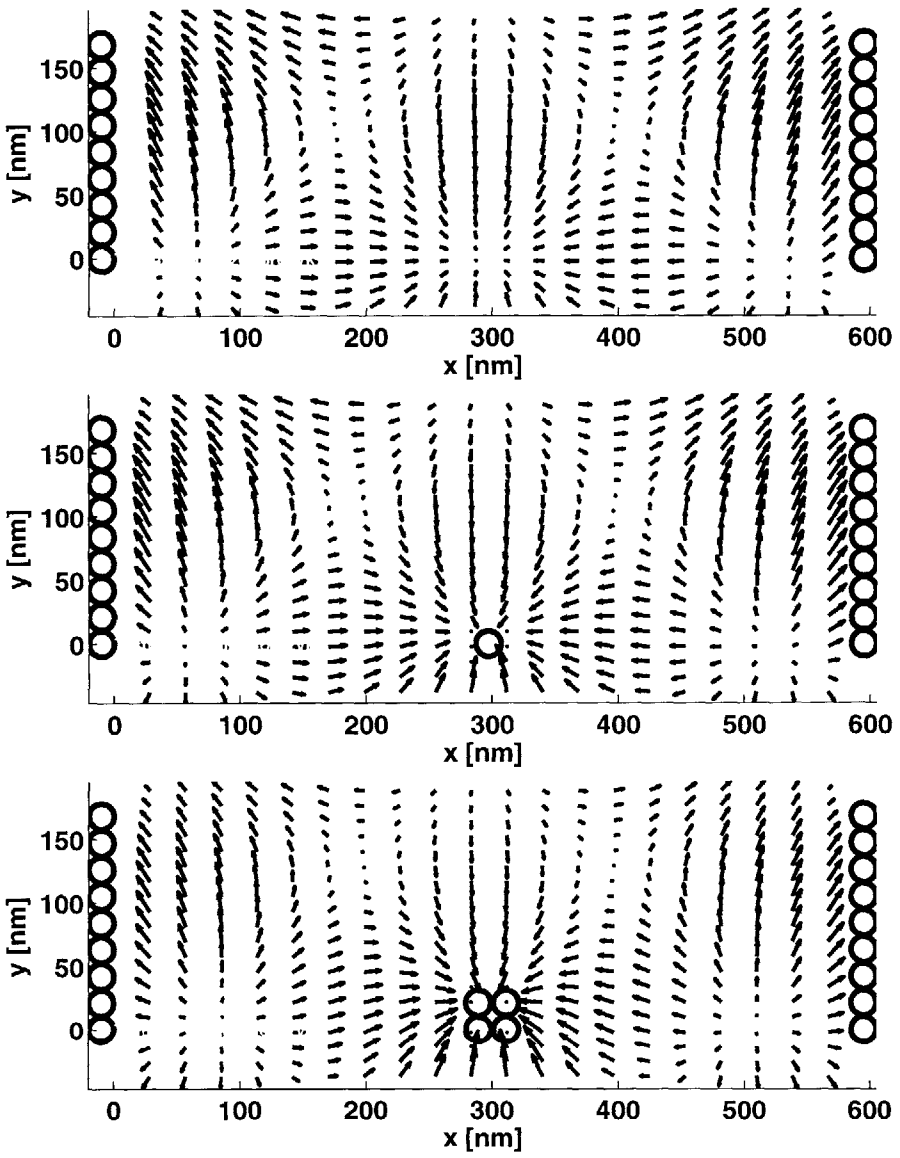

Figure 5-10: Force on a free particle in the presence of two vertical walls of particles separated by 595 nm and (a) no trapped particle, (b) a single trapped particle, (c) four trapped particles, all clustered around the trapping position $(x, y) = (297.5, 0.4)$ nm. The other parameters are identical to those of Fig. 5-9. © 2006 The American Physical Society [6].

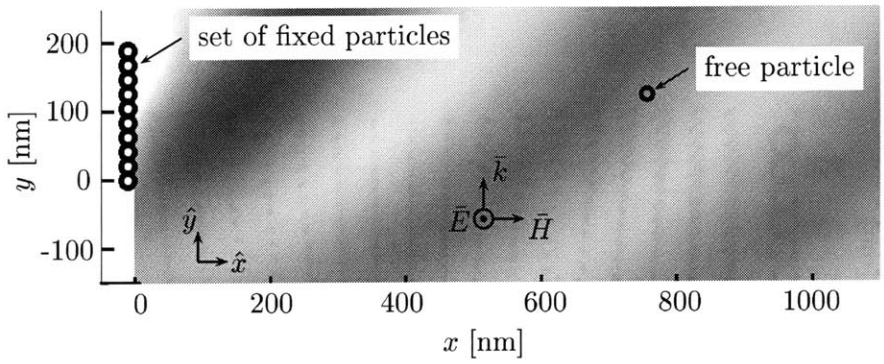

Figure 5-11: Configuration proposed for guiding and sorting consisting of an incident plane wave propagating along $\hat{y}$. A series of ten fixed cylinders is used to guide and sort one particle which is free to move in the $x-y$ plane. The force results from the interaction between the free particle and the fixed particles responsible for the field intensity shown in the background. © 2006 Optical Society of America, Inc. [7]

binding forces contribute to guiding and sorting properties of the structure.

The operation of the structure can be viewed as a "black box" and is demonstrated by the trajectories in Fig. 5-12. Free particles are allowed to enter the region of space at any x position along the line defined by $y \approx -100\ nm$. We then are interested in the exit positions along the line $y \approx 300$. To deduce the exit positions, we follow the iterative procedure previously applied: the particle is moved a small amount based on the direction and the magnitude of the cycle averaged force, and this process is repeated until an exit position is reached. The paths are shown by the lines with starting positions every 20 nm along x. In the simulation shown, 10 nm particles propagate along channels and exit the guiding structure at A or B, denoted by the index $l = 1$ or $l = 2$, respectively.

The sorting ability is studied by defining the relative displacement $x_{rel}^{(l)}(a) = x_0^{(l)}(a) - x_0^{(l)}(a = 5nm)$ where $x_0^{(l)}(a)$ is the size-dependent exit position and $x_0^{(l)}(a = 5nm)$ is the nominal exit position for a particle of radius $a = 5nm$. Three data sets are presented in Fig. 5-13 corresponding to the nominal (reference) exit positions $x_0^{(1)}(a = 5nm) = 534nm$ and $x_0^{(2)}(a = 5nm) = 1032nm$ for a water background

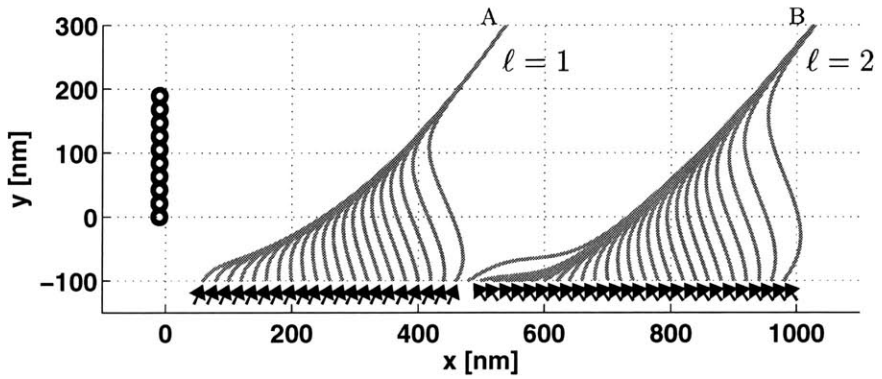

Figure 5-12: Propagation channels of a free cylindrical particle due to the interaction with the guiding and sorting configuration of Fig. 5-11. The starting points for the particle with $\epsilon_p = 2.56\epsilon_0$ and radius $a = 10\ nm$ are located at various x positions (shown at 20 nm intervals) for $y = -100\ nm$. The trajectory of the free particle is traced by computing the force and displacing the particle accordingly. © 2006 Optical Society of America, Inc. [7]

($\epsilon_b = 1.69\epsilon_0$) and $x_0^{(l)}(a = 5nm) = 659nm$ for free space background ($\epsilon_b = \epsilon_0$). It can be seen that the larger particles have a larger displacement away from the reference position (negative displacement indicates shifting to the left). The unique correspondence between position and size for a given configuration is the key feature by which passive sorting is possible. This uniqueness in the exit position is a direct result of the binding force since the propagation channel differs from the field gradient of Fig. 5-11 by virtue of binding forces between the fixed particles and the free particle.

5.3 Discussion

In this chapter, the forces on a collection of 1-D particles (slabs) and 2-D particles (cylinders) have been calculated without the usual approximations on particle size, permittivity, or separation. Because of this, the optical forces based on scattering, trapping, and binding have not been calculated as separate quantities, rather the electrodynamics of the system have been deduced from application of the Lorentz force density directly or by conservation of momentum via the Maxwell stress tensor.

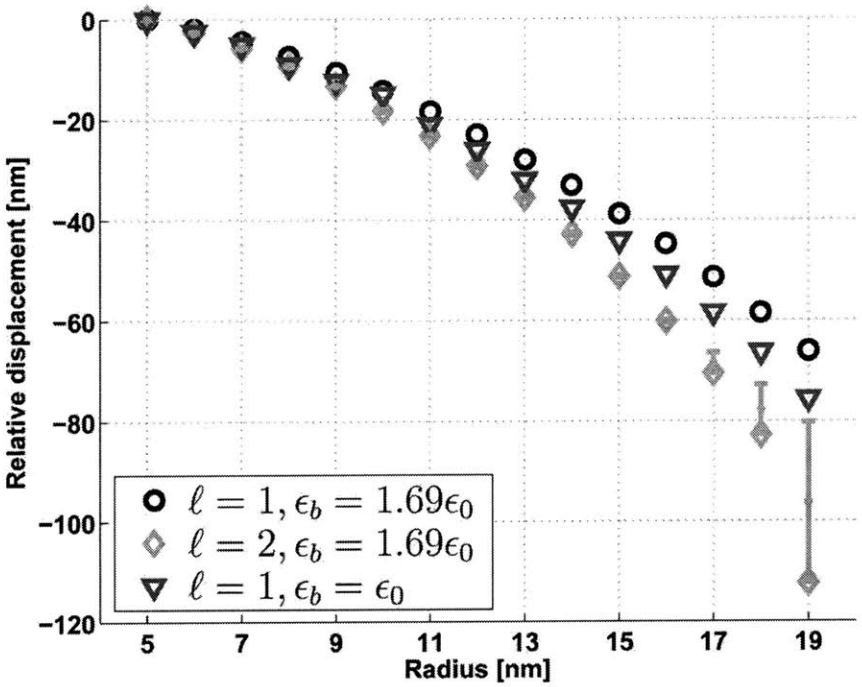

Figure 5-13: Relative exit position of the particle for various sizes and permittivity. The absolute reference positions are $x_0^{(1)}(a = 5nm) = 534nm$ and $x_0^{(2)}(a = 5nm) = 1032nm$ for $\epsilon_b = 1.69\epsilon_0$ and $x_0^{(1)}(a = 5nm) = 659nm$ for $\epsilon_b = \epsilon_0$. The error bars (not shown for the case of $\epsilon_b = \epsilon_0$ for clarity) illustrate the drift in positions of a minority of particles whose starting positions are toward the right edge of the right- and left-pointing arrows in Fig. 5-13 (close to 460 nm for $l = 1$ and close to 990 nm for $l = 2$. © 2006 Optical Society of America, Inc. [7]

However, we have shown that the terms "trapping force" and "binding force" are useful in a qualitative description of the optical manipulation of dielectric particles.

The results contained herein represent the first analysis of optical binding of slabs. Two identical lossless dielectric slabs were studied to reduce the optical binding problem to a simple one dimensional study of interference patterns. In this regard, the Lorentz force density, which exists everywhere inside the material once the fields are present, is distributed within the slabs according to the interference pattern of counter propagating waves. Thus, the details of the direction of binding force and the location of stable equilibria depend upon the standing waves both inside the slabs and outside the slabs. Therefore, it should not be surprising that the binding force between two slabs in free space is periodic with separation distance δ with a period which depends upon the free space wavelength λ_0 (or the wavelength of the background medium). The period of the function $F_{bind}(\delta)$ is $\lambda_0/2$ because the "round trip" distance between two slabs separated by $m\lambda_0/2$ is $m\lambda_0$, which provides a phase of $2k_0\delta = 2m\pi$ since $k_0 = 2\pi/\lambda_0$.

An exact method to compute the optical forces within a system of multiple Mie particles has also been presented. For the sake of simplicity, the particles are taken to be lossless dielectric cylinders, which is not a sever limitation since apart from the depolarization effects, most of the phenomena observed in two-dimensions can be generalized to three-dimensions. This model represents a step forward in the understanding of optical binding and the formation of optical matter, particularly where large particles are manipulated. Using this method, three systems have been studied in two dimensions; a collection of free dielectric particles, a new trapping regime based on optical binding forces, and passive guiding and sorting of dielectric particles with optical binding forces. These three studies demonstrate applications of optical binding via two dimensional simulations. Each system provides evidence of the effect of binding forces, which were calculated here from the general theory of optical momentum transfer, not from separate approximations for scattering, trapping, and

binding forces.

It should be noted that each of these systems required the computation of fields in a region of many particles surrounded by dielectric medium. Furthermore, the concept of electromagnetic wave momentum presented in previous chapters was employed to deduce the effective momentum transferred to each particle. Without this approach, the simulation would require the computation of force everywhere inside the particle and the background medium as well as the characterization of mechanical interaction between the background medium and the particles. Such a computationally expensive procedure would severely limit the ability to simulate optical binding experiments involving multiple particles suspended in a background medium such as water.

Chapter 6

Conclusions

This thesis presents a self-consistent formulation for efficiently modeling optical momentum transfer to macroscopic media. The formulation is based on the classical electromagnetic wave theory applied to monochromatic waves propagating in linear, isotropic, and stationary media. The results contained herein reconcile two methods for calculating the cycle-average force; the direct application of the Lorentz force density to media, which has been in vogue with researchers over the past few years, and application of momentum conservation theorems via the Maxwell stress tensor formalism, a topic which has been debated for most of the past century. The formulation is shown to be valid for a wide range of dielectric and magnetic media exhibiting temporal dispersion and loss. This theory is shown to be consistent with relevant experimental observations of momentum transfer to media and is applied to model optical manipulation of one or multiple particles in a laser field.

6.1 Conceptual conclusions of theoretical work

A number of conceptual conclusions can be deduced from the theoretical work presented in this thesis. Thus, a better fundamental understanding of electrodynamics

accompanies the ability to model optical trapping and binding experiments.

Two approaches were equivalently applied to various problems. The divergence of the Maxwell stress tensor relies on the conservation of momentum to deduce the forces on a material. On the other hand, the Lorentz force density states that the forces exist everywhere inside the matter once the fields are present. For example, the pressure on a lossless slab can be viewed as resulting from momentum changes at the two boundaries, or the pressure can be viewed as originating from the standing wave patterns inside the slab. In all cases studied herein, however, the prediction of experimental observable quantities are identical. Furthermore, the conceptual problem of the radiation attraction of a lossless dielectric interface has been reconciled in favor of the results derived by Daly and Gruenberg [61]. Reconciliation has also been shown for multiple examples of particles subject to multiple electromagnetic waves. These results have been published in *Optics Express* [1] and the *Journal of Electromagnetic Waves and Applications* [3], and they were presented at the 2006 Progress in Electromagnetics Research Symposium session "Recent advances in optical trapping and binding" organized by Professor Jean-Marc Fournier and Dr. Tomasz M. Grzegorczyk [109].

The momentum transfer to media has been separated into an adiabatic process and a non-adiabatic process. These processes are derived from the Lorentz force density exerted upon bound currents and charges and upon free currents, respectively. This separation was shown to be very useful in modeling various experimental observations of electromagnetic momentum transfer due to absorption in polarizable media. It is concluded that the direct dependence of absorbed momentum on the refractive index holds for both dielectric and magnetic media. These conclusions remain valid for temporally dispersive media. Thus, in the case where the index of refraction is negative, free currents are pulled toward the incident wave as the wave attenuates inside the material. This result is in agreement the reversal of radiation pressure predicted by Veselago [82]. This viewpoint of electromagnetic wave momentum is generalized

to model electromagnetic momentum transfer in lossless systems such as reflections from submerged mirrors and optical manipulation of mesoscopic particles in a background medium. In this regard, the electromagnetic wave momentum, which contains contributions from the electromagnetic fields and the response of the material, can be applied to predict observations in a wide variety of problems. We may conclude that the theory presented here attaches fundamental physical meaning to Snell's law; the reflected and transmitted wave vectors ensure conservation of the momentum component which is parallel to the boundary. Likewise, the magnitudes of the reflected and transmitted waves ensure conservation of wave energy at the interface. This assertion ensures that no sheering force exists due to the reflection and transmission of an electromagnetic wave at an interface. The theory is applied to predict a decrease in optical momentum transfer to Mie particles due to absorption, which contrasts the common intuition based on the scattering and absorption by Rayleigh particles. These results have been published in the *Physical Review Letters* [4] and the *Physical Review A* [2].

Evidence of optical trapping and binding forces have been predicted in one dimension and two dimensions without approximation. Optical trapping of single particles subject to multiple waves and Gaussian beams can be modeled using Mie theory and the scattering of electromagnetic wave momentum computed from the divergence of the Maxwell stress tensor. Thus the formulation is not only exact, but computationally efficient both in computing the fields and deducing the forces. Optical binding was demonstrated in one dimension by studying the interaction of multiple plane waves incident by an electromagnetic waves. Modeling of multiple particles in an in-plane electromagnetic wave is based on an extension of Mie theory to cylindrical particles combined with the Foldy-Lax multiple scattering equations. Modeling the electrodynamics of a system of particles represents an advancement in the understanding of optical trapping and binding. Using this formulation, a new trapping regime based on optical binding forces has been demonstrated analytically. The pos-

sibility of serially guiding and sorting nanometer sized particles using optical binding forces is also demonstrated. These applications are derived without approximation or explicit separation of scattering, trapping, and binding forces. However, they do serve to demonstrate the effects of multiple particle interactions. These results have been published in the *Journal of the Optical Society of America A* [5], the *Physical Review Letters* [6], and *Optics Letters* [7], and they were presented at the 2006 Progress in Electromagnetics Research Symposium [110].

6.2 Future work

As with any thesis, the results presented here are incomplete. The theoretical modeling of optical manipulation and electromagnetic momentum could be carried out indefinitely. Through the course of this investigation, I have come across a number of interesting problems. However, one cannot hope to solve the entire universe within one Ph.D. program. In this section, I outline some avenues of future research that have come to my attention over the past couple of years. In addition, I give some thoughts on how such problems could be approached. However, I have also learned that my original intuition and approach are often times misleading at best, or simply wrong at worst. Thus, the research projects and proposed solution approaches listed here are merely suggestions based on untested ideas.

6.2.1 Optical trapping and binding of LHM particles

I have conducted an initial study of optical manipulation to lossless (noncausal) negative index particles, which is not included in this thesis. As expected, the radiation pressure on such particles, either modeled as infinite cylinders or spheres, depends only upon the refractive index of the background medium; a particle is pushed by the incident wave if the background index of refraction is positive and is pulled by the incident wave if the background is negative, regardless of the sign of the particle

refractive index. There is some question as to the direction of the gradient force, for example in a Gaussian beam or a three plane wave interference pattern. Initial investigation suggests that there may be polarization effects that would greatly influence the direction of the trapping force on negative index cylinders. Initial binding studies of negative index particles have not been carried out to my knowledge. All of the theory to conduct this academic investigation are contained within this thesis. However, it has not been completed at the time of this writing due to time constraints.

6.2.2 Development of an optical manipulation simulator

This thesis demonstrates how to efficiently model slabs, cylinders, and spheres subject to various optical incidences. As the field of optical manipulation matures, applications are being found in physics, biology, chemistry, and medicine [25–27]. So far, experiments and applications have been designed relying mostly on approximate formulas. The theory presented herein could be used to develop an efficient simulator for optical trapping and binding studies. The field solutions would fall into two categories: analytical solutions for canonical geometries and numerical solutions for arbitrary geometries. A user friendly interface could eventually lead to a commercially viable engineering design tool.

6.2.3 Optical momentum transfer to bianisotropic media

All of the results presented here assume isotropic media. Many materials in nature exhibit anisotropy, while a new class of metamaterials can be classified as bianisotropic [111]. To study electromagnetic momentum transfer to such metamaterials, it is necessary to have a model of bianisotropy in the force calculations. In this case, $\bar{D} = \bar{\bar{\epsilon}} \cdot \bar{E} + \bar{\bar{\xi}} \cdot \bar{H}$ and $\bar{B} = \bar{\bar{\mu}} \cdot \bar{H} + \bar{\bar{\zeta}} \cdot \bar{E}$. For simplicity, one could study arbitrary incidence upon a bianisotropic slab. Fortunately, the field solution already exists [89]. Also, the total pressure on the slab can be computed via they divergence of the free space Maxwell stress tensor once the fields are known. Then, to model the details of

momentum transfer, we would need to determine the contributions to $\bar{f}_c$ and $\bar{f}_b$. One possibility is using the lossless conditions [39], $\bar{\bar{\epsilon}} = \bar{\bar{\epsilon}}^\dagger$, $\bar{\bar{\mu}} = \bar{\bar{\mu}}^\dagger$, and $\bar{\bar{\xi}} = \bar{\bar{\zeta}}^\dagger$, to factor out the bound currents from the free currents in Maxwell's equations. Then, one could show that an equivalent separation can be made using a stress tensor formalism as was done in this thesis for isotropic material.

6.2.4 Electromagnetic wave momentum in moving media

In Chapter 3, the electromagnetic wave momentum was derived for a dispersive dielectric and magnetic material. However, the assumption of stationary material was placed on the derivation for simplicity. One could, however, apply the concept of virtual power to derive the form of the momentum flux density $\bar{\bar{T}}$ and the momentum density vector $\bar{G}$ from the accepted forms of the energy flux and energy density in the rest frame of the material. The prescription for the application of virtual power is given by Penfield and Haus [53]. We should expect that the derived quantities $\bar{\bar{T}}$ and $\bar{G}$ in the laboratory frame reduce to the quantities derived in Chapter 3 in the limit of material velocity approaches zero. This derivation is expected to involve a lot of tedious math, and the results, while providing a more complete solution, may not add to the understanding of optical manipulation.

6.2.5 Light pulses and the Abraham-Minkowski controversy

The momentum of electromagnetic waves has been debated by physicists by nearly a century. The issue of momentum flux due to an electromagnetic waves is now well understood. The electromagnetic wave momentum, which reduces to the Minkowski momentum in non-dispersive materials, consists of a contribution from the electromagnetic fields (Abraham momentum) and the response of the medium. Thus, the Abraham-Minkowski controversy for time-harmonic fields has been reduced to interpreting the contributions of field and matter [2, 21, 38, 65]. For a finite wave packet (electromagnetic pulse) the isolation of the momentum density vector from the stress

tensor is possible as discussed in Chapter 2. In this case, the force exerted on the media is interpreted according to the choice of momentum density vector $\bar{G}$, which results directly from the formulation of the Maxwell equations applied to separate field and material contributions. Scalora *et. al.* revisited this issue in 2006 by comparing the momentum transfer to a thick slab (*i.e.* thick compared to the incident light pulse) based on the assumption of Abraham or Minkowski forms of the momentum density vector [68]. The numerical results of that study show that the predicted pressure on a slab evolves differently in time depending upon which value for the momentum density vector is applied. The momentum transfer in this case occurs in one dimension with the incident pulse having a positive momentum. Application of the Minkowski (Abraham) momentum predicts that the slab will acquire a negative (positive) momentum while the wave packet is inside the slab. In all cases however, the total momentum transferred to the slab as $t \rightarrow \infty$ approaches the same value as expected. While the principal author and I agree that an experiment would provide a fundamental test of electromagnetic theory [72], I argue that resolution to the issue may not be out of reach for the theorist. The key issue is the direction of momentum acquired by the slab due to the interaction of the wave packet with the medium. One could apply an analysis similar to that of Daly and Gruenberg [61]. That is, solve the problem within the framework of moving media. Then, use energy relations to deduce the direction of the slab velocity. To my knowledge, this approach has not been applied to the problem of a slab incident by a finite pulse. A theoretical and/or experimental resolution to this problem would be a significant contribution to physics considering the long and controversial history of this topic. However, one should bear in mind that such a claim would also come under significant scrutiny.

Appendix A

Reflection and Transmission by a Slab

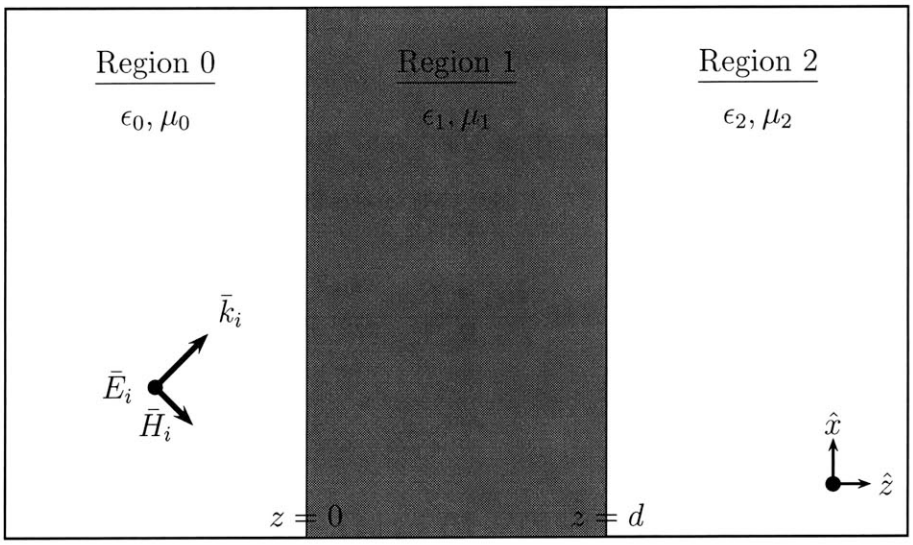

Figure A-1: TE plane wave incident upon an isotropic slab of thickness d.

The fields inside and outside an isotropic slab occupying the region $0 \leq z \leq d$ due to TE incidence are give below.

Region 0 ($z < 0$)

$$\bar{E}_0 = \hat{y}E_i(e^{ik_{0z}z} + Re^{-ik_{0z}z})e^{ik_x x} \tag{A.1}$$

$$\bar{H}_0 = \hat{x}\frac{-k_{0z}}{\omega\mu_0}E_i(e^{ik_{0z}z} - Re^{-ik_{0z}z})e^{ik_x x} + \hat{z}\frac{k_x}{\omega\mu_0}E_i(e^{ik_{0z}z} + Re^{-ik_{0z}z})e^{ik_x x} \tag{A.2}$$

Region 1 ($0 < z < d$)

$$\bar{E}_1 = \hat{y}(Ae^{ik_{1z}z} + Be^{-ik_{1z}z})e^{ik_x x} \tag{A.3}$$

$$\bar{H}_1 = \hat{x}\frac{-k_{1z}}{\omega\mu_1}(Ae^{ik_{1z}z} - Be^{-ik_{1z}z})e^{ik_x x} + \hat{z}\frac{k_x}{\omega\mu_1}(Ae^{ik_{1z}z} + Be^{-ik_{1z}z})e^{ik_x x} \tag{A.4}$$

Region 2 ($z > d$)

$$\bar{E}_2 = \hat{y}E_i T e^{ik_{2z}z}e^{ik_x x} \tag{A.5}$$

$$\bar{H}_2 = \hat{x}\left(\frac{-k_{2z}}{\omega\mu_2}\right)E_i T e^{ik_{2z}z}e^{ik_x x} + \hat{z}\left(\frac{k_x}{\omega\mu_2}\right)E_i T e^{ik_{2z}z}e^{ik_x x} \tag{A.6}$$

The unknown coefficients are found in the usual manor by applying the boundary conditions for tangential $\bar{E}$ and $\bar{H}$ at the two boundaries.

$$R = \frac{R_{01} + R_{12}e^{i2k_{1z}d}}{1 + R_{01}R_{12}e^{i2k_{1z}d}} \tag{A.7}$$

$$A = \frac{E_i}{2}\left[(1+R) + p_{10}(1-R)\right] \tag{A.8}$$

$$B = \frac{E_i}{2}\left[(1+R) - p_{10}(1-R)\right] \tag{A.9}$$

$$T = \frac{1}{E_i}\left(Ae^{ik_{1z}d} + Be^{-ik_{1z}d}\right)e^{-ik_{2z}d} \tag{A.10}$$

$$R_{01} = -R_{10} = \frac{1-p_{01}}{1+p_{01}} \qquad R_{12} = -R_{21} = \frac{1-p_{12}}{1+p_{12}} \tag{A.11}$$

$$p_{01} = \frac{1}{p_{10}} = \frac{\mu_0 k_{1z}}{\mu_1 k_{0z}} \qquad p_{12} = \frac{1}{p_{21}} = \frac{\mu_1 k_{2z}}{\mu_2 k_{1z}} \tag{A.12}$$

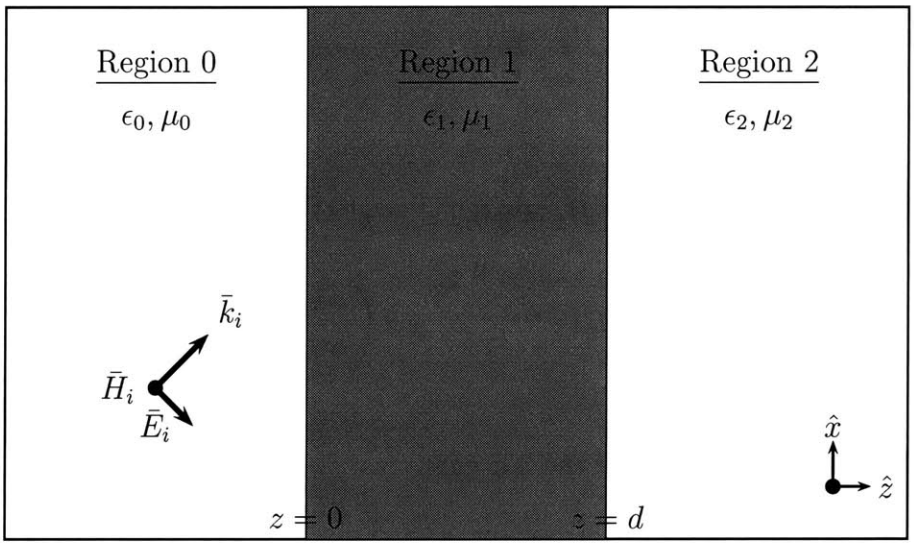

Figure A-2: TM plane wave incident upon an isotropic slab of thickness d.

The fields inside and outside an isotropic slab due to TM incidence are found by duality.

$$\bar{E} \to \bar{H}, \qquad \bar{H} \to -\bar{E}, \qquad \epsilon \leftrightarrow \mu \tag{A.13}$$

Incident Region ($z < 0$)

$$\bar{H}_0 = \hat{y} H_i (e^{ik_{0z}z} + Re^{-ik_{0z}z}) e^{ik_x x} \tag{A.14}$$

$$\bar{E}_0 = \hat{x} \frac{k_{0z}}{\omega \epsilon_0} H_i (e^{ik_{0z}z} - Re^{-ik_{0z}z}) e^{ik_x x} + \hat{z} \frac{-k_x}{\omega \epsilon_0} H_i (e^{ik_{0z}z} + Re^{-ik_{0z}z}) e^{ik_x x} \tag{A.15}$$

Slab Region $(0 < z < d)$

$$\bar{H}_1 = \hat{y}(Ae^{ik_{1z}z} + Be^{-ik_{1z}z})e^{ik_x x} \tag{A.16}$$

$$\bar{E}_1 = \hat{x}\frac{k_{1z}}{\omega\epsilon_1}(Ae^{ik_{1z}z} - Be^{-ik_{1z}z})e^{ik_x x} + \hat{z}\frac{-k_x}{\omega\epsilon_1}(Ae^{ik_{1z}z} + Be^{-ik_{1z}z})e^{ik_x x} \tag{A.17}$$

Transmitted Region $(z > d)$

$$\bar{H}_2 = \hat{y}H_i T e^{ik_{2z}z}e^{ik_x x} \tag{A.18}$$

$$\bar{E}_2 = \hat{x}\left(\frac{k_{2z}}{\omega\epsilon_2}\right)H_i T e^{ik_{2z}z}e^{ik_x x} + \hat{z}\left(\frac{-k_x}{\omega\epsilon_2}\right)H_i T e^{ik_{2z}z}e^{ik_x x} \tag{A.19}$$

The coefficients are also dual of the TE case.

$$R = \frac{R_{01} + R_{12}e^{i2k_{1z}d}}{1 + R_{01}R_{12}e^{i2k_{1z}d}} \tag{A.20}$$

$$A = \frac{E_i}{2}\left[(1+R) + p_{10}(1-R)\right] \tag{A.21}$$

$$B = \frac{E_i}{2}\left[(1+R) - p_{10}(1-R)\right] \tag{A.22}$$

$$T = \frac{1}{E_i}\left(Ae^{ik_{1z}d} + Be^{-ik_{1z}d}\right)e^{-ik_{2z}d} \tag{A.23}$$

$$R_{01} = -R_{10} = \frac{1-p_{01}}{1+p_{01}} \qquad R_{12} = -R_{21} = \frac{1-p_{12}}{1+p_{12}} \tag{A.24}$$

$$p_{01} = \frac{1}{p_{10}} = \frac{\epsilon_0 k_{1z}}{\epsilon_1 k_{0z}} \qquad p_{12} = \frac{1}{p_{21}} = \frac{\epsilon_1 k_{2z}}{\epsilon_2 k_{1z}} \tag{A.25}$$

Appendix B

Scattering by an Infinite Cylinder

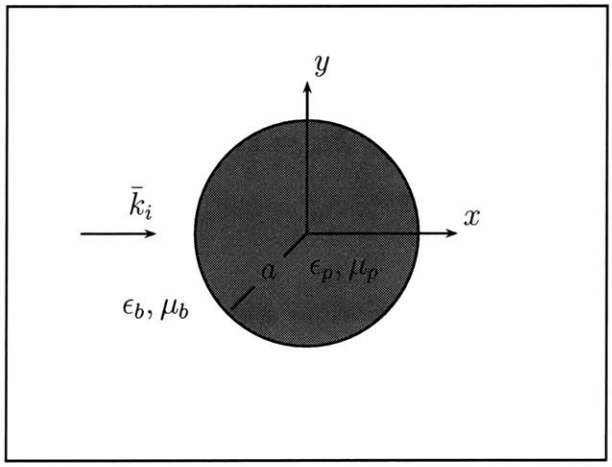

Figure B-1: Scattering from an infinite cylinder. The geometry for the problem is an infinitely long cylinder in the $\hat{z}$-direction. The cylinder of radius a, which can be used to represent a circular particle in two dimensions, is composed of isotropic material (μ_p, ϵ_p) in a background of (μ_b, ϵ_b).

The geometry of the problem is shown in Fig. B-1. It consists of an electromagnetic wave incident upon an infinite cylinder of radius a. The cylinder is characterized by (μ_p, ϵ_p) and the background by (μ_b, ϵ_b). The incident wave is assumed to be a plane wave with $e^{-i\omega t}$ dependence. Note that many other field distributions, such as a Gaussian beam, can be described by a sum of plane-waves. Therefore, the

total solution for such incident fields can be described as a superposition of solutions resulting from a plane-wave. The incident, scattered, and internal fields are expanded in cylindrical waves given by $\bar{N}_n$, $\bar{M}_n$, $Rg\bar{N}_n$, and $Rg\bar{M}_n$. The solution is given by [112].

The incident electric field is polarized in the $\hat{z}$-direction and propagates in the plane ($k_z = 0$). The magnetic fields are obtained from Faraday's law

$$i\omega\mu\bar{H}(\bar{\rho}) = \nabla \times \bar{E}(\bar{\rho}) \tag{B.1}$$

using the identities

$$\nabla \times \bar{M}_n = k\bar{N}_n \tag{B.2a}$$

$$\nabla \times \bar{N}_n = k\bar{M}_n. \tag{B.2b}$$

The incident fields are regular at the origin and are given by

$$\bar{E}_{inc}(\bar{\rho}) = \hat{z}E_0 e^{i\bar{k}_i\cdot\bar{\rho}} = \sum_{n=-N}^{N} a_n Rg\bar{N}_n(k_b, \bar{\rho}) \tag{B.3a}$$

$$\bar{H}_{inc}(\bar{\rho}) = \frac{k_b}{i\omega\mu_b}\sum_{n=-N}^{N} a_n Rg\bar{M}_n(k_b, \bar{\rho}), \tag{B.3b}$$

where the wavenumber in the background medium is given by the dispersion relation $k_b^2 = \omega^2\mu_b\epsilon_b$. The scattered fields are

$$\bar{E}_{scat}(\bar{\rho}) = \sum_{n=-N}^{N} a_n^s \bar{N}_n(k_b, \bar{\rho}) \tag{B.4a}$$

$$\bar{H}_{scat}(\bar{\rho}) = \frac{k_b}{i\omega\mu_b}\sum_{n=-N}^{N} a_n^s \bar{M}_n(k_b, \bar{\rho}). \tag{B.4b}$$

The internal fields are also regular at the origin and can be computed from

$$\bar{E}_{int}(\bar{\rho}) = \sum_{n=-N}^{N} c_n Rg\bar{N}_n(k_p, \bar{\rho}) \tag{B.5a}$$

$$\bar{H}_{int}(\bar{\rho}) = \frac{k_p}{i\omega\mu_p} \sum_{n=-N}^{N} c_n Rg\bar{M}_n(k_p, \bar{\rho}), \tag{B.5b}$$

where the wavenumber in the cylinder ($\rho < a$) is given by $k_p^2 = \omega^2\mu_p\epsilon_p$. The unknown coefficients (a_n^s, c_n) are determined by matching the boundary conditions and the coefficients (a_n) are known from the incident plane wave expansion [112]. The expressions for incident, scattered, and internal fields become exact for $N \to \infty$. The vector cylindrical wave functions for this particular incidence are given by [55]

$$\bar{N}_n(k, \bar{\rho}) = \hat{z}kH_n^{(1)}(k\rho)e^{in\phi} \tag{B.6a}$$

$$\bar{M}_n(k, \bar{\rho}) = \hat{\rho}\left[i\frac{n}{\rho}H_n^{(1)}(k\rho)\right]e^{in\phi} + \hat{\phi}\left[kH_{n+1}^{(1)}(k\rho) - \frac{n}{\rho}H_n^{(1)}(k\rho)\right]e^{in\phi} \tag{B.6b}$$

$$Rg\bar{N}_n(k, \bar{\rho}) = \hat{z}kJ_n(k\rho)e^{in\phi} \tag{B.6c}$$

$$Rg\bar{M}_n(k, \bar{\rho}) = \hat{\rho}\left[i\frac{n}{\rho}J_n(k\rho)\right]e^{in\phi} + \hat{\phi}\left[kJ_{n+1}(k\rho) - \frac{n}{\rho}J_n(k\rho)\right]e^{in\phi}. \tag{B.6d}$$

Here, $H_n^{(1)}(\cdot)$ is the Hankel function of the first kind and $J_n(\cdot)$ is the bessel function. The coordinates (ρ, θ, ϕ) represent the point for field evaluation (i.e. the observer position). The angle ϕ_i is used to represent the incident direction of the illuminating wave.

The simplest case is a perfect electrical conductor (PEC). For the PEC, the internal fields are assumed to be zero so that $c_n = 0$ for all n. Note that the discontinuity in the magnetic field at the surface gives rise to a surface current $\bar{J}_s$. However, since the incident wave is TE, it is expected that no resonant effects result from $\bar{J}_s$.

The coefficients for the incident and reflected wave are

$$a_n = i^n \frac{e^{in\phi_i}}{k_b} E_0 \tag{B.7a}$$

$$a_n^s = -a_n \frac{J_n(ka)}{H_n^{(1)}(ka)}. \tag{B.7b}$$

The fields were compared favorably with results obtained using the commercial software package CST Microwave Studio ®. Only a few field plots are presented here for future reference. Note that while several minutes are required for numerical programs to calculate the fields suitable for radiation pressure studies, the analytic approach detailed in these notes require only a couple of seconds since the field evaluation at one point in space requires far less than a second using a MATLAB script based on the equations contained herein.

For a general dielectric and magnetic medium, the boundary conditions give a 2×2 system of equations that must be solved for the unknown coefficients,

$$a_n = i^n \frac{e^{in\phi_i}}{k_b} E_0 \tag{B.8a}$$

$$a_n^s = \frac{b_1 m_{22} - b_2 m_{12}}{m_{11} m_{22} - m_{21} m_{12}} \tag{B.8b}$$

$$c_n = \frac{b_1 m_{21} - b_2 m_{11}}{m_{12} m_{21} - m_{22} m_{11}}. \tag{B.8c}$$

The matrix elements and RHS for the linear system are

$$m_{11} = -k_b H_n^{(1)}(k_b a) \tag{B.9a}$$

$$m_{12} = k_p J_n(k_p a) \tag{B.9b}$$

$$m_{21} = -k_b H_{n+1}^{(1)}(k_b a) + \frac{n}{a} H_n^{(1)}(k_b a) \tag{B.9c}$$

$$m_{22} = \frac{\mu_b k_p}{\mu_p k_b} \left[k_p J_{n+1}(k_p a) - \frac{n}{a} J_n(k_p a) \right] \tag{B.9d}$$

$$b_1 = a_n k_b J_n(k_b a) \tag{B.9e}$$

$$b_2 = a_n \left[k_b J_{n+1}(k_b a) - \frac{n}{a} J_n(k_b a) \right]. \tag{B.9f}$$

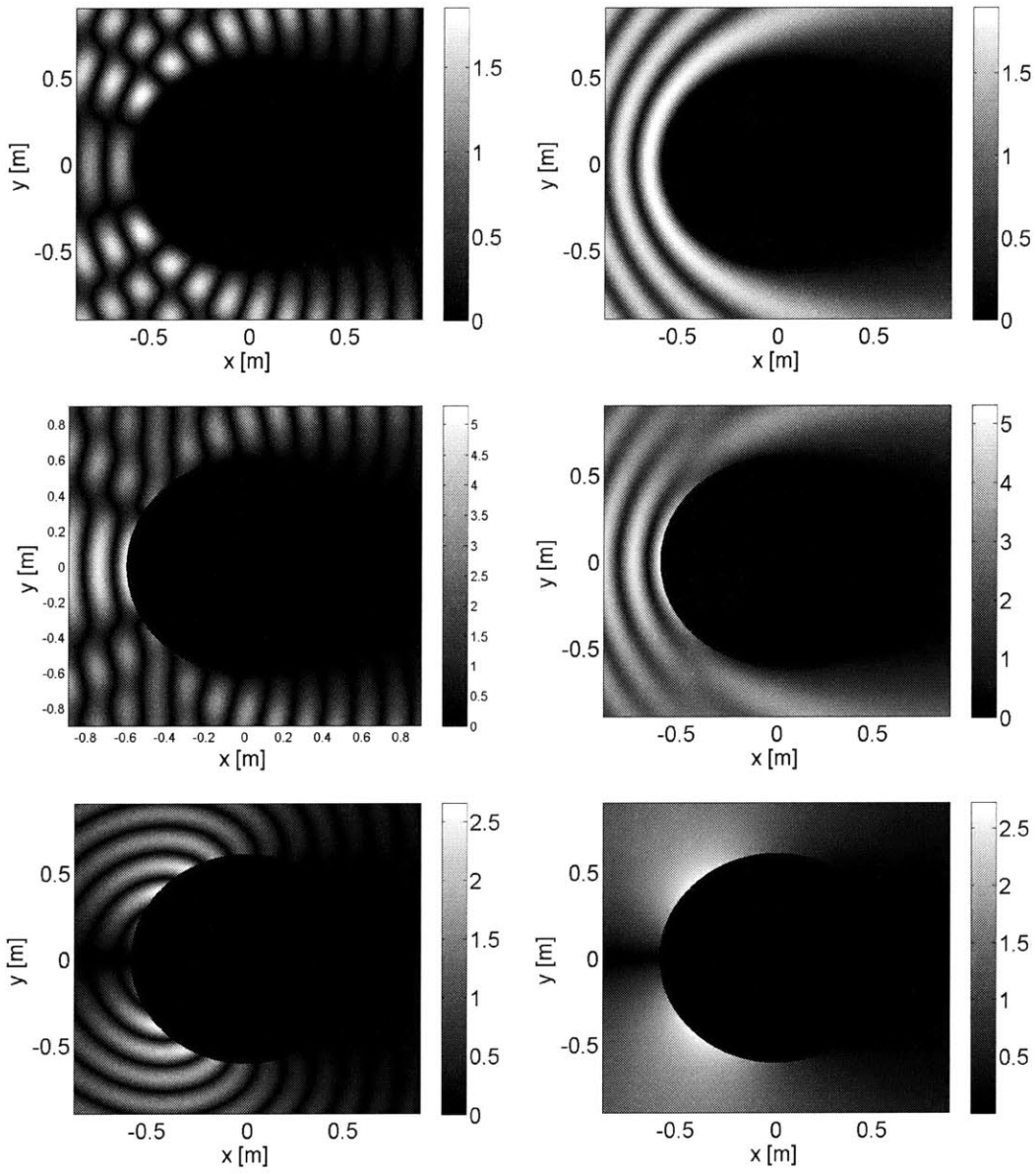

Figure B-2: A 1 GHz electromagnetic plane wave scattered from an infinite PEC cylinder. The wave is incident from free space ($\epsilon_b = \epsilon_0$, $\mu_b = \mu_0$) in the $\hat{x}$ direction. The radius of the cylinder is $a = 2\lambda_0 \approx 0.6\ m$ and the calculation was performed with $N = 40$. The left column is magnitude of the real part of the complex field, and the right column is absolute value of the field. The fields are, from top to bottom, E_z, H_y, H_x. The order of magnitude is 10^-3 for the magnetic field.

The resulting fields compare favorably with results obtained using the commercial software package CST Microwave Studio ®.

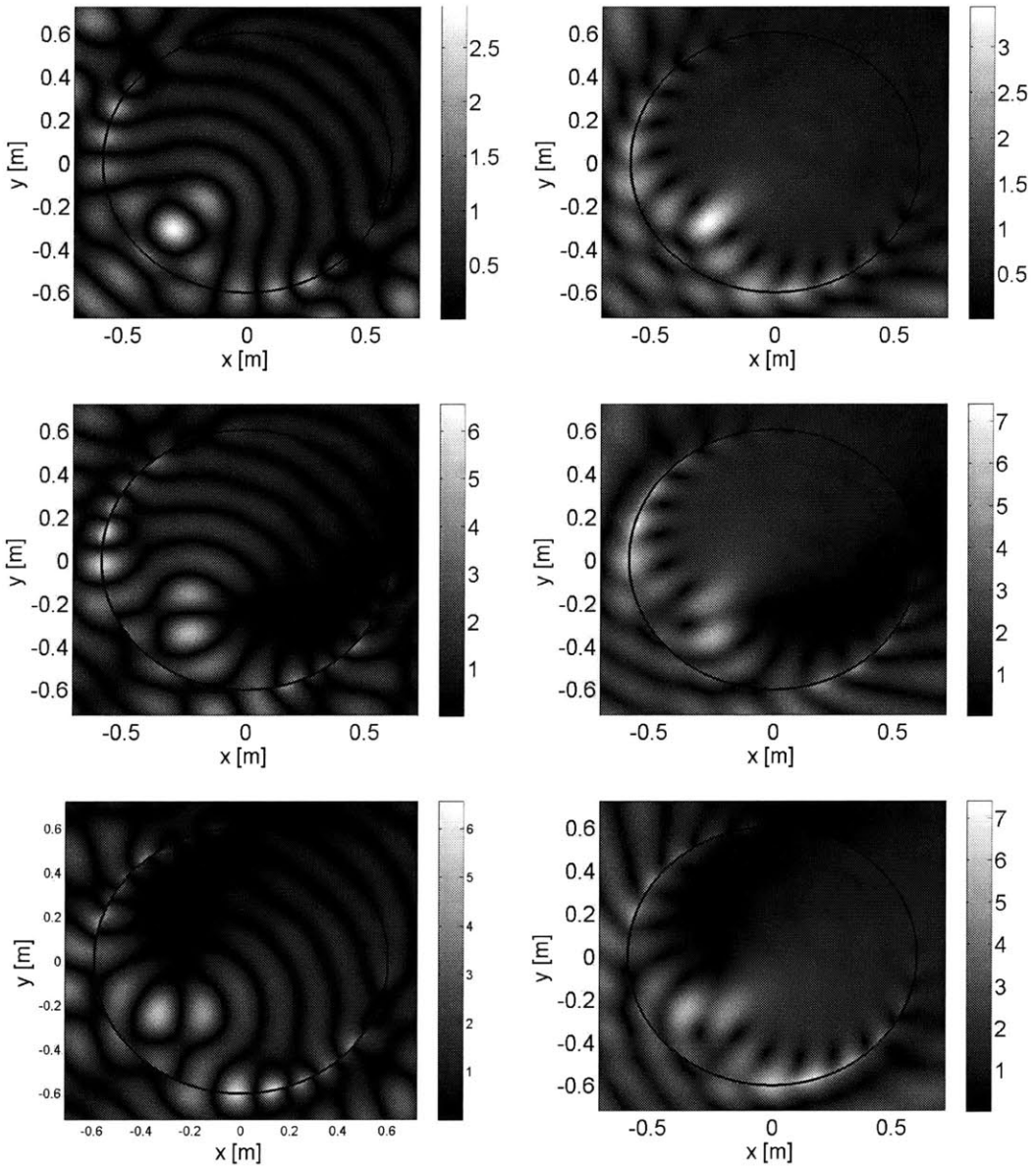

Figure B-3: A 1 GHz electromagnetic plane wave scattered from an infinite LHM cylinder ($\epsilon_p = -\epsilon_0$, $\mu_p = -\mu_0$). The wave is incident from free space ($\epsilon_b = \epsilon_0$, $\mu_b = \mu_0$) at an angle $\phi_i = \pi/4$. The radius of the cylinder is $a = 2\lambda_0 \approx 0.6\ m$ and the calculation was performed with $N = 40$. The left column is magnitude of the real part of the complex field, and the right column is absolute value of the field. The fields are, from top to bottom, E_z, H_y, H_x. The order of magnitude is 10^{-3} for the magnetic field.

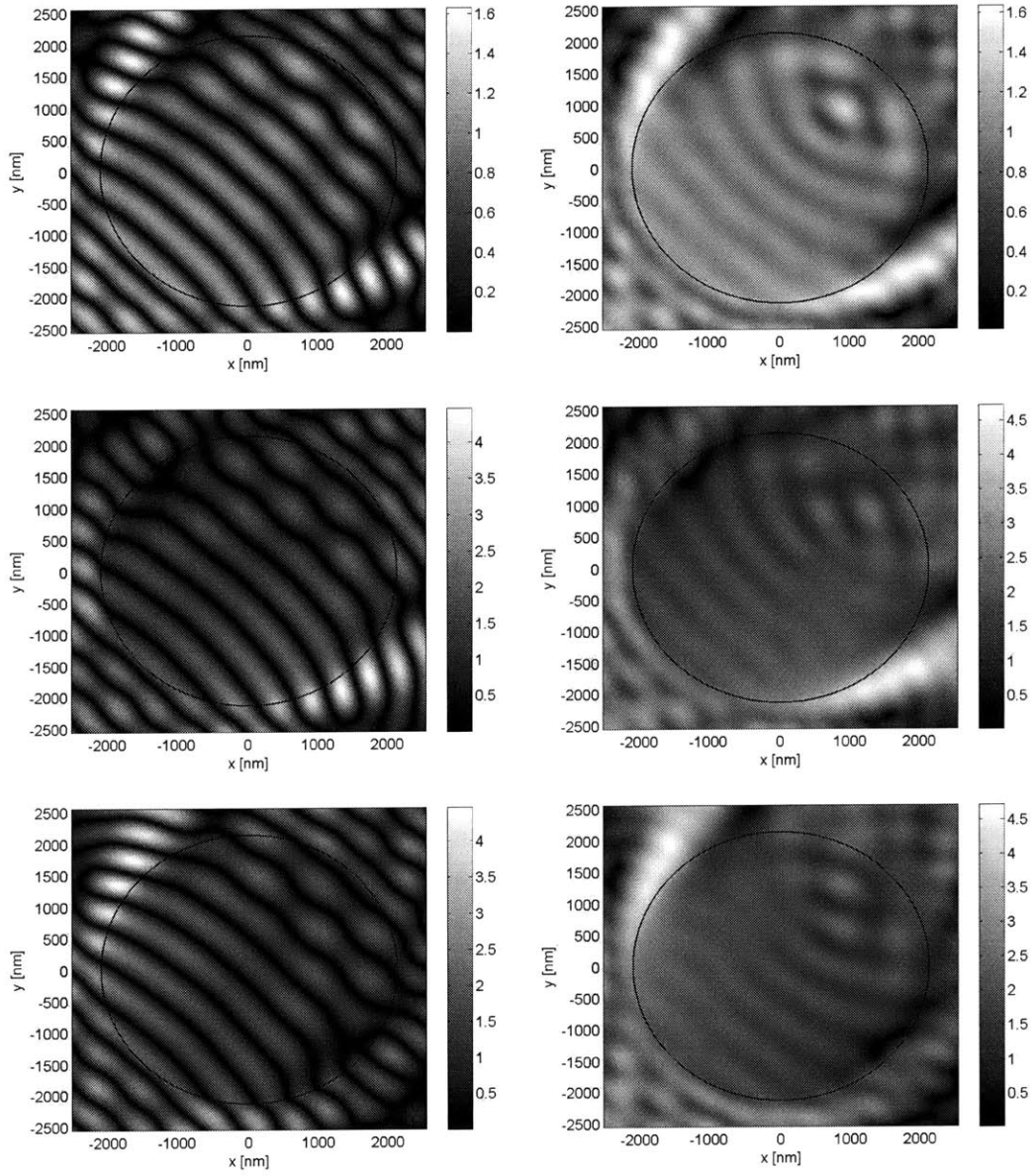

Figure B-4: Electromagnetic fields resulting from a plane wave scattered from an infinite air cylinder ($\epsilon_p = \epsilon_0$, $\mu_p = \mu_0$). The wave is incident from water ($\epsilon_b = 1.69\epsilon_0$, $\mu_b = \mu_0$) at an angle $\phi_i = \pi/4$. The radius of the cylinder is $a = 2\lambda_0$, where $\lambda_0 = 1064\ nm$ is the wavelength of the incident wave. The calculation was performed with $N = 40$. The left column is magnitude of the real part of the complex field, and the right column is absolute value of the field. The fields are, from top to bottom, E_z, H_y, H_x. The order of magnitude is 10^{-3} for the magnetic field.

Appendix C

Scattering by a Sphere

The incident electric field is polarized in the $\hat{x}$-direction and propagates in the $\hat{z}$-direction. The background is characterized by (ϵ_b, μ_b) with a wavenumber k_b. The particle is composed of (ϵ_p, μ_p) with wavenumber k_p. The geometry of the problem is shown in Fig. C-1. The incident fields are

$$\bar{E}_{inc} = \hat{x} E_0 e^{ik_b z} = \hat{x} E_0 e^{ik_b r\cos\theta} \tag{C.1a}$$

$$\bar{H}_{inc} = \hat{y}\frac{E_0}{\eta_b} e^{ik_b z} = \hat{y}\frac{E_0}{\eta_b} e^{ik_b r\cos\theta}. \tag{C.1b}$$

The solution is found by expanding the incident, scattered, and internal fields as a sum of spherical waves. The unknown coefficients for the scattered and internal fields are found from the boundary conditions. The problem and solution are given in [39].

The incident wave is expanded in spherical modes using the identity

$$e^{ikr\cos\theta} \approx \sum_{n=0}^{N} (-i)^{-n}(2n+1) j_n(kr) P_n(\cos\theta), \tag{C.2}$$

where $j_n(kr)$ is a spherical Bessel function and $P_n(\cos\theta)$ is the Legendre function.

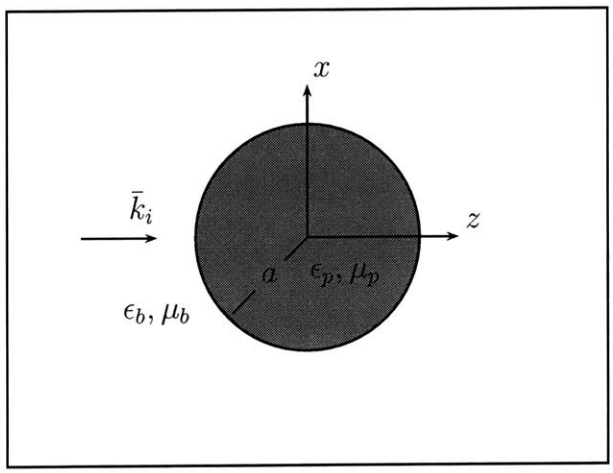

Figure C-1: Scattering from an isotropic sphere. The sphere of radius a, which can be used to represent a circular particle in three dimensions, is composed of isotropic material (μ_p, ϵ_p) in a background of (μ_b, ϵ_b). The incident wave is linearly polarized in the $\hat{x}$ direction and propagates in the $\hat{z}$ direction.

The approximation is exact as $N \to \infty$.

The incident, scattered, and internal waves are decomposed into TM to $\hat{r}$ and TE to $\hat{r}$ waves by using scalar potentials π_e and π_m respectively. The potentials are defined by

$$\bar{A} = \bar{r}\pi_e \tag{C.3a}$$

$$\bar{H} = \nabla \times \bar{A} = \hat{\theta}\frac{1}{\sin\theta}\frac{\partial}{\partial\phi}\pi_e - \hat{\phi}\frac{\partial}{\partial\theta}\pi_e \tag{C.3b}$$

for TM waves and

$$\bar{Z} = \bar{r}\pi_m \tag{C.4a}$$

$$\bar{E} = \nabla \times \bar{Z} = \hat{\theta}\frac{1}{\sin\theta}\frac{\partial}{\partial\phi}\pi_m - \hat{\phi}\frac{\partial}{\partial\theta}\pi_m \tag{C.4b}$$

for TE waves. The potentials satisfy the Helmholtz equation in spherical coordinates

$$\left(\nabla^2 + k^2\right)\pi = 0. \tag{C.5}$$

The scaler potentials are

$$\pi_e = \sum_{n=1}^{N} A_n z_n(kr) P_n^1(\cos\theta)\cos\phi \tag{C.6a}$$

$$\pi_m = \sum_{n=1}^{N} B_n z_n(kr) P_n^1(\cos\theta)\sin\phi, \tag{C.6b}$$

where $z_n(kr)$ represents solutions to the Bessel equation. The solutions differ in the three regions by the following.

- Incident (π_e, π_m)

$$\begin{aligned} z_n(kr) &= j_n(k_b r) \\ A_n &= E_0 \frac{k_b}{\omega\mu_b} \cdot \frac{(-i)^{-n}(2n+1)}{n(n+1)} \\ B_n &= -A_n \frac{\omega\mu_b}{k_b} \end{aligned}$$

- Scattered (π_e^s, π_m^s)

$$\begin{aligned} z_n(kr) &= h_n(k_b r) \\ A_n &= E_0 \frac{k_b}{\omega\mu_b} \cdot a_n \\ B_n &= -E_0 \cdot b_n \end{aligned}$$

$h_n(k_b r) = h_n^{(1)}(k_b r)$ is the spherical Hankel function of the first kind.

- internal (π_e^i, π_m^i)

$$\begin{aligned} z_n(kr) &= j_n(k_p r) \\ A_n &= E_0 \frac{k_p}{\omega\mu_p} \cdot c_n \\ B_n &= -E_0 \cdot d_n \end{aligned}$$

The unknown coefficients a_n, b_n, c_n, d_n are found using the boundary conditions for the tangential electric field and tangential magnetic field.

The total fields are:

$$E_r = i\frac{k}{\omega\epsilon}\sum_{n=1}^{N} A_n P_n^1(\cos\theta)\left[krz_n(kr) + 2z_n'(kr) + krz_n''(kr)\right]\cos\phi \tag{C.10a}$$

$$E_\theta = \sum_{n=1}^{N}\left\{iA_n\frac{k}{\omega\epsilon}\frac{\partial}{\partial\theta}P_n^1(\cos\theta)\left[\frac{1}{kr}z_n(kr) + z_n'(kr)\right]\right.$$
$$\left. + B_n\frac{P_n^1(\cos\theta)}{\sin\theta}z_n(kr)\right\}\cos\phi \tag{C.10b}$$

$$E_\phi = -\sum_{n=1}^{N}\left\{iA_n\frac{k}{\omega\epsilon}\frac{P_n^1(\cos\theta)}{\sin\theta}\left[\frac{1}{kr}z_n(kr) + z_n'(kr)\right]\right.$$
$$\left. + B_n\frac{\partial}{\partial\theta}P_n^1(\cos\theta)z_n(kr)\right\}\sin\phi \tag{C.10c}$$

$$H_r = -i\frac{k}{\omega\mu}\sum_{n=1}^{N} B_n P_n^1(\cos\theta)\left[krz_n(kr) + 2z_n'(kr) + krz_n''(kr)\right]\sin\phi \tag{C.10d}$$

$$H_\theta = -\sum_{n=1}^{N}\left\{iB_n\frac{k}{\omega\mu}\frac{\partial}{\partial\theta}P_n^1(\cos\theta)\left[\frac{1}{kr}z_n(kr) + z_n'(kr)\right]\right.$$
$$\left. - A_n\frac{P_n^1(\cos\theta)}{\sin\theta}z_n(kr)\right\}\sin\phi \tag{C.10e}$$

$$H_\phi = -\sum_{n=1}^{N}\left\{iB_n\frac{k}{\omega\mu}\frac{P_n^1(\cos\theta)}{\sin\theta}\left[\frac{1}{kr}z_n(kr) + z_n'(kr)\right]\right.$$
$$\left. + A_n\frac{\partial}{\partial\theta}P_n^1(\cos\theta)z_n(kr)\right\}\cos\phi \tag{C.10f}$$

The spherical Bessel and Hankel functions $z_n(\xi)$ are given in terms of the Bessel and Hankel functions $Z_n(\xi)$ by

$$z_n(\xi) = \sqrt{\frac{\pi}{2\xi}}Z_{n+\frac{1}{2}}(\xi). \tag{C.11}$$

To evaluate the derivatives, it is helpful to define $l = n+2$, $m = n+1$, $p = n-1$, and $q = n-2$ and use the relation [55]

$$z_n'(\xi) = \frac{n}{2n+1}z_p(\xi) - \frac{m}{2n+1}z_m(\xi). \tag{C.12}$$

The second derivative with respect to the argument ξ is

$$z_n''(\xi) = \frac{n}{(2n+1)(2p+1)}\left[pz_q(\xi) - nz_n(\xi)\right] - \frac{m}{(2n+1)(2m+1)}\left[mz_n(\xi) + lz_l(\xi)\right]. \tag{C.13}$$

The derivative of the Legendre function with respect to the argument is, in general, known. Therefore, a useful relation is

$$\frac{\partial}{\partial\theta}P_n^m(\cos\theta) = -\sin\theta\frac{\partial}{\partial\cos\theta}P_n^m(\cos\theta). \tag{C.14}$$

The coefficients as determined from the boundary conditions are [113]

$$a_n = g_n \cdot \frac{k_b\epsilon_p\hat{J}_n(k_pa)\hat{J}_n'(k_ba) - k_p\epsilon_b\hat{J}_n(k_ba)\hat{J}_n'(k_pa)}{k_p\epsilon_b\hat{H}_n(k_ba)\hat{J}_n'(k_pa) - k_b\epsilon_p\hat{J}_n(k_pa)\hat{H}_n'(k_ba)} \tag{C.15a}$$

$$b_n = g_n \cdot \frac{k_b\mu_p\hat{J}_n(k_pa)\hat{J}_n'(k_ba) - k_p\mu_b\hat{J}_n(k_ba)\hat{J}_n'(k_pa)}{k_p\mu_b\hat{H}_n(k_ba)\hat{J}_n'(k_pa) - k_b\mu_p\hat{J}_n(k_pa)\hat{H}_n'(k_ba)} \tag{C.15b}$$

$$c_n = g_n \cdot \frac{ik_b\epsilon_p\mu_p}{k_b\epsilon_p\mu_b\hat{J}_n(k_pa)\hat{H}_n'(k_ba) - k_p\epsilon_b\mu_p\hat{H}_n(k_ba)\hat{J}_n'(k_pa)} \tag{C.15c}$$

$$d_n = g_n \cdot \frac{ik_p\mu_p}{k_b\mu_p\hat{J}_n(k_pa)\hat{H}_n'(k_ba) - k_p\mu_b\hat{H}_n(k_ba)\hat{J}_n'(k_pa)} \tag{C.15d}$$

where

$$g_n = \frac{(-i)^{-n}(2n+1)}{n(n+1)}. \tag{C.16}$$

The Ricatti-Bessel functions $\hat{J}_n(\xi)$ and $\hat{H}_n(\xi) = \hat{H}_n^{(1)}(\xi)$ are

$$\hat{Z}_n(\xi) = \xi z_n(\xi) \tag{C.17a}$$

$$\hat{Z}_n'(\xi) = z_n(\xi) + \xi z_n'(\xi). \tag{C.17b}$$

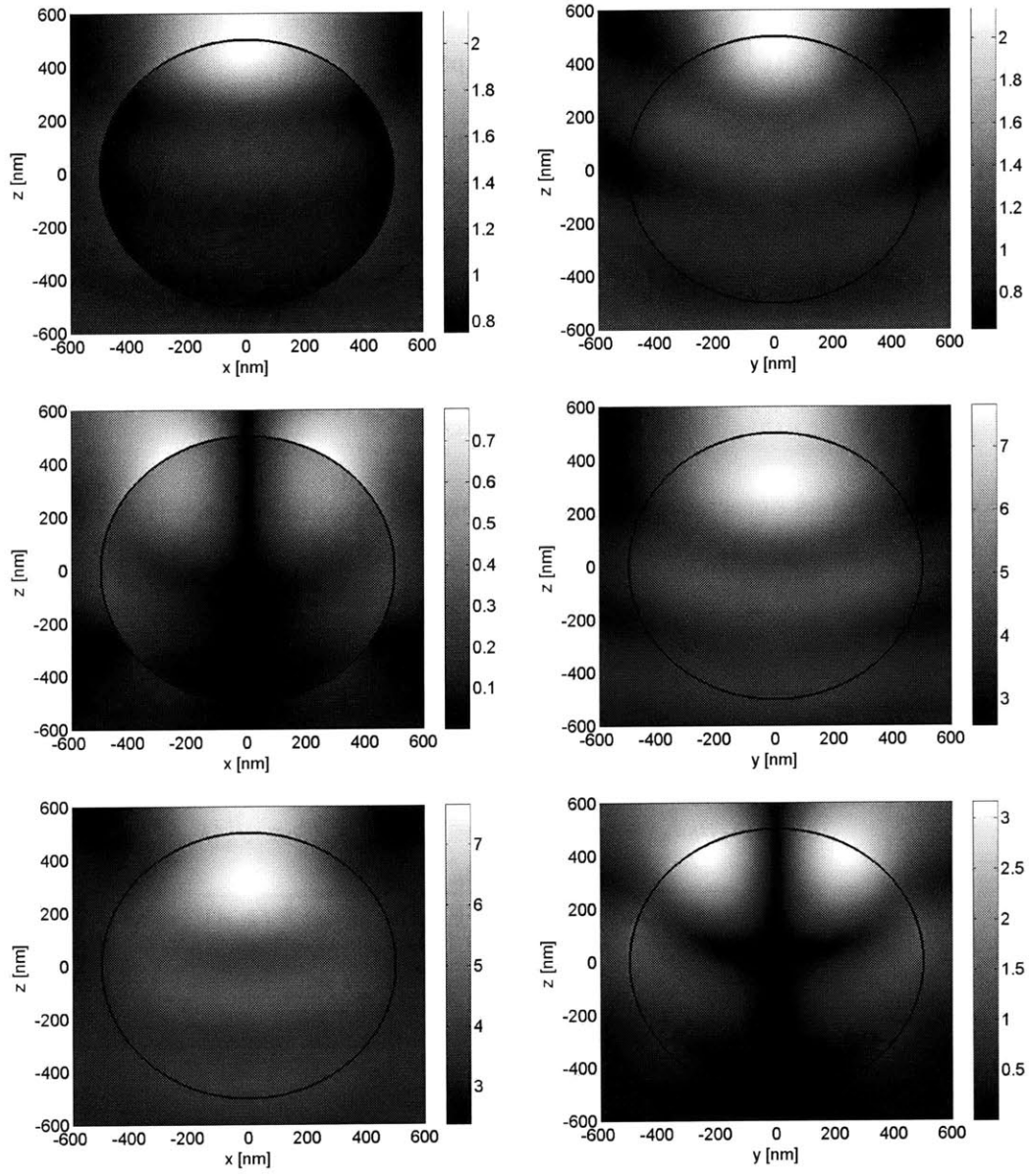

Figure C-2: Absolute values of the electromagnetic fields resulting from a plane wave scattered from a dielectric sphere ($\epsilon_p = 2.56\epsilon_0$, $\mu_p = \mu_0$). The wave is incident from water ($\epsilon_b = 1.69\epsilon_0$, $\mu_b = \mu_0$) in the $\hat{z}$ direction. The radius of the sphere is 0.5 μm, and $\lambda_0 = 1064\ nm$ is the wavelength of the incident wave. The calculation was performed with $N = 100$. The fields are, from top to bottom, (left column) $|E_x|$, $|E_z|$, and $|H_y|$ in the $y = 0$ plane and (right column) $|E_x|$, $|H_y|$, and $|H_z|$ in the $x = 0$ plane. The order of magnitude of the magnetic field is 10^{-3}.

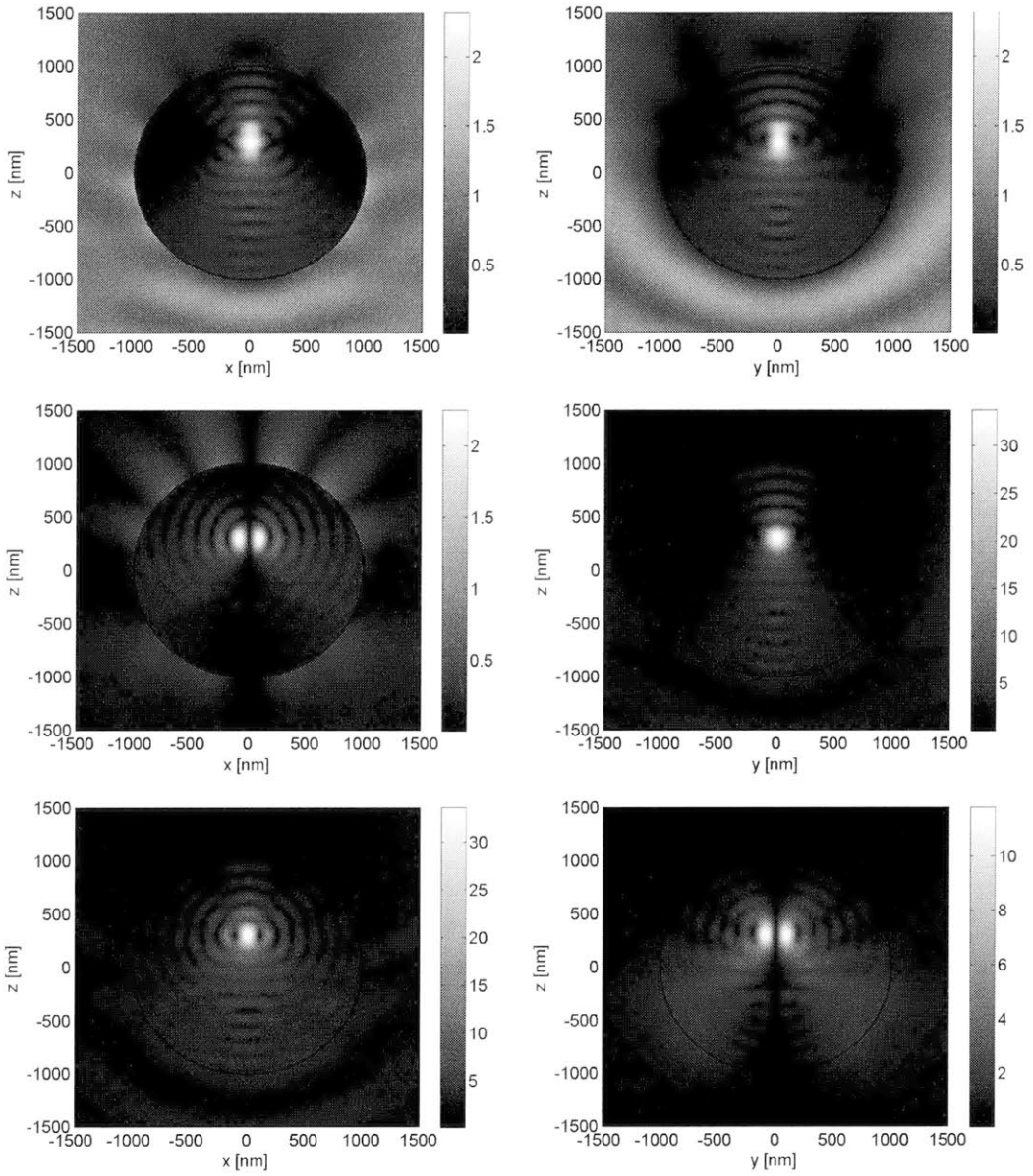

Figure C-3: Absolute values of the electromagnetic fields resulting from a plane wave scattered from a lossy sphere ($\epsilon_p = (16+i)\epsilon_0$, $\mu_p = \mu_0$). The wave is incident from free space ($\epsilon_b = \epsilon_0$, $\mu_b = \mu_0$) in the $\hat{z}$ direction. The radius of the sphere is 0.5 μm, and $\lambda_0 = 1064\ nm$ is the wavelength of the incident wave. The calculation was performed with $N = 100$. The fields are, from top to bottom, (left column) $|E_x|$, $|E_z|$, and $|H_y|$ in the $y = 0$ plane and (right column) $|E_x|$, $|H_y|$, and $|H_z|$ in the $x = 0$ plane. The order of magnitude of the magnetic field is 10^{-3}.

Appendix D

Field Solution for Multiple Slabs

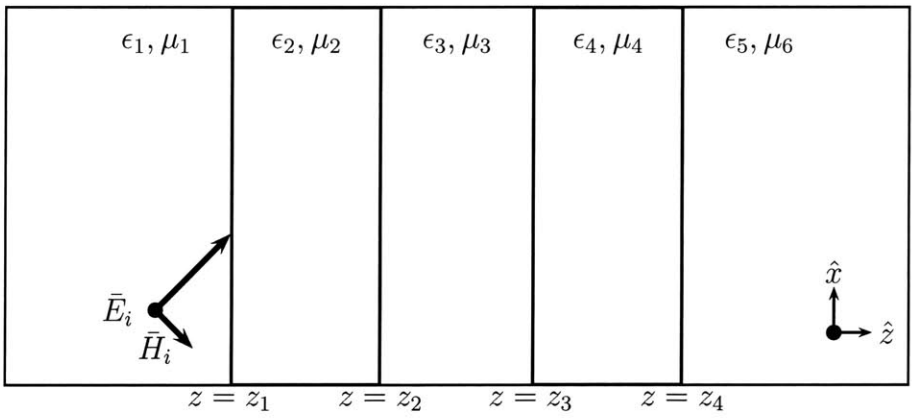

Figure D-1: The fields resulting from five layered media (4 boundaries) are found by matching the boundary conditions with counter propagating plane wave solutions in each region. The unit amplitude incident electric field is polarized in $\hat{y}$.

The fields in the five regions shown in Fig. D-1 are assumed to be plane wave solutions.

Region 1 $(A_1 = 1,\ B_1 = R)$

$$\bar{E}_1 = \hat{y}(e^{ik_{1z}} + Re^{-ik_{1z}z})e^{ik_x x} \tag{D.1a}$$

$$\bar{H}_1 = \hat{x}\frac{-k_{1z}}{\omega\mu_1}(e^{ik_{1z}} - Re^{-ik_{1z}z})e^{ik_x x} + \hat{z}\frac{k_x}{\omega\mu_1}(e^{ik_{1z}z} + Re^{-ik_{1z}z})e^{ik_x x} \tag{D.1b}$$

Region 2

$$\bar{E}_2 = \hat{y}(A_2 e^{ik_{2z}} + B_2 e^{-ik_{2z}z})e^{ik_x x} \tag{D.2a}$$

$$\bar{H}_2 = \left[\hat{x}\frac{-k_{2z}}{\omega\mu_2}(A_2 e^{ik_{2z}} - B_2 e^{-ik_{2z}z}) + \hat{z}\frac{k_x}{\omega\mu_2}(A_2 e^{ik_{2z}z} + B_2 e^{-ik_{2z}z})\right] e^{ik_x x} \tag{D.2b}$$

Region 3

$$\bar{E}_3 = \hat{y}(A_3 e^{ik_{3z}} + B_3 e^{-ik_{3z}z})e^{ik_x x} \tag{D.3a}$$

$$\bar{H}_3 = \left[\hat{x}\frac{-k_{3z}}{\omega\mu_3}(A_3 e^{ik_{3z}} - B_3 e^{-ik_{3z}z}) + \hat{z}\frac{k_x}{\omega\mu_3}(A_3 e^{ik_{3z}z} + B_3 e^{-ik_{3z}z})\right] e^{ik_x x} \tag{D.3b}$$

Region 4

$$\bar{E}_4 = \hat{y}(A_4 e^{ik_{4z}} + B_4 e^{-ik_{4z}z})e^{ik_x x} \tag{D.4a}$$

$$\bar{H}_4 = \left[\hat{x}\frac{-k_{4z}}{\omega\mu_4}(A_4 e^{ik_{4z}} - B_4 e^{-ik_{4z}z}) + \hat{z}\frac{k_x}{\omega\mu_4}(A_4 e^{ik_{4z}z} + B_4 e^{-ik_{4z}z})\right] e^{ik_x x} \tag{D.4b}$$

Region 5 $(A_5 = T,\ B_5 = 0)$

$$\bar{E}_5 = \hat{y}Te^{ik_{5z}}e^{ik_x x} \tag{D.5a}$$

$$\bar{H}_5 = \left[\hat{x}\frac{-k_{5z}}{\omega\mu_5}Te^{ik_{5z}} + \hat{z}\frac{k_x}{\omega\mu_5}Te^{ik_{5z}z}\right] e^{ik_x x} \tag{D.5b}$$

The coefficients are determined by matching the boundary conditions at z_1, z_2, z_3, and z_4. These eight equations (two for each boundary) can be written as a matrix equation in terms of the column vector of unknown coefficients. The solution is found by inverting the matrix.

The solution is simplified when we apply the equations to two identical dielectric slabs as in Chapter 5. Here, we let $\epsilon_1 = \epsilon_3 = \epsilon_5 = \epsilon_0$, $\epsilon_2 = \epsilon_4 = n^2\epsilon_0$ and $\mu_1 = \mu_2 = \mu_3 = \mu_4 = \mu_5$, where n is the index of refraction of the two slabs. Furthermore, the two slabs are of equal thickness os that we let $z_1 = 0$, $z_2 = d$, $z_3 = d + \delta$, and $z_4 = 2d + \delta$. Refer to Fig. 5-1. To evaluate the force in this case, we can apply the formula given in (5.4), which gives the force in terms of the coefficients $A_\delta = A_3$ and $B_\delta = B_3$. These coefficients are calculated in this simplified case using the closed-form expressions

$$A_\delta = -\frac{\left[\cos(kd) - i\left(\frac{n^2+1}{2n}\right)\sin(kd)\right] e^{-ik_0(d+\delta)}}{\Omega} \tag{D.6a}$$

$$B_\delta = -\frac{-i\left(\frac{n^2-1}{2n}\right)\sin(kd)e^{ik_0(d+\delta)}}{\Omega} \tag{D.6b}$$

where

$$\Omega = \left[\cos^2(kd) - \left(\frac{n^2+1}{2n}\right)^2 \sin^2(kd) - i2\left(\frac{n^2+1}{2n}\right)\cos(kd)\sin(kd)\right] e^{-ik_0\delta} + \left(\frac{n^2-1}{2n}\right)^2 \sin^2(kd)e^{ik_0\delta}. \tag{D.7}$$

Appendix E

Scattering by Multiple Cylinders

The scattering from multiple cylinders is solved analytically by applying the formulation proposed by Foldy [106] and Lax [114]. The formulation presented here is reproduced from [115]. The total excitation field of particle q is the incident field plus the scattered field from all other particles except itself, and is written mathematically as

$$\bar{E}_{ex}^{(q)}(\bar{\rho}) = \bar{E}_{inc}(\bar{\rho}) + \sum_{l \neq q} \bar{E}_{scat}^{(l)}(\bar{\rho}). \tag{E.1}$$

The incident field field is given in terms of the Bessel functions in Appendix B, and, as a generalization of those results, the scattered field of particle q is

$$\bar{E}_{scat}^{(q)}(\bar{\rho}) = \sum_{n=-N}^{+N} a_n^{s(q)} \bar{N}_n(k_b, \bar{\rho} - \bar{\rho}_q). \tag{E.2}$$

The cylindrical wave functions $\bar{N}_n$ were given in Appendix B and must be evaluated at translated origins for each particle q located at $\bar{\rho}_q$. The scattering coefficients are given by $a_n^{s(q)} = T_n w_n^{(q)}$, where T_n is the known coefficient for a cylinder. For the given

s-polarized (TM) wave,

$$T_n = \frac{k_p}{k_b}\frac{J_n(k_p a)}{H_n^{(1)}(k_b a)}B_n - \frac{J_n(k_b a)}{H_n^{(1)}(k_b a)} \tag{E.3a}$$

$$B_n = \frac{2ik_b}{\pi a k_p}\left[k_b H_n^{(1)'}(k_b a)J_n(k_p a) - k_p J_n'(k_p a)H_n^{(1)}\right]^{-1} \tag{E.3b}$$

and the $w_n^{(q)}$ are solved from

$$w_n^{(q)} = e^{i\bar{k}_b\cdot\bar{\rho}_q}a_n + \sum_{n'=-N}^{+N}\sum_{l\neq q} H_{n-n'}^{(1)}(k_b|\bar{\rho}_l - \bar{\rho}_q|)e^{-i(n-n')\phi_{lq}}T_{n'}w_{n'}^{(l)}, \tag{E.4}$$

where ϕ_{lq} is the angel between $\hat{x}$ and the vector joining the centers of particles (l) and (q). The solution is exact as $N \to \infty$. In reality, the summation over n is truncated. Thus, the solution of (E.4) requires the inversion of a square matrix of dimension $L \times (2N+1)$, where L is the number of particles. This formulation was implemented in FORTRAN by Dr. Grzegorczyk and validated via numerous examples using the commercial field solver CST Microwave Studio ®. An example is plotted in Fig. E-1. In the example, the 1 GHz electromagnetic wave is incident from free space in the $\hat{x}$ direction upon two identical dielectric cylinders ($\epsilon_p = 2\epsilon_0$, $a = \lambda_0/2$) cylinders separated by $3\lambda_0$. Although not shown, the electric and magnetic fields of this example and several others involving multiple cylinders compare favorably with the fields generated using CST Microwave Studio ®.

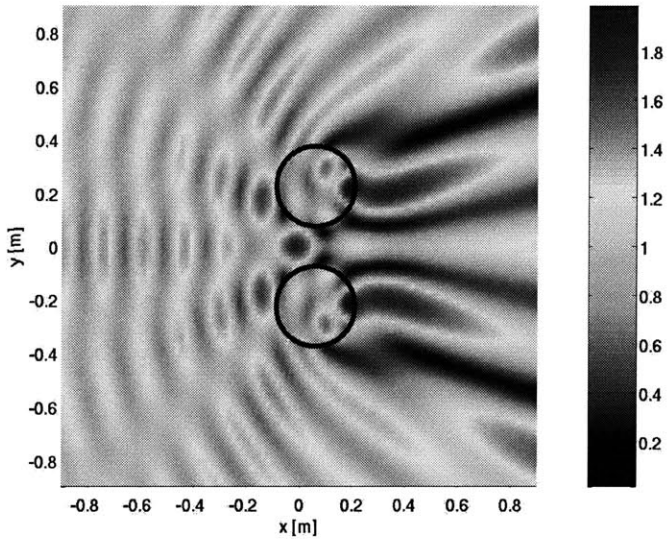

Figure E-1: Electric field magnitude $|E_z|$ scattered from 2 dielectric cylinders. The incident electric field is unit amplitude at 1 GHz propagating in the $\hat{x}$ direction. The two identical cylinders of permittivity $\epsilon_p = 2\epsilon_0$ and radius $a = \lambda_0/2$ are separated by a center-to-center distance of $3a$. The background is free space $\epsilon_b = \epsilon_0$

Bibliography

[1] B. A. Kemp, T. M. Grzegorczyk, and J. A. Kong. Ab initio study of the radiation pressure on dielectric and magnetic media. *Opt. Express*, 13:9280, 2005.

[2] B. A. Kemp, J. A. Kong, and T. M. Grzegorczyk. Reversal of wave momentum in isotropic left-handed media. *Phys. Rev. A*, Accepted for Publication, 2007.

[3] B. A. Kemp, T. M. Grzegorczyk, and J. A. Kong. Lorentz force on dielectric and magnetic particles. *J. of Electromagn. Waves and Appl.*, 20:827, 2006.

[4] B. A. Kemp, T. M. Grzegorczyk, and J. A. Kong. Optical momentum transfer to absorbing mie particles. *Phys. Rev. Lett.*, 97:133902, 2006.

[5] T. M. Grzegorczyk, B. A. Kemp, and J. A. Kong. Trapping and binding of an arbitrary number of cylindrical particles in an in-plane electromagnetic field. *J. Opt. Soc. Am. A*, 23:2324, 2006.

[6] T. M. Grzegorczyk, B. A. Kemp, and J. A. Kong. Stable optical trapping based on optical binding forces. *Phys. Rev. Lett.*, 96:113903, 2006.

[7] T. M. Grzegorczyk, B. A. Kemp, and J. A. Kong. Passive guiding and sorting of small particles with optical binding forces. *Opt. Lett.*, 31:3378, 2006.

[8] J. C. Maxwell. *A Treatise on Electricity and Magnetism.* Constable, London, 1891.

[9] P. Lebedew. Pressure of light. *Ann. Phys*, 6:433, 1901.

[10] E. F. Nichols and G. F. Hull. The pressure due to radiation. *Phys. Rev.*, 17:26, 1903.

[11] J. H. Poynting. Tangential stress of light obliquely incident on absorbing surface. *Phil. Mag*, 24:156, 1905.

[12] A. Ashkin. Acceleration and trapping of particles by radiation pressure. *Phys. Rev. Lett.*, 24:156, 1970.

[13] A. Ashkin and J. M. Dziedzic. Optical levitation by radiation pressure. *Appl. Phys. Lett.*, 19:283, 1971.

[14] A. Ashkin and J. M. Dziedzic. Optical levitation in high vacuum. *Appl. Phys. Lett.*, 28:333, 1976.

[15] A. Ashkin and J. M. Dziedzic. Radiation pressure on a free liquid surface. *Phys. Rev. Lett.*, 30:139, 1973.

[16] A. Ashkin. Trapping of atoms by resonance radiation pressure. *Phys. Rev. Lett.*, 40:729, 1978.

[17] A. Ashkin and J. P. Gordon. Cooling and trapping of atoms by resonance radiation pressure. *Opt. Lett.*, 4:161, 1979.

[18] S. Chu, L. Holberg, J. E. Bjorkholm, A. Cable, and A. Ashkin. Three-dimensional viscous confinement and cooling of atoms by resonance radiation pressure. *Phys. Rev. Lett.*, 55:48, 1985.

[19] S. Chu, J. E. Bjorkholm, A. Ashkin, and A. Cable. Experimental observation of optically trapped atoms. *Phys. Rev. Lett.*, 57:314, 1986.

[20] S. Chu, J. E. Bjorkholm, A. Ashkin, J. P. Gordon, and L. Holberg. Proposal for optically cooling atoms to temperatures of the order of 10^{-6} k. *Opt. Lett.*, 11:73, 1986.

[21] J. P. Gordon. Radiation forces and momenta in dielectric media. *Phys. Rev. A*, 8:14, 1973.

[22] A. Ashkin, J. M. Dziedzic, J. E. Bjorkholm, and S. Chu. Observation of a single-beam gradient force optical trap for dielectric particles. *Opt. Lett.*, 11:288, 1986.

[23] R. Gussgard and T. Lindmo. Calculation of the trapping force in a strongly focused laser beam. *J. Opt. Soc. Am. B*, 9:1922, 1992.

[24] Y. Harada and T. Asakura. Radiation forces on a dielectric sphere in the rayleigh scattering regime. *Opt. Comm.*, 124:529, 1996.

[25] A. Ashkin. Optical trapping and manipulation of neutral particles using lasers. *Proc. Natl. Acad. Sci.*, 94:4853, 1997.

[26] A. Ashkin. History of optical trapping and manipulation of small-neutral particle, atoms, and molecules. *IEEE Journal of Selected Topics in Quantum Electronics*, 6:841, 2000.

[27] D. G. Grier. A revolution in optical manipulation. *Nature (London)*, 424:810, 2003.

[28] A. Ashkin and J. M. Dziedzic. Optical trapping and manipulation of viruses and bacteria. *Science*, 235:1517, 1987.

[29] K. Svoboda and S. M. Block. Optical trapping of metallic rayleigh particles. *Opt. Lett.*, 19:930, 1994.

[30] S. Sato, Y. Harada, and Y. Waseda. Optical trapping of microscopic metal particles. *Opt. Lett.*, 19:1807, 1994.

[31] Ricardo R. Brau. Private communication. MIT Biological Engineering, 2006.

[32] M. M. Burns, J. M. Fournier, and J. Golovchenko. Optical binding. *Phys. Rev. Lett.*, 63:1233, 1989.

[33] M. M. Burns, J. M. Fournier, and J. Golovchenko. Optical matter: crystallization and binding in intense optical fields. *Science*, 249:749, 1990.

[34] F. Depasse and J. M. Vigoureux. Optical binding force between two rayleigh particles. *J. Phys. D: Appl. Phys.*, 27:914, 1994.

[35] H. Minkowski. Die grundgleichungen für die elektromagnetischen vorgänge in bewegten Körpern. *Nachr. Ges. Wiss. Göttingen*, 1:53, 1908.

[36] M. Abraham. Zur elektrodynamik der bewegter Körper. *Rend. Pal.*, 28:1, 1909.

[37] M. Abraham. Sull'elettrodinamica di minkowski. *Rend. Pal.*, 30:33, 1910.

[38] D. F. Nelson. Momentum, pseudomomentum, and wave momentum: Toward resolving the minkowski-abraham controversy. *Phys. Rev. A*, 44:3985, 1991.

[39] J. A. Kong. *Electromagnetic Wave Theory.* EMW Publishing, Cambridge, MA, 2005.

[40] R. Loudon. Radiation pressure and momentum in dielectrics. *Fortschr. Phys*, 52:1134, 2004.

[41] R. Loudon. Theory of the radiation pressure on dielectric surfaces. *J. Mod. Opt.*, 49:821, 2002.

[42] R. Loudon, S. M. Barnett, and C. Baxter. Radiation pressure and momentum transfer in dielectrics: The photon drag effect. *Phys. Rev. A*, 71:063802, 2005.

[43] M. Mansuripur. Radiation pressure and the linear momentum of the electromagnetic field. *Opt. Express*, 12:5375, 2004.

[44] A. Zakharian, M. Mansuripur, and J. V. Moloney. Radiation pressure and the distribution of electromagnetic force in dielectric media. *Opt. Express*, 13:2321, 2005.

[45] M. Mansuripur, A. R. Zakharian, and J. V. Moloney. Radiation pressure on a dielectric wedge. *Opt. Express*, 13:2064, 2005.

[46] M. Mansuripur. Radiation pressure and the linear momentum of light in dispersive dielectric media. *Opt. Express*, 13:2245, 2005.

[47] I. Brevik. Experiments in phenomenological electrodynamics and the electromagnetic energy-momentum tensor. *Phys. Rep.*, 52:133, 1979.

[48] J. H. Poynting and G. Barlow. The pressure of light against the source: The recoil from light. *Proc. R. Soc. Lond. A.*, 83:534, 1910.

[49] R. V. Jones and J. C. S. Richards. The pressure of radiation in a refracting medium. *Proc. R. Soc. Lond. A.*, 221:480, 1954.

[50] R. V. Jones and B. Leslie. The measurement of optical radiation pressure in dispersive media. *Proc. R. Soc. Lond. A.*, 360:347, 1978.

[51] A. F. Gibson, M. F. Kimmitt, A. O. Koohian, D. E. Evans, and G. F. D. Levy. A study of radiation pressure in a refractive medium by the photon drag effect. *Proc. R. Soc. Lond. A.*, 370:303, 1980.

[52] G. K. Campbell, A. E. Leanhardt, J. Mun, M. Boyd, E. W. Streed, W. Ketterle, and D. E. Pritchard. Photon recoil momentum in dispersive media. *Phys. Rev. Lett.*, 94:170403, 2005.

[53] P. Penfield and H. A. Haus. *Electrodynamics of Moving Media.* M.I.T. Press, Cambridge, MA, 1967.

[54] J. D. Jackson. *Classical Electrodynamics.* John Wiley and Sons, New York, 1999.

[55] J. A. Stratton. *Electromagnetic Theory.* McGraw-Hill, New York, 1941.

[56] F. Rasetti. Deflection of mesons in magnetized iron. *Phys. Rev.*, 66:1, 1944.

[57] A. R. Zakharian, P. Polynkin, M. Mansuripur, , and J. V. Moloney. Single-beam trapping of micro-beads in polarized light: Numerical simulations. *Opt. Express*, 14:3660, 2006.

[58] S. Linden, C. Enkrich, M. Wegener, J. Zhou, T. Koschny, and C. M. Soukoulis. Magnetic response of metamaterials at 100 terahertz. *Science*, 306:1351, 2004.

[59] A. N. Grigorenko, A. K. Geim, H. F. Gleeson, Y. Zhang, A. A. Firsov, I. Y. Khrushchev, and J. Petrovic. Nanofabricated media with negative permeability at visible frequencies. *Nature*, 438:335, 2005.

[60] A. F. Gibson, M. F. Kimmitt, and A. C. Walker. Photon drag in germanium. *Appl. Phys. Lett.*, 17:75, 1970.

[61] P. Daly and H. Gruenberg. Energy relations for plane waves reflected from moving media. *J. Appl. Phys.*, 38:4486, 1967.

[62] M. Mansuripur. Radiation pressure on submerged mirrors: Implications for the momentum of light in dielectric media. *Opt. Express*, 15:2677, 2007.

[63] R. Peierls. The momentum of light in a refracting medium. *Proc. R. Soc. Lond. A.*, 347:475, 1976.

[64] R. Peierls. The momentum of light in a refracting medium. ii. generalization. application to oblique reflexion. *Proc. R. Soc. Lond. A.*, 355:141, 1977.

[65] R. Loudon, L. Allen, and D. F Nelson. Propagation of electromagnetic energy and momentum through an absorbing dielectric. *Phys. Rev. E*, 55:1071, 1997.

[66] S. Stallinga. Energy and momentum of light in dielectric media. *Phys. Rev. E*, 73:026606, 2006.

[67] Y. N. Obukhov and F. W. Hehl. Electromagnetic energymomentum and forces in matter. *Phys. Lett. A*, 311:277, 2003.

[68] M. Scalora, G. D' Aguanno, N. Mattiucci, M. J. Bloemer, M. Centini, C. Sibilia, and J. W. Haus. Radiation pressure of light pulses and conservation of linear momentum in dispersive media. *Phys. Rev. E*, 73:056604, 2006.

[69] R. W. Ziolkowski. Superluminal transmission of information through an electromagnetic metamaterial. *Phys. Rev. E*, 63:046604, 2001.

[70] H. A. Haus. *Proc. of the IEEE*, 54:920, 1966.

[71] H. A. Haus. *Physica*, 43:77, 1969.

[72] Michael Scalora. Private communication. Charles M. Bowden Research Center, Redstone Arsenal, 2006.

[73] R. A. Shelby, D. R. Smith, and S. Schultz. Experimental verification of a negative index of refraction. *Science*, 292:77, 2001.

[74] D. R. Smith, W. J. Padilla, D. C. Vier, S. C. Nemat-Nasser, and S. Schultz. Composite medium with simultaneously negative permeability and permittivity. *Phys. Rev. Lett.*, 84:4184, 2000.

[75] J. Pacheco, T. M. Grzegorczyk, B. I. Wu, Y. Zhang, and J. A. Kong. Power propagation in homogeneous isotropic frequency-dispersive left-handed media. *Phys. Rev. Lett.*, 89:257401, 2002.

[76] C. G. Parazoli, R. B. Greegor, K. Li, B. E. C. Koltenbah, and M. Tanielian. Experimental verification and simulation of negative index of refraction using snells law. *Phys. Rev. Lett.*, 90:107401, 2003.

[77] J. Lu, T. M. Grzegorczyk, Y. Zhang, J. Pacheco, B. I. Wu, and J. A. Kong. Čerenkov radiation in materials with negative permittivity and permeability. *Opt. Express*, 11:723, 2003.

[78] R. Matloob and A. Ghaffari. Čerenkov radiation in a causal permeable medium. *Phys. Rev. A*, 70:052116, 2004.

[79] Y. O. Averkov and V. M. Yakovenko. *Phys. Rev. B*, 72:205110, 2005.

[80] S. D. Korovin, A. A. Eltchaninov, V. V. Rostov, V. G. Shpak, M. I. Yalandin, N. S. Ginzburg, A. S. Sergeev, and I. V. Zotova. *Phys. Rev. E*, 74:016501, 20056.

[81] J. B. Pendry. Negative refraction makes a perfect lens. *Phys. Rev. Lett.*, 85:3966, 2000.

[82] V. G. Veselago. The electrodynamics of substances with simultaneously negative values of ϵ and μ. *Sov. Phys. Usp.*, 10:509, 1968.

[83] S. Riyopoulos. Conservation of electromagnetic momentum and radiation forces exerted on left-handed material interfaces. *Opt. Lett.*, 31:2480, 2006.

[84] T. J. Cui and J. A. Kong. Time-domain electromagnetic energy in a frequency-dispersive left-handed medium. *Phys. Rev. E*, 70:205106, 2004.

[85] L. Brillouin. *Wave Propagation and Group Velocity.* Academic Press, New York, 1960.

[86] L. D. Landau, E. M. Lifshitz, and L. P. Pitaevskii. *Electrodynamics of Continuous Media, 2nd ed.* Pergamon, New York, 1984.

[87] R. Loudon. The propagation of electromagnetic energy through an absorbing dielectric. *J. Phys. A*, 3:233, 1970.

[88] T. M. Grzegorczyk, C. D. Moss, J. Lu, X. Chen, J. Pacheco, and J. A. Kong. Properties of left-handed metamaterials: transmission, backward phase, negative refraction, and focusing. *IEEE Trans. Microw. Theory Tech.*, 53:1443, 2005.

[89] T. M. Grzegorczyk, X. Chen, J. Pacheco, J. Chen, B.-I. Wu, and J. A. Kong. Reflection coefficients and goos-hanchen shifts in anisotropic and bianisotropic left-handed metamaterials. *Prog. Electromagn. Res.*, PIER 51:83, 2005.

[90] J. J. Chen, T. M. Grzegorczyk, B. I. Wu, and J. A. Kong. Role of evanescent waves in the positive and negative goos-hanchen shifts with left-handed material slabs. *J. Appl. Phys*, 98:094905, 2005.

[91] A. D. Boardman and K. Marinov. Electromagnetic energy in a dispersive metamaterial. *Phys. Rev. B*, 73:165110, 2006.

[92] W. C. Chew. Some reflections on double negative materials. *Prog. Electromagn. Res.*, PIER 51:1, 2005.

[93] T. M. Grzegorczyk and J. A. Kong. Analytical expression of the force due to multiple TM plane wave incidences on an infinite lossless dielectric circular cylinder of arbitrary size. *J. Opt. Soc. Am. B.*, 24:644, 2007.

[94] J. M. Fournier, G. Boer, G. Delacétaz, P. Jacquot, J. Rohner, and R. P. Salathé. Building optical matter with binding and trapping forces. *Proc. of the SPIE*, 5514:309, 2004.

[95] T. M. Grzegorczyk and J. A. Kong. Analytical prediction of stable optical trapping in optical vortices created by three TE and TM plane wave incidences. *Opt. Express*, Submitted to Publication, 2007.

[96] L. C. Shen and J. A. Kong. *Applied Electromagnetism, Third Edition.* PWS Publishing, Boston, 1987.

[97] A. Rohrbach. Stiffness of optical traps: quantitative agreement between experiment and electromagnetic theory. *Phys. Rev. Lett.*, 95:168102, 2005.

[98] G. Knoner, S. Parkin, T. A. Nieminen, N. R. Heckenberg, and H. Rubinsztein-Dunlop. Measurement of the index of refraction of single microparticles. *Phys. Rev. Lett.*, 97:157402, 2006.

[99] Timo A. Nieminen. Private communication. The University of Queensland, Austrailia, 2006.

[100] J. Murakowski Z. Lu, C. A. Schuetz, S. Shi, G. J. Schneider, J. P. Samluk, and D. W. Prather. Perfect lens makes a perfect trap. *Opt. Express*, 14:2228, 2006.

[101] H. Chen, L. Ran, J. Huangfu, X. M. Zhang, K. Cheng, T. M. Grzegorczyk, and J. A. Kong. Magnetic properties of s-shaped split-ring resonators. *Prog. Electromagn. Res.*, PIER 51:231, 2005.

[102] L. Ran, J. Huangfu, H. Chen, X. M. Zhang, K. Cheng, T. M. Grzegorczyk, and J. A. Kong. Experimental study on several left-handed matamaterials. *Prog. Electromagn. Res.*, PIER 51:249, 2005.

[103] S. A. Tatarkova, A. E. Carruthers, and Dholakia. One-dimensional optically bound arrays of microscopic particles. *Phys. Rev. Lett.*, 89:283901, 2002.

[104] Yu lin Xu. Electromagnetic scattering by an aggregate of spheres. *Appl. Opt.*, 34:4573, 1995.

[105] J. Ng, Z. F. Lin, C. T. Chan, and P. Sheng. Photonic clusters formed by dielectric microspheres: Numerical simulations. *Phys. Rev. B*, 72:085130, 2005.

[106] L. L. Foldy. The multiple scattering of waves. i. general theory of isotropic scattering by randomly distributed scatterers. *Phys. Rev.*, 67:107, 1945.

[107] M. P. MacDonald, G. C. Spalding, and K. Dholakia. Microfluidic sorting in an optical lattice. *Nature*, 426:421, 2003.

[108] M. Pelton, K. Ladavac, and D. Grier. Transport and fractionation in periodic potential-energy landscapes. *Phys. Rev. E*, 70:031108, 2004.

[109] B. A. Kemp, T. M. Grzegorczyk, and J. A. Kong. Comparison of methods for the calculation of radiation pressure on dielectric and magnetic particles. PIERS Cambridge, 2006.

[110] T. M. Grzegorczyk, B. A. Kemp, and J. A. Kong. Theory and modeling of optical forces within a collection of mie scatterers. PIERS Cambridge, 2006.

[111] X. Chen, J. A. Kong, and T. M. Grzegorczyk. Optimization approach to the retrieval of the constitutive parameters of a slab of general bianisotropic medium. *Prog. Electromagn. Res.*, 60:1, 2006.

[112] L. Tsang, J. A. Kong, and K. H. Ding. *Scattering of Electromagnetic Waves: Theory and Applications.* John Wiley and Sons, New York, 2000.

[113] J. Pacheco. *Theory and Applications of Left-Handed Metamaterials.* PhD thesis, Massachusetts Institute of Technology, 2004.

[114] M. Lax. *Phys. Rev.*, 85:261, 1952.

[115] L. Tsang, J. A. Kong, K. H. Ding, and C. Ao. *Scattering of Electromagnetic Waves: Numerical Simulations.* John Wiley and Sons, New York, 2000.

Biographical Note

Brandon Alden Kemp was born in Jonesboro, Arkansas on August 5, 1975. He is the son of Donnie H. Kemp and Freda J. Kemp and is the younger brother of Bellamy.

He earned the Bachelor of Science in Engineering degree from the Arkansas State University (ASU) in 1997 under the support of the Goldwater Scholarship. While at ASU, he was an undergraduate research assistant in the Optoelectronic Materials Research Laboratory directed by Professor Robert D. Engelken. Brandon's research while at ASU was supported in part by two Science Information Liaison Office (SILO) Undergraduate Research Fellowships, and the results of his efforts were presented at various regional conferences. In 1997, he was awarded the Dwight Moore Research Award for Outstanding Student Technical Paper by the Arkansas Academy of Science. Brandon earned a Master of Science degree in Electrical Engineering in 1998 from the University of Missouri-Rolla (UMR). His thesis was completed in the UMR Electromagnetic Compatibility Laboratory under the advice of Professor Tom Van Doren. He was supported financially by University of Missouri-Rolla Chancellor's Fellowship.

He spent five years as a hardware development engineer with Lexmark International, Inc. in Lexington, KY, USA. While at Lexmark, he specialized in electromagnetic compatibility and high-speed digital design.

From February 2004 to May 2007, Brandon has been a doctoral student at the Massachusetts Institute of Technology. He has served as a research assistant and a teaching assistant to Professor Kong, who is the director of the Center for Electromagnetic Theory and Applications. Brandon's technical interests are in the application of mathematical modeling to a variety of technical areas including electromagnetic wave theory, optical trapping and binding, radar cross section, source localization, and electromagnetic compatibility. He is a member of the IEEE and a registered professional engineer in the state of Kentucky.

Brandon married Shan N. Day on May 22, 1999. They have one daughter named Hadley Faith Kemp.